UNIVERSIDAD DE CHILE
FACULTAD DE CIENCIAS FÍSICAS Y MATEMÁTICAS
DEPARTAMENTO DE ASTRONOMÍA

LAS MATERNIDADES DE OBJETOS ESTELARES JÓVENES ASOCIADOS CON CHORROS

TESIS PARA OPTAR AL GRADO DE MAGISTER EN CIENCIAS MENCIÓN ASTRONOMÍA

MATÍAS ANDRÉS LACKINGTON WERNER

PROFESOR GUIA:
GUIDO GARAY BRIGNARDELLO

MIEMBROS DE LA COMISION:
DIEGO MARDONES PEREZ
LEONARDO BRONFMAN AGUILO
LARS-ÅKE NYMAN

SANTIAGO DE CHILE
MAYO 2011

Resumen

Los procesos de formación y evolución temprana de estrellas de alta masa aun no se entienden bien. El estudio de las estrellas masivas es, tanto desde el punto de vista observacional como teórico, mucho mas complejo que el de las estrellas de baja masa. Aun así se sabe que la zonas de formación de estrellas masivas se encuentran dentro de nubes moleculares gigantes, y que las estrellas masivas nacen en los núcleos más densos de las nubes. Estos núcleos densos y masivos tienen propiedades características (Garay & Lizano 1999) y son denominados las maternidades estelares. En la formación de estrellas de baja masa se observan chorros y flujos bipolares, pero los chorros colimados son raros en regiones de formación estelar masiva (Guzman et al 2010). Para investigar este problema Guzman compiló una lista de candidatos a objetos estelares jóvenes y masivos con posible presencia de chorros.

El objetivo de este trabajo es estudiar los entornos de estos objetos estelares jóvenes con posible presencia de chorros y ver si tienen características similares con las maternidades estelares. Para ello se obtuvieron datos de los siguientes estudios: ATLASGAL (observación en longitud de onda sub-milimétrica), IRAS, MSX y GLIMPSE (observaciones en longitudes de onda infrarrojas). Consideré 2 listas de objetos: (1) la lista de Guzmán que consiste de 45 objetos infrarrojos (con colores infrarrojos de regiones de formación de estrellas masivas y observaciones de líneas moleculares de alta de densidad) y asociados con emisión en ondas de radio, y (2) una lista de 12 regiones HII hiper-compactas que se cree están en la misma etapa de evolución que objetos con chorros. Primero determine cuales de los objetos en ambas listas están dentro del rango de coordenadas en que observó ATLASGAL. Para aquellos objetos que lo estaban obtuve mapas de contorno, flujo total integrado y ajustes Gaussianos a la emisión. Todos los objetos, excepto uno, tienen emisión sub-milimétrica asociada a la posición de la fuente de radio. Estudié la morfología de esta emisión y encontré que la mas común es la de un núcleo central y compacto, rodeado de una envoltura simétrica y débil. Estudié la correspondencia entre la posición de la fuente de radio y el máximo de la emisión sub-milimétrica, encontrando que hay una muy buena correlación y que generalmente la fuente de radio se ubicaba en el centro del núcleo.

Para aquellos objetos incluidos en ATLASGAL (43) obtuve mapas y datos espectrales de los estudios infrarrojos IRAS, MSX y GLIMPSE. Con los mapas construí 2 imágenes de 3 colores (RGB), una para los datos de MSX y la otra para GLIMPSE, para cada objeto. A los datos espectrales obtenidos les ajusté modelos de cuerpos grises de los cuales obtuve valores para la temperatura, densidad de columna y luminosidad de los núcleos. Usando esta temperatura más el flujo sub-milimétrico obtuve la masa y densidad de estos objetos. Encontré que los objetos tienen típicamente tamaños de 0.48 pc, temperaturas de 35°K, masas de 2000 $M_{\odot}$, columnas de densidad de 8.7 x 10^{22} cm^{-2}, densidades moleculares de 1.8 x 10^{5} cm^{-3}, y luminosidades de 1.4 x 10^{5} $L_{\odot}$.

Finalmente, analicé la distribución de los parámetros físicos de los objetos en mi muestra y los comparé con la de objetos estudiados previamente, principalmente con la muestra de Faundez et al. (2004). Comprobé que los objetos analizados tienen las características de los núcleos densos y masivos.

Agradecimientos

Quisiera agradecer a mi familia, en especial a mis padres, ya que con su apoyo incondicional y cariño las etapas difíciles se superaron y los momentos felices se disfrutaron más.

Agradezco a mi profesor guía Dr. Guido Garay por las enseñanzas y la ayuda durante estos años, pero sobre todo por el entendimiento que tuvo conmigo. Agradezco a los miembros de la comisión de tesis Dr. Leonardo Bronfman, Dr. Diego Mardones y Dr. Lars Nyman. Y también a Andrés Guzman por toda la ayuda para mi trabajo.

Agradezco a los docentes y funcionarios de Cerro Calán por la gran formación que me han dado durante pregrado y magíster, en especial al Dr. René Mendez por sus consejos.

Agradezco a mis compañeros de astronomía e ingeniería, por su apoyo, ayuda, y sobre todo la amistad y alegría que hemos compartido durante estos años de estudio.

Contents

Index of Tables

Index of Figures

Chapter 1

Introduction

Massive stars play a dominant role in the shaping and evolution of galaxies, through radiative (UV radiation), kinetic (winds, massive outflows, expanding HII regions and supernova explosions) and chemical (main source of heavy elements) feedback into the interstellar medium. However, the formation process and early evolution of high-mass stars is not well understood. The main reasons are: (1) in the critical early phases of star formation the abundance of dust makes them difficult to observe; (2) high mass stars evolve quickly so the early stages are short lived. Hence high mass stars are rare, implying that they are generally observed at large distances; and (3) high mass stars are rarely (if at all) formed in solitary, but in clusters. The presence of other massive stars give rise to a complex environment via gravitational interaction, winds, outflows and ionizing radiation. Thus the study of high-mass star from both observational and theoretical point of view is much more complex than that of low mass star formation.

In spite of the previous arguments, important progress, both observational and theoretical, has been made during the last two decades concerning the process of high-mass star formation. We know that massive star forming regions are found within giant molecular clouds and that massive stars are formed mainly within the dense cores of giant molecular clouds. This is supported by a wealth of observations that show that the signposts of recently formed massive stars, such as the compact HII regions, are associated with warm and dense regions of molecular gas (Churchwell et al. 1990; Cesaroni et al. 1991); Plume et al. 1992). These dense cores have distinctive characteristics (Garay & Lizano 1999):

- Mean linear sizes of 0.3 – 1.0 pc
- Mean molecular densities in the range of $2 \times 10^4 - 3 \times 10^6$ cm^{-3}
- Mean kinetic temperatures of 30 − 50 °K
- Mean masses between $10^3 - 3 \times 10^4$ $M_\odot$

From a theoretical point of view, the formation of high mass stars is likely to proceed as follows (Zinnecker & Yorke 2007).

1. The first stage is characterized by the formation of a cold dense massive core (CDMC) or filament, induced by gravitational turbulent cloud fragmentation (M. Low & Klessen 2004). Supersonic turbulence rapidly produces localized compressed pockets of gas, some of which remain gravitationally bound and provide the initial conditions for collapse (Padoan & Nordlund 2002). These CDMC are starless clouds, in the verge of collapsing, or already collapsing.

2. The second phase is characterized by non-homologous gravitational collapse of portions of the cores into optically thick, pressure-supported protostellar embryos with initial masses of the order of 10^{-3} $M_\odot$ (Larson 1969; Bate 2000). The term non-homologous collapse refers to the fact that the relative distribution of mass changes, as opposed to a homologous or self-similar collapse. When a protostar forms in the center it heats the core turning it into a hot dense massive core (HDMC). At this stage outflows and jets begin to appear, and are seen in water and methanol masers.

3. The third stage of the high-mass protostar formation as it evolves towards the main sequence is the accretion stage, characterized by a central protostellar object and a circumstellar disk surrounded by an

envelope of infalling gas and dust.

- This stage is accompanied by molecular outflows and jets which transfer linear and angular momentum, and mechanical energy from the infalling material into the surroundings. Unlike the low-mass stars, high-mass stars start burning hydrogen and develop radiation-driven winds as they continue to accrete and evolve up the main sequence to hotter and more luminous states (Kudritzki 2002).

4. Disk-accreting main-sequence star. Here the jets opening angles are widening becoming less collimated. The accretion disk starts to get photoionized and photoevaporated (and possibly even be disrupted), which makes a gravitationally confined hyper-compact HII region (HCHII). So the presence of a massive disk, and hence the appearance of molecular outflows and jets, in the accretion is thus not clear.

5. Final main-sequence star; at some point star has accreted its final mass, while the disk has been dissipated. At this stage the ionizing radiation is not stopped by the accretion disk and so it can expand to the vicinity of the star, merging with other ionizing bubbles of different stars. This is denominated a ultra-compact HII region (UCHII), and often they are associated with OH masers. The UCHII region expands to become a compact radio HII region and finally a diffuse optical HII region.

- But there is controversy about how they attain their final masses as the radiation pressure of high mass stars can be enough to stop the infall of material. The main theories to circumvent this problem are: competitive accretion (Bonnell et al. 2004) or coalescence of intermediate mass stars (Bonnell et al. 1998).

6. Disruption phase, which in some effects take place during the previous stages. High-mass stars strongly influence their environment by their winds, molecular outflows, and UV radiation, and eventually supernovae, which will drastically affect the physical conditions, structure, and chemistry of their surroundings.

Whereas there is ample evidence for the presence of molecular outflows in high mass star forming regions (Shepherd & Churchwell 1996; Beuther et al. 2002; Wu et al. 2004; Zhang et al. 2001), collimated jets are rare (Guzmán et al. 2010). Whether this is due to a different formation mechanism for high and low mass stars or very short time scales for the jet phenomenon in high-mass stars is not known. To investigate this issue Andres Guzman (private communication) has compiled a list of high-mass YSO (young stellar object) candidates, based on an RMS color criteria and strength of radio emission, and started a survey for radio jets. The characteristics of the environment of the jets candidates are, however, not known. Are they embedded in dense cores, the birthplace of high mass stars? Which is the morphology of the environment: spherical or filamentary? Which is the mass distribution of the sample?

To address these questions, in this thesis I will use the new available ATLASGAL data (Schuller et al 2009) to study the characteristics of the dust continuum emission. ATLASGAL is an unbiased survey of continuum emission at 870 microns (in the sub-millimeter range) of the galactic plane, carried out using the LABOCA (Large Apex Bolometer Camera) instrument at the APEX 12m sub mm antenna. The dust continuum emission in the (sub) millimeter range is a good tracer of dense interstellar material from which stars form and therefore is ideal to study the earliest phases of star formation. In addition to the list of high-mass YSOs from Guzman, I also considered a sample of hyper-compact HII regions which are thought to be in a similar evolutionary phase than jets. Our final list consists of 57 targets (45 of the Guzman and 12 compact HII regions). So one of the objectives will be to see if these are present in the ATLASGAL data, and from there analyze the environment of each object.

In addition, I will make use of publicly available data at several wavelengths to complement our data. With these overall data I will obtain further information about the environments of each object in the sample so as to advance in the understanding of every individual object. I will determine the physical parameters of the dust structures, such as their mass, size and temperature, and assess whether the targets

correspond to high mass star forming regions, i.e. dense cores. I will then investigate the mass, size and temperature distribution of the sample as a whole, and compare to that of dense cores from previous works. I will look for parameters correlations like mass vs luminosity relations. And finally I will characterize the environments structure, like determining if the 870 emission is a single core, or if it is inside a more diffuse and extended envelope.

Chapter 2

The Samples

2.1 Guzman Sample

Andres Guzman (private communication) has compiled a list of high-mass YSO candidates, based on an Red MSX Sources (RMS) color criteria and strength of radio emission, and started a survey of radio jets. This list is shown in Table 1, along with their coordinates in J2000 and in galactic coordinates. The distribution in the ATLASGAL coverage is seen in Figure 1 represented by the square points.

2.1.1 Construction

Guzman's list of jet candidates was selected from the catalog of RMS associated with compact radio sources (Urquhart et al. 2007), and from the catalog of Ultra Compact HII regions (UCHIIR) of Walsh et al. (1998) as described in what follows.

RMS sources are objects detected by the Midcourse Space Experiment (MSX) having characteristic colors on the MSX and 2MASS (Two Micron All-Sky Survey) bands, thought to correspond to YSOs (Lumsden et al. 2002). The criteria for selection as an RMS source can be summarized as:

$$F_{21\mu m} > F_{14\mu m} > F_{8\mu m} \quad \text{, (rising, featureless red continuum)} \tag{1}$$

$$F_{21\mu m} > 2\mathrm{F}_{8\mu m} \quad . \tag{2}$$

Sources fulfilling this criteria have a 2/3 probability of being a massive young stellar objects (MYSO). The criteria is combined with the 2MASS color criterion:

$$F_{8\mu m} > 2\mathrm{F}_{K} \quad and \quad F_{K} > 2\mathrm{F}_{J} \quad . \tag{3}$$

Conditions (1, 2 and 3) are fulfilled by ~2000 MSX sources with |b|<5° and |l| >10°. Of these, ~800 were selected by Urquhart et al. (2007) according to:

1. Observability with the Australian Telescope Compact Array (ATCA)
2. Not observed in another high-resolution radio emission survey (e.g. Walsh et al. 1998)
3. Not already identified in the literature

The Walsh et al. (1998) sample was built from IRAS sources using an infrared color criteria proposed by Wood & Churchwell (1989) to target UCHII regions;

$$\log(F_{25\mu m}/F_{12\mu m}) > 0.57 \ , \quad \log(F_{60\mu m}/F_{12\mu m}) > 1.3 \quad . \tag{4}$$

There are ~1900 IRAS sources in the galaxy that fulfill the above condition (4). From these Walsh et al. (1997) selected ~500 sources according to their association with 4.85 GHz radio-continuum sources, OH, H_2O or methanol masers. Finally, Walsh et al. (1998) found 364 IRAS sources with methanol 6.67 GHz maser and/or compact radio continuum emission.

To search for jet candidates within the Urquhart and Walsh samples, Guzman further selected those radio sources with positive radio continuum spectral index at centimeter wavelengths. He found 119 and 45 sources fulfilling this criteria for the Urquhart and Walsh catalogs respectively (included are non-detections at the lower frequency). We note that in both surveys the high frequency data is at 8.6 GHz. In the work by Urquhart the low frequency data is at 4.8 GHz which was observed with the same sensitivity as the 8.6 GHz, thus a non-detection implies a positive spectral index. For the Walsh et al. (1998) sample the lower band comes from continuum observation near the 6.67 GHz maser line, observed at a high resolution filter hence with lower sensitivity than the 8.6 GHz data so a non detection does not imply a positive spectral index.

MYSO are expected to be surrounded by an envelope of gas and dust which will absorb all the radiation. Thus most of the luminosity will be re-emitted in the infrared and so they should be seen as IRAS sources. Imposing a maximum offset of 1' between the radio and IRAS position, the list is narrowed to 76 and 18 objects from the Urquhart and Walsh-98 respectively.

Finally, to distinguish between a normal optically thin HII region and a jet source, Guzman looked at the quotient between the F_{IR} and the 8.6 GHz free-free flux. For a given infrared luminosity, jets are expected to have less radio luminosity than optically thin HII regions. Of the sources with line measurements (86) from other references (e.g. CS(2-1) observations from Bronfman et al. (1996)), necessary for determining the distance to the source, 66 fulfill the previous criteria. Finally only objects with luminosities greater than 20000 $L_\odot$ will be considered, narrowing the final list to 45 objects.

Table 1: Guzman Sample

Object	RA (J2000)	DEC (J2000)	l	b
07427-2400	07 44 52.04	-24 07 42.4	240 18 57.4	+00 04 17.0
G274.0649-01.1460	09 24 42.13	-52 02 00.8	274 03 52.3	-01 08 50.2
G286.3938-01.3514	10 33 56.48	-59 44 00.4	286 23 38.7	-01 21 06.0
G289.9446-00.8909	11 01 09.00	-60 56 56.3	289 56 29.5	-00 53 23.2
G293.9633-00.9776	11 32 36.14	-62 28 08.3	293 57 45.4	-00 58 41.0
G298.2234-00.3393	12 10 01.16	-62 49 53.9	298 13 27.2	-00 20 20.7
G300.9674+01.1499	12 34 53.23	-61 39 40.1	300 58 07.5	+01 08 51.0
G301.1364-00.2249A	12 35 35.13	-63 02 31.7	301 08 11.1	-00 13 32.4
G301.1364-00.2249B	12 35 35.19	-63 02 24.0	301 08 11.1	-00 13 24.7
G302.1515-00.9488	12 44 22.38	-63 48 35.0	302 09 08.6	-00 56 55.2
13134-6242	13 16 42.62	-62 58 21.2	305 47 54.2	-00 14 29.6
G308.9176+00.1231	13 43 01.72	-62 08 56.1	308 55 03.1	+00 07 18.4
13471-6120	13 50 41.89	-61 35 11.5	309 55 14.3	+00 28 42.6

Object	RA (J2000)	DEC (J2000)	l	b
G311.1359-00.2372	14 02 09.93	-61 58 37.9	311 08 10.0	-00 14 14.3
G317.4298-00.5612	14 51 37.60	-60 00 19.4	317 25 43.8	-00 33 38.3
G317.8908-00.0578	14 53 06.19	-59 20 56.7	317 53 22.3	-00 03 26.8
G326.7249+00.6159	15 44 59.36	-54 02 18.9	326 43 26.3	+00 36 53.6
15437-5343	15 47 32.47	-53 51 30.9	327 07 50.6	+00 31 33.4
G326.5297-00.4186	15 48 19.42	-54 58 20.8	326 31 47.6	-00 25 07.9
G329.4761+00.8414	15 58 16.52	-52 07 37.6	329 28 38.0	+00 50 33.5
G330.2935-00.3946	16 07 38.08	-52 30 53.7	330 17 43.8	-00 23 33.7
G333.0162+00.7615	16 15 18.7	-49 48 52.8	333 01 00.7	+00 45 42.4
G332.8256-00.5498	16 20 11.07	-50 53 15.3	332 49 33.4	-00 32 57.3
G333.1306-00.4275	16 21 02.95	-50 35 12.3	333 08 05.7	-00 25 55.1
G336.9842-00.1835	16 36 12.42	-47 37 58.0	336 58 59.8	-00 10 59.4
G337.7091+00.0932	16 37 54.43	-46 54 36.5	337 42 45.2	+00 05 16.9
G337.7051-00.0575	16 38 29.63	-47 00 35.3	337 42 19.2	-00 03 11.0
G337.4032-00.4037	16 38 50.45	-47 28 02.7	337 24 13.7	-00 24 08.2
G338.9217+00.6233	16 40 15.46	-45 39 02.5	338 55 20.3	+00 37 27.8
G337.8442-00.3748	16 40 26.67	-47 07 13.1	337 50 38.0	-00 22 28.3
G340.2480-00.3725	16 49 30.00	-45 17 44.2	340 14 55.4	-00 22 17.5
G345.0061+01.7944	16 56 47.59	-40 14 25.8	345 00 34.2	+01 47 32.6
16547-4247	16 58 17.21	-42 52 07.1	343 07 36.6	-00 03 46.1
16561-4006	16 59 37.75	-40 12 03.5	345 22 36.4	+01 23 33.3
G345.4938+01.4677	16 59 41.61	-40 03 43.4	345 29 37.2	+01 28 07.4
17238-3516a	17 27 11.32	-35 19 32.8	352 31 01.9	-00 09 18.0
17238-3516b	17 27 11.32	-35 19 32.8	352 31 01.9	-00 09 18.0
17439-2845a	17 47 09.66	-28 46 27.7	0 18 48.9	-00 12 15.1
17439-2845b	17 47 09.66	-28 46 27.7	0 18 48.9	-00 12 15.1
17559-2420	17 59 05.98	-24 21 16.4	5 28 34.3	-00 15 25.3
18048-2019	18 07 52.84	-20 18 29.3	9 59 51.8	-00 01 59.4
18064-2020	18 09 22.27	-20 19 14.4	10 09 22.5	-00 20 41.5
18162-2048	18 19 12.1	-20 47 30.7	10 50 29.1	-02 35 29.9
18314-0720	18 34 08.12	-07 18 18.2	24 27 44.7	+00 29 34.6
18316-0602	18 34 20.91	-05 59 39.3	25 39 01.3	+01 02 59.3

2.2 Hyper Compact HII Regions

In addition to the Guzman sample, I compiled from the literature a list of Hyper Compact HII thought to be in a similar evolutionary phase than jets. Their names and positions are listed in Table 2. HCHII regions are very small ionized regions around massive stars, with typical sizes ≤ 0.05 pc and densities ≥ 10^6 cm^{-3} (Hoare et al. 2007). Another typical characteristic is a rising continuum spectra, $S_\nu \sim \nu^\gamma$, with a slope of γ ~ 1 which is intermediate between the optically thick and thin cases. This may due to the presence of jets, a distribution in size of constant density clumps, or density gradients. The distribution in the ATLASGAL coverage is seen in Figure 1 represented by the circular points.

Table 2: HCHII region sample

Object	RA (J2000)	DEC (J2000)	l	b
G9.62+0.19F	18 06 14.80	-20 31 39.2	9 37 10.6	+00 11 39.5
G10.47+0.03	18 08 38.22	-19 51 46.7	10 28 23.2	+00 01 39.7
M17-UC1	18 20 24.84	-16 11 35.1	15 02 04.4	-00 40 38.1
G20.08-0.14N	18 28 10.3	-11 28 48	20 04 51.0	-00 08 07.2
G24.78+0.08A1	18 36 12.5	-07 12 10	24 47 23.5	+00 05 01.0
G28.20-0.04N	18 42 57.88	-04 13 55.9	28 12 01.1	-00 02 54.1
G34.26+0.15B	18 53 18.80	+01 14 55.7	34 15 25.6	+00 09 08.0
G12.89	18 59 09.87	+04 12 13.6	37 33 11.4	+00 12 03.4
G43.80-0.13	19 11 53.77	+09 35 50.3	43 47 41.9	-00 07 35.2
G45.07+0.13	19 13 21.86	+10 50 55.5	45 04 16.8	+00 07 59.8
G75.78+0.34	20 21 44.10	+37 26 39.7	75 46 57.7	+00 20 34.2
NGC-7538 IRS1	23 13 45.02	+61 28 12.7	111 32 30.2	+00 46 39.9

Chapter 3

The Data

3.1 Description

To investigate the characteristics of the environments around the targets I make use of the ATLASGAL (Schuller et al. 2009) sub-millimeter survey data which has been obtained by Universidad de Chile researchers in collaboration with the Max Planck Institute für Radioastronomie in Bonn, Max Planck Institute für Astronomie in Heidelberg, and the European Southern Observatory (ESO).To complement these data I use data from the publicly available infrared surveys: IRAS (far-infrared), MSX (mid-infrared) and GLIMPSE (near-mid infrared). From the ATLASGAL, GLIMPSE and MSX surveys I obtained images. And from the MSX and IRAS point source catalogs I obtained photometric information. Additionally I searched for radial velocity and distance data in the following references: Bronfman et al. (1996) CS(2->1) survey, Avedisova (2002b) catalog from Vizier, and Pestalozzi et al. (2005) 6.7 GHz methanol masers catalog.

3.1.1 ATLASGAL

The APEX Telescope Large Area Survey of the Galaxy (ATLASGAL) is an unbiased survey of the inner galactic plane at 870 μm (Schuller et al. 2009). The observations were carried out using the LABOCA (Large Apex Bolometer Camera) instrument at the APEX 12m submm antenna. This antenna has a surface accuracy of 15 μm rms. LABOCA is a 295 element bolometer array arranged in an hexagonal pattern, with two-beam spacing between bolometers (Siringo et al. 2009). Its bandpass is centered at 870 μm and has a bandwidth of 60 GHz. Located at the Cassegrain focus it has a field of view of 11.4' in diameter. The beam size at this wavelength is 19.2" FWHM. The final area coverage is l = 300° to 60°, |b| <1.5°. The typical 1-σ noise level is in the range 50-70 mJy/beam, and the final flux uncertainty should be lower than 15%. The data release map sizes are 3°x3° with a resolution of 6 arcsec per pixel.

3.1.2 GLIMPSE

The Galactic Legacy Infrared Midplane Survey Extraordinaire (GLIMPSE) Legacy Program (Benjamin et al. 2003) is a survey of the galactic plane in the four bands of the Infrared Camera Array (IRAC; Fazio et al. (2004)) instrument aboard the Spitzer Space Telescope (Werner et al. 2004). The images downloaded from the publicly available data are at 3.6, 4.5, 5.8, 8.0 μm, with a resolution of 1.25" per pixel, and an image size of 2.4° x 3.1°.

3.2 Data Reduction

First I downloaded all the ATLASGAL maps available from the full survey. Since this is a large

database, I automatized the process of searching whether or not the targets are within the coverage area, and identified the corresponding maps. For this I used the WCSTOOLS software, which is a package of programs and a library of subroutines for setting and using the WCS (world coordinate system) in the headers of FITS files to relate pixels to sky coordinates (Mink 2010). In this part I used specifically the 'cat' function which given a set of coordinates searches in the FITS images for these objects, and returns all which are present in pixel coordinates. Not all the sources from our list fall into the current ATLASGAL coverage, narrowing our list of targets. From this new list I proceeded to download the complementary data of the other surveys. The coverage used and how the sources of our list fall into is shown in (Figure 1).

The maps from all the surveys have already been calibrated, and ready to use. However they had different projection, coordinates and epoch, so I standardized them to TAN projection and equatorial J2000 coordinates.

GLIMPSE maps were in TAN projection with J2000 WCS. MSX maps were in CAR projection and Galactic WCS. All ATLASGAL final maps were in Galactic WCS and in TAN projection. Again I rely on wcstools to automatize the process. I used the 'remap' function to change the map projections. For the MSX maps I had to first redefine the reference pix values and positions in the header so they correspond to the center of the map, so as to 'remap' work correctly, and for this I used the 'gethead' and 'sethead' functions. With the maps in TAN projection I used again the 'cat' routine to obtain the correct locations of the objects in the images, this time also in the GLIMPSE and MSX data.

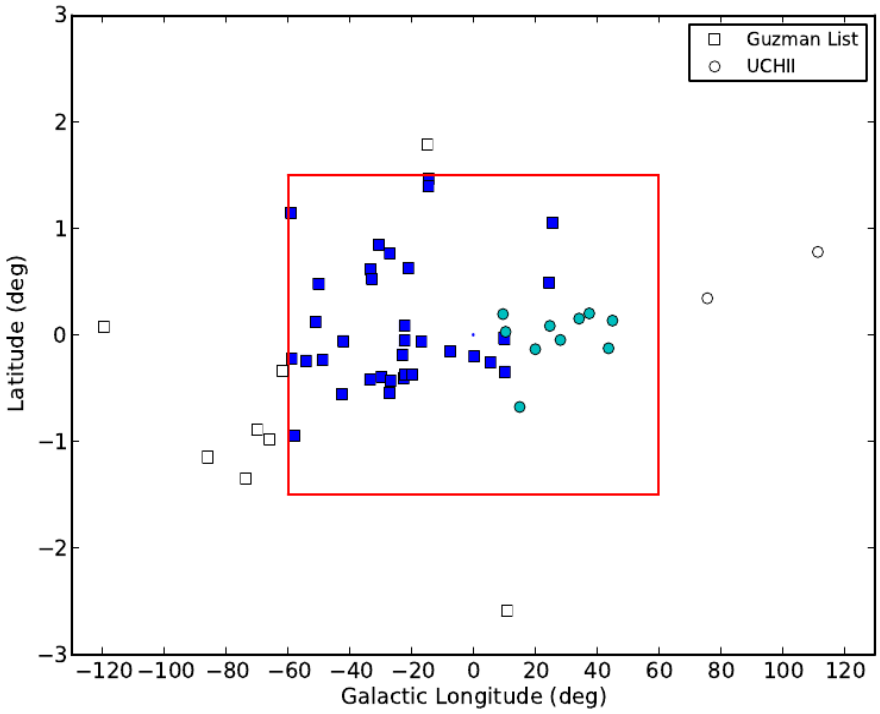

Figure 1: Samples Distribution in ATLASGAL coverage

3.3 Data extraction

3.3.1 ATLASGAL

The first goal was to assess whether or not our objects are associated with 0.87 mm emission. Guzman's initial list of 45 radio sources, was shortened to 42 targets as in the ATCA resolution there were some double objects but the ATLASGAL resolution couldn't resolve them (e.g. 17238-3516a and 17238-3516b were counted only as 17238-3516). Of the 42 remaining 34 were in the ATLASGAL coverage area, and all, except one, had a 0.87 mm counterpart.

Of the 12 sources of the UCH2 list, 10 were in ATLASGAL and they all had a counterpart at 870 μm. So I ended with a total of 43 (33 and 10) sources to analyze.

For the final list of 43 objects with 0.87 mm emission, I extracted the size and flux data from the maps. To do this I used the AIPS (Astronomical Image Processing System; Greisen 2009) program of the NRAO (National Radio Astronomy Observatory), which is a software package for calibration, data analysis, image display, plotting, and a variety of ancillary tasks on Astronomical Data.

First I loaded the maps into AIPS, and using the previously obtained pixel coordinates of the objects I made a sub-image for each source, with 7.07'x7.07' of size centered at the location of the radio source. Then I proceeded to change the pixel system coordinate to equatorial J2000, which produced a misalignment between the x-y axes of the image and the right ascension and declination of the sky coordinates. So I rotated the obtained image respect to the center (if necessary) to match them. After the rotation there are blank spaces in the area of the map, so I perform a second cut to reduce the size to 5' x 5' where there are no null data.

Then I proceeded to extract the required data for analysis. I used two routines to extract the flux density of the sources, *jmfit* and *imean*. *imean* returns the total flux density and the maximum value within a box given by the user, and *jmfit* fits an elliptical Gaussian to the source returning the total flux density, peak flux, peak location, and minor and major axes (FWHM) of the ellipse (observed and deconvolved). It has to be noted that the *jmfit* flux assumes a Gaussian distribution of the intensity distribution. Since the intensity distribution may not be Gaussian, I used the *imean* value as the actual flux of the source.

So I finally obtained: total flux [Jy], peak value of the Gaussian [Jy/beam] and deconvolved size [arcsec x arcsec], all at 870 μm. The values are listed in Table (3).

Table 3: Extracted Parameters from ATLASGAL

Object	Jmfit Peak [Jy/beam]	Jmfit iflux [Jy]	Imean iflux [Jy]	Major Axis ["]	Minor Axis ["]
G300.9674+01.1499	6.1	30.63	27.72	39.84	33.36
G301.1364-00.2249	20.09	48.68	52.85	24.39	19.13
G302.1515-00.9488	0.87	2.7	2.62	29.24	23.8
G308.9176+00.1231	2.51	13.11	11.68	42.91	32.46
G311.1359-00.2372	0.45	3.12	2.84	49.03	39.79
G317.4298-00.5612	2.08	6.47	6.33	27.05	25.86
G317.8908-00.0578	1.24	5.77	5.02	41.59	28.64
G326.5297-00.4186	0.35	0.4	0.43	10.12	10.12
G326.7249+00.6159	7.11	29.29	27.33	36.92	27.79
G329.4761+00.8414	1.4	5.24	4.86	35.95	24.84
G330.2935-00.3946	5.25	16.1	16.47	28.08	24.32
G332.8256-00.5498	25.98	83.94	97.2	28.6	25.84
G333.0162+00.7615	6.69	59.16	48.49	61.94	41.64
G333.1306-00.4275	19.11	142.8	119.72	50.34	42.57
G336.9842-00.1835	1.33	3.48	3.73	26.37	20.04
G337.4032-00.4037	15.69	46	51.96	26.62	24.04
G337.7051-00.0575	12.21	31.37	35.34	23.51	22.14
G337.7091+00.0932	7.53	22.71	24.67	29.44	22.47
G337.8442-00.3748	2.68	8.35	9.42	27.44	25.65
G338.9217+00.6233	4.79	28.65	28.85	51.05	31.79
G340.2480-00.3725	4.39	39.13	32.09	57.74	45.41
G345.4938+01.4677	14.38	124.45	132.82	56.22	45.03
13134-6242	10.64	21.64	23.65	19.86	17.19
13471-6120	6.37	20.98	22.81	31.31	24.07
15437-5343	3.15	10.39	10.04	30.98	24.39
16547-4247	16.6	52.7	58.38	30.35	23.55
17238-3516	2.3	6.67	6.4	27.86	22.52
17439-2845	4.02	27.71	24.68	51.63	37.57
17559-2420	0.95	33.17	17.25	135.41	82.6
18048-2019	0.66	1.82	1.72	27.26	20.95
18064-2020	3.27	29.95	22.16	58.73	45.95
18314-0720	2.13	49.92	39.74	105.83	69.93

Object	Jmfit Peak [Jy/beam]	Jmfit iflux [Jy]	Imean iflux [Jy]	Major Axis ["]	Minor Axis ["]
18316-0602	6.28	29.77	30.1	38.99	31.68
G9.62	10.56	32.68	34.36	29.73	23.16
G10.47	29.96	59.86	65.79	18.3	18.1
M17	19.62	250.06	196.03	67.45	57.71
G20.08-0.14N	6.34	14.96	17.92	21.96	20.54
G24.78+0.08 A2	13.49	46.59	50.48	30.77	26.38
G28.20	8.07	25.27	25.98	29.94	23.44
G34.26+0.15B	45.96	143.81	145.77	27.05	26.13
G12.89	3.26	11.33	11.07	35.52	22.47
G43.80	5.98	13.31	14.41	21.23	19.12
G45.07	6.26	16.57	18.05	23.97	22.77

Although ATLASGAL gives a typical noise level, for each map I took a zone with no sources and calculated its mean and rms using the imean routine. For each map then I computed a three sigma noise level which I will use as a threshold for detection in the map. The average of this value was 220 mJy/beam, with a minimum of 110 mJy/beam, which is close to the typical 3-σ noise (rms) of 150-210 mJy/beam given by Schuller et al. (2009).

3.3.2 GLIMPSE

All of the 43 sources were in the range of the GLIMPSE survey. Two of them, G300.9674+01.1499 and 18316-0602 only had data at two of the four IRAC bands.

GLIMPSE resolution is much better (1.25" versus 19.2") than of ATLASGAL. For this reason for one object in ATLASGAL there can be several objects in the same region in a Spitzer band. As default I will take the flux of the object of GLIMPSE that matches the peak of the 870 μm emission, or the closest one. For each counterpart I will use the same box for the four IRAC bands and calculate the flux inside of it. This box is taken so that all the flux of the counterpart in the I4 band falls into it unless otherwise stated. I used the I4 band because it has a better correlation with the dust emission and the emission was generally more extended.

3.3.3 IRAS and MSX

All 43 objects were in the MSX and IRAS surveys. I took the value of the flux from their point sources catalogs (PSC) available through a web based catalog query at NASA/IPAC infrared science archive website. From the MSX survey I also obtained maps.

A priori I had the IRAS ans MSX names because of the way the initial list was built, but I corroborated that the coordinates indeed match the 870 μm emission. This was more important for the second list. I also had to see if the better resolution of ATLASGAL and Spitzer resolve the IRAS and MSX point sources into many counterparts.

Chapter 4

Results

4.1 Individual Sources

In this section I present contour maps of the 870 μm emission for each of the sources, and give a brief description of the dust morphology and flux. Additionally I present two three-color images, created with the data from Spitzer and MSX. All images and maps have the same angular size, of 5'x5', centered on the radio source position indicated by a cross of 15"x15" of size.

I created 4 types of level contours for each map:

i. 1, 5, 10 to 90 by 10 percent
ii. 2, 5, 10 to 90 by 10 percent
iii. 5, 10 to 90 by 10 percent
iv. 10 to 90 by 10 percent

The maps that I present will have one of these types of contours, depending on the noise level of the image. To calculate the background noise I took a portion of the image without emission and computed its rms value. So our levels are chosen in such a way that the lowest contour is above three times the mean background noise. For four objects (G302.1515, G311.1359, G326.5297, and 17559-2420) the 10% contour was below our criteria, so I created special maps which started at the 3-sigma computed noise level and the levels were of increasing multiples of sigma.

To analyze the infrared data of GLIMPSE and MSX I created false color (RGB) images. The Spitzer RGB images were composed using red for the 8 μm IRAC4 band, green for the 5.8 μm IRAC3, and blue for the 4.5 μm IRAC2 band. Meanwhile for the MSX images I used red for the 21.34 μm E band, green for the 12.13 μm C band, and blue for the 8.28 μm A band. To be able to compare this images to the sub-millimeter data in the RGB images I plotted in yellow four contours; 20, 40, 60 and 80 percent of the peak flux.

With respect to the MSX color images, we note that a red color dominance indicates a high flux at longer wavelength, which is a hint for the presence of a more embedded source. The higher frequencies emissions are absorbed by the dust, and re-emitted at longer wavelengths and is a source is embedded enough the higher frequencies are all absorbed and the object is only seen in this case a red source. So on the other side as the blue color (A band) isophotal wavelength is 8.28 μm, its dominance is due to PAH emissions or hot dust(>300 °K) which has been heated by absorbing all the high frequencies flux. So a red color dominance points to a more embedded object, and a blue one towards a more evolved evolutionary state.

The colors of the Spitzer three color image are such that more evolved zones are blue and more embedded ones are red, the same conclusion as for the MSX colors. In addition, the red color emission in the Spitzer three color image should be about the same, albeit the better resolution, as a blue in the MSX as it is from the the IRAC 1 band which has 8 μm as isophotal wavelength.

4.1.1 Maps

4.1.1.1 G300.9674+01.1499

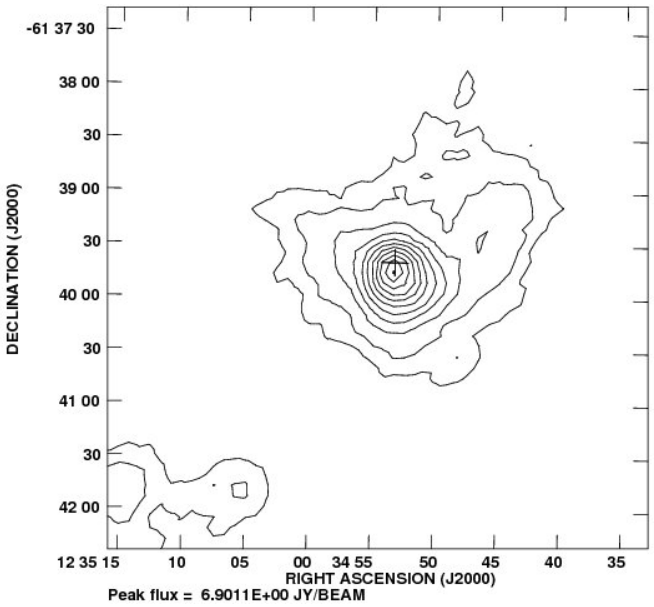

Figure 2a: 870 μm emission, contour levels iii

The 870 μm emission towards G300.9674+01.1499 arises from a single source with a bright core and a weak, extended and irregular envelope. The radio source lies at the peak of the dust emission. The region has a total flux density of 27.72 Jy and peak flux density of 6.9 Jy/beam. The map's rms noise is 110 mJy/beam.

The MSX image shows two bright sources about 30" towards the east and north of the radio source, and a third weak embedded associated with the radio source. This is one of the two sources in the sample without Spitzer three color image (it was observed in only two bands).

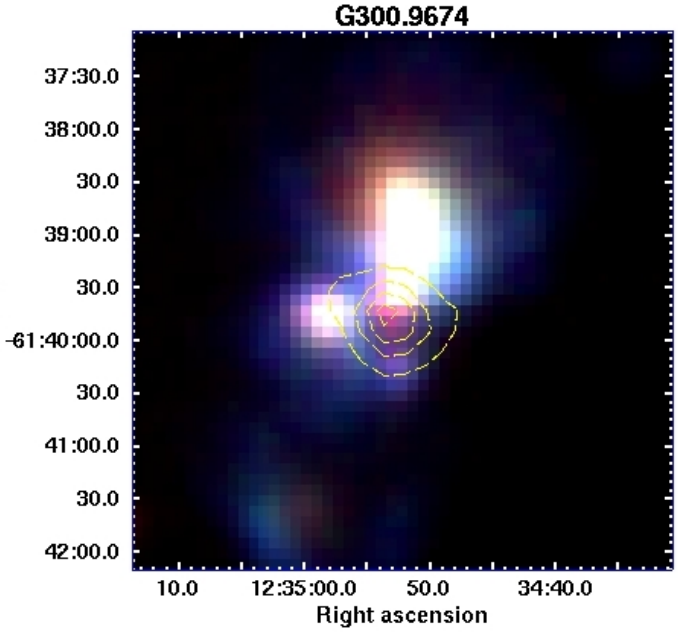

Figure 2b: MSX three color image

4.1.2 G301.1364-00.2249

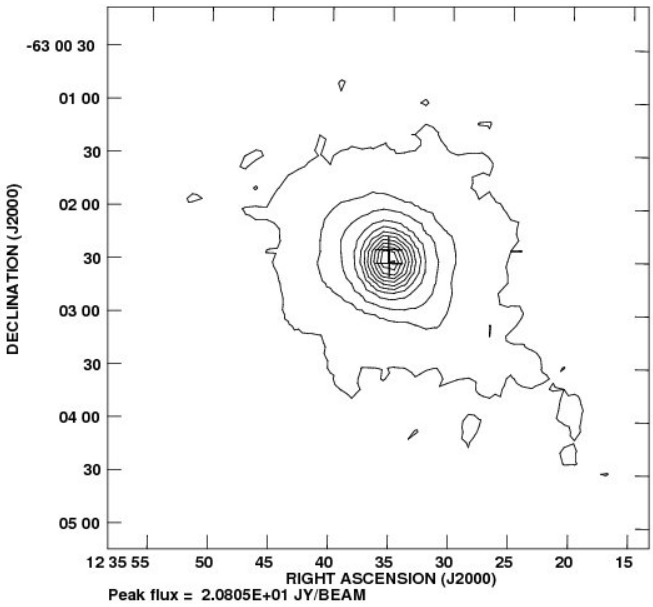

Figure 3a: 870 µm emission, contour levels i

The 870 µm emission towards G301.1364-00.2249 arises from a single source with a centrally condensed morphology, namely the presence of a bright compact core and a weak extended envelope. The total flux density and peak flux density are 52.85 Jy and 2.08 Jy/beam respectively. The map's rms noise is 70 mJy/beam. The two radio sources lie in the center of the dust core.

The MSX image shows a bright embedded source coincident with the compact core. The Spitzer image shows the presence of a cluster of 5 to 6 objects within the compact dust core. In both images, an extended emission at 8 µm is seen surrounding the central core.

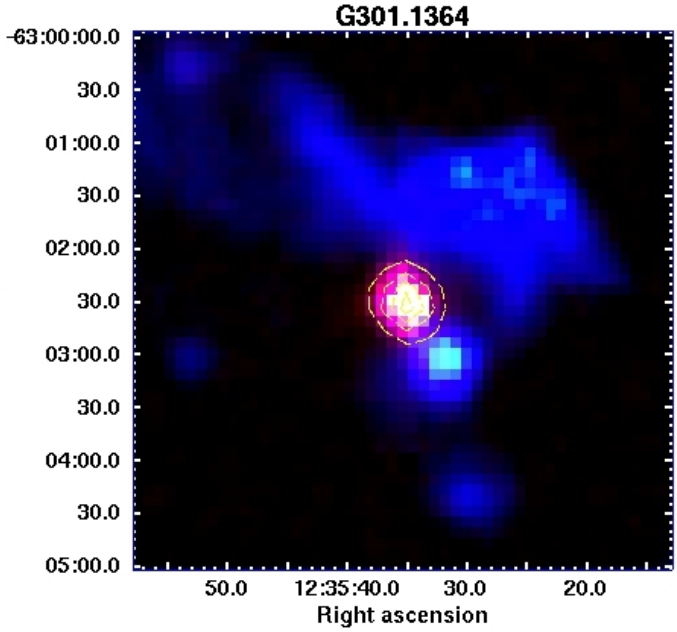

Figure 3b: MSX three color image

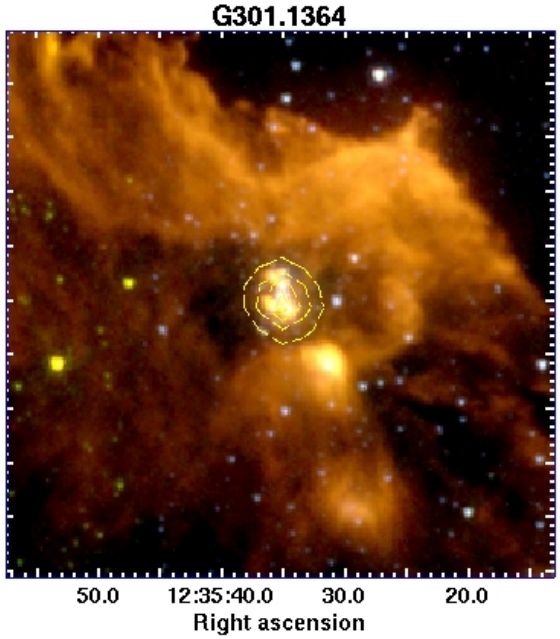

Figure 3c: Spitzer three color image

4.1.3 G302.1515-00.9488

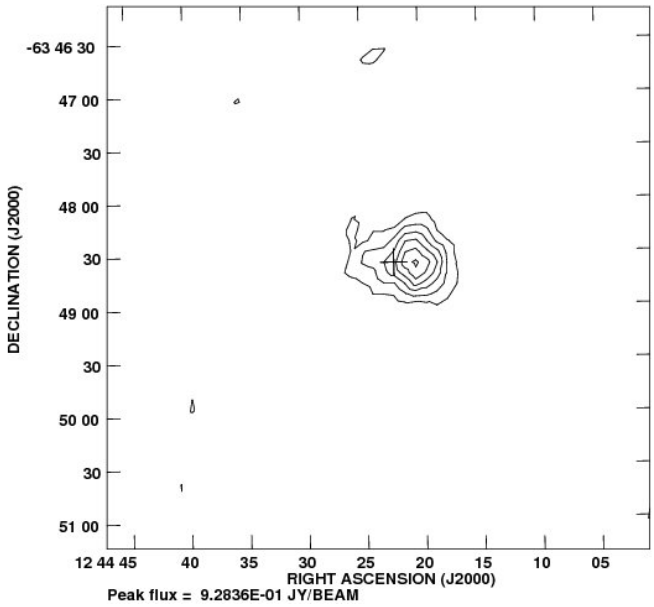

Figure 4a: 870 μm emission, contour levels: Starting from 3-sigma (150 mJy/beam) and increasing in steps of 3-sigma

The 870 μm emission towards G302.1515-00.9488 arises from a single source with a bright component to the west and a weaker component to the east. The total flux density and peak flux density are 2.62 Jy and 0.928 Jy/beam respectively. The map's rms noise is 50 mJy/beam. The radio source lies within the emission but not in its peak position.

The MSX image shows a bright red source associated with the radio source and the weaker dust component, and a weaker extension towards the west associated with the bright dust component. The Spitzer image shows a cluster of sources within the cold dust core.

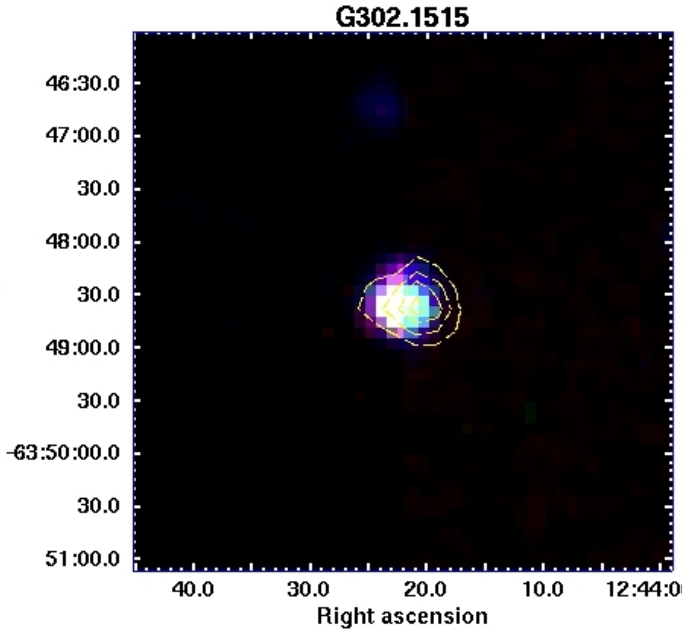

Figure 4b: MSX three color image

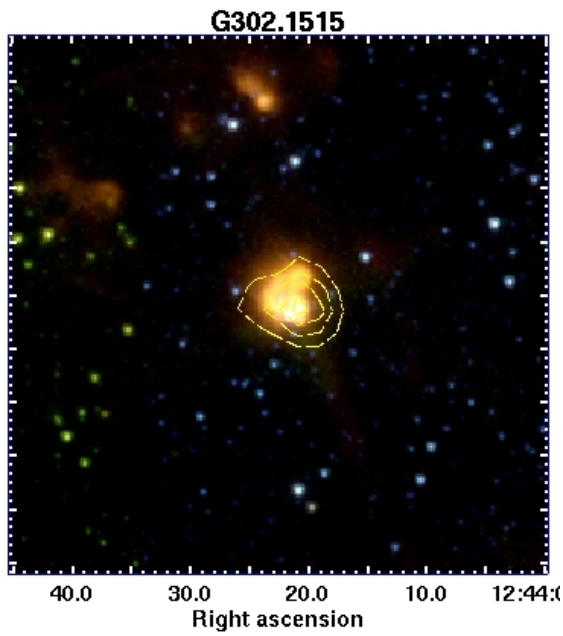

Figure 4c: Spitzer three color image

4.1.4 G308.9176+00.1231

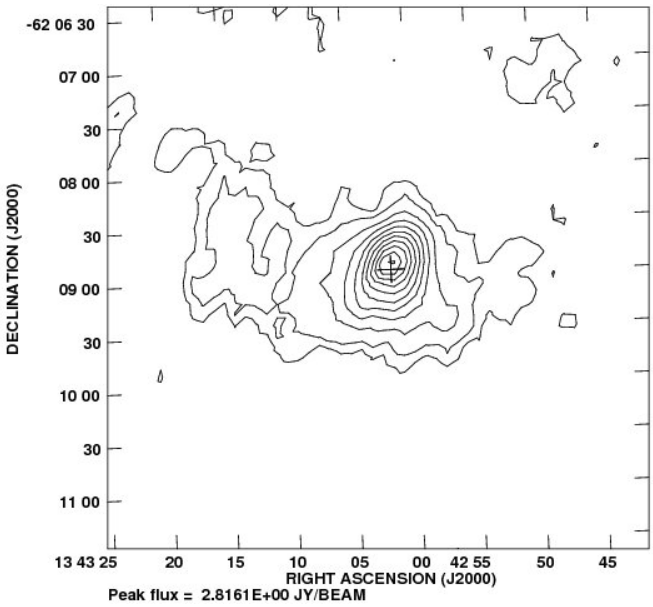

Figure 5a: 870 µm emission, contour levels iii

The 870 µm emission towards G308.9176+00.1231 arises from a single source showing a bright component within a filamentary structure extending about 3 arc-minutes. The total flux density and peak flux density are 11.68 Jy and 2.8 Jy/beam respectively. The map's rms noise is 50 mJy/beam. The radio source lies near the peak of the compact component.

The MSX image shows the presence of two sources with clear different colors: a northern source, prominent at the shortest wavelength, and a southern red source. In the Spitzer image the northern source is saturated. Due to its colors, this source is probably a foreground object.

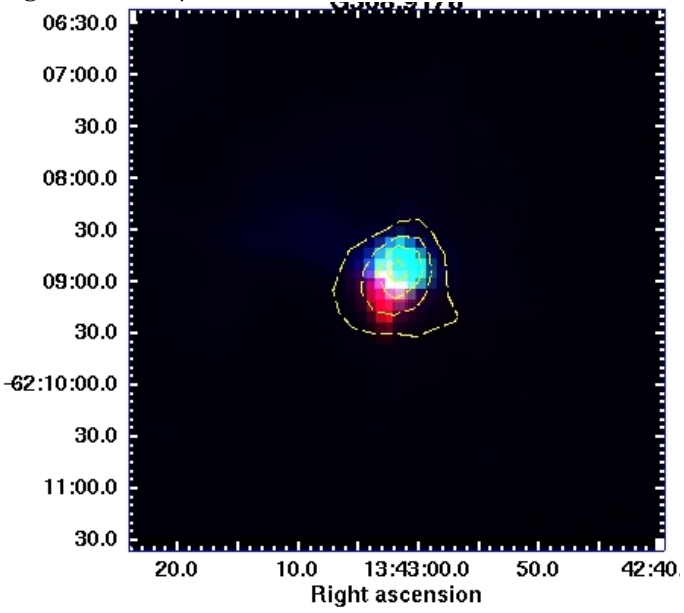

Figure 5b: MSX three color image

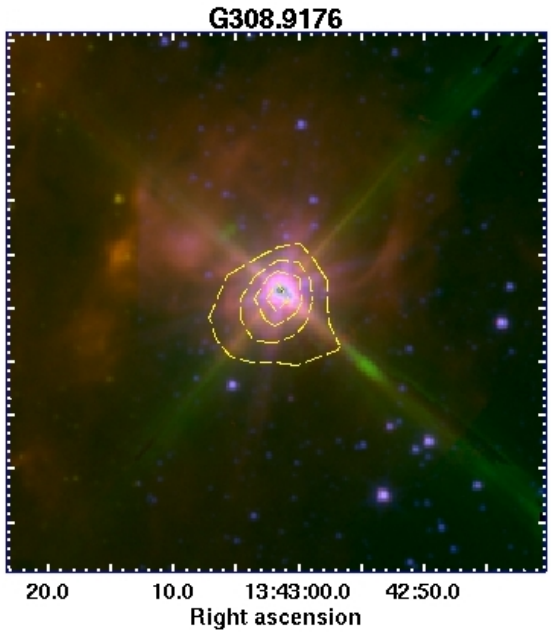

Figure 5c: Spitzer three color image

4.1.5 G311.1359-00.2372

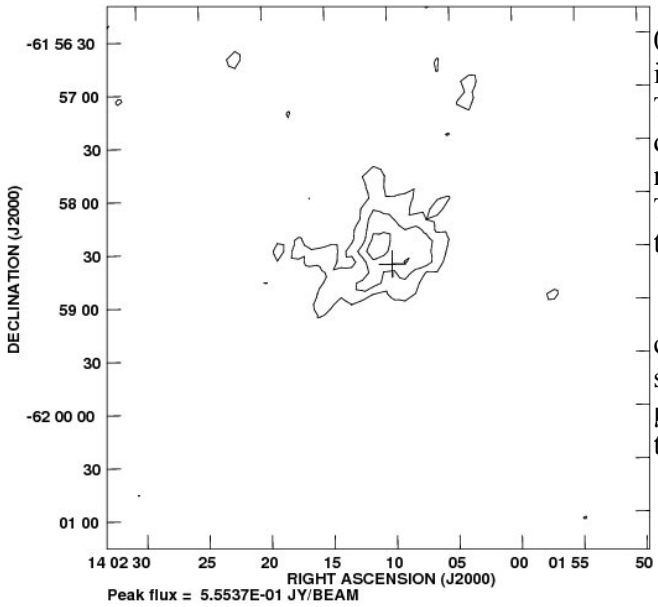

Figure 6a: 870 μm emission, contour levels: starting from 3-sigma (150 mJy/beam) and increasing in steps of 3-sigma

The 870 μm emission towards G311.1359-00.2372 arises from a single source with an irregular morphology, exhibiting two main peaks. The region's total flux density and peak flux density are 2.84 Jy and 0.555 Jy/beam respectively. The map's rms noise is 50 mJy/beam. The position of the radio source is in between those two peaks.

The MSX three color image shows a bright compact source coincident with the radio source surrounded by a weaker component prominent at 8 μm. The Spitzer image shows a couple of sources towards the center of the dust structure.

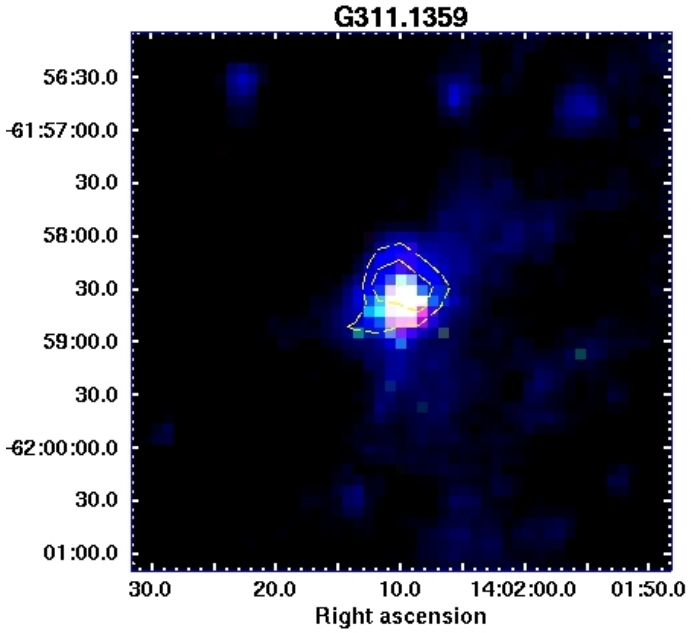

Figure 6b: MSX three color image

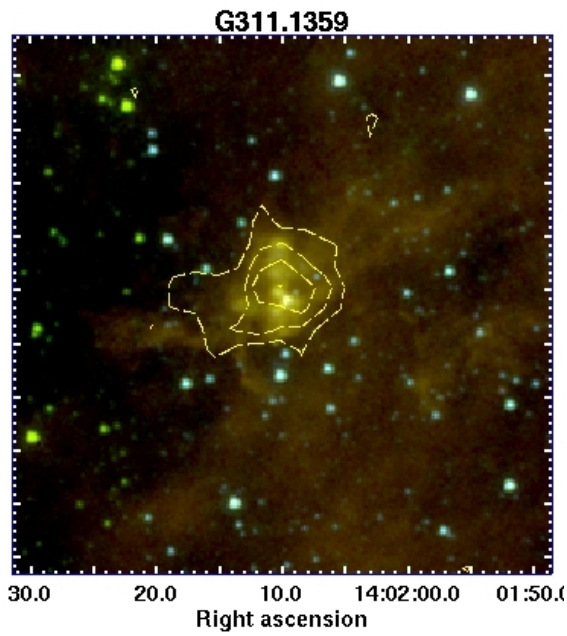

Figure 6c: Spitzer three color image

4.1.6 G317.4298-00.5612

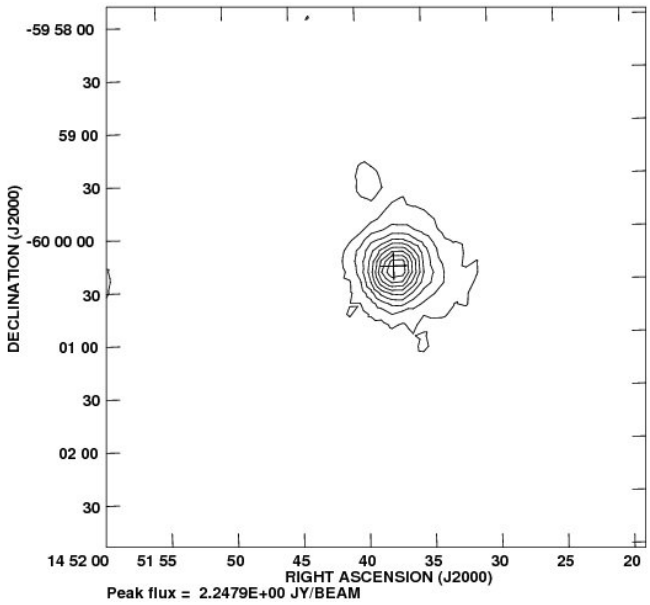

Figure 7a: 870 µm emission, contour levels iv

The 870 µm emission towards G317.4298-00.5612 arises from a single source with a centrally condensed morphology. The region's total flux density and peak flux density are 6.33 Jy and 2.25 Jy/beam respectively. The map's rms noise is 57 mJy/beam. The radio source lies at the peak of the dust core.

The MSX image shows a bright source coincident with the cold dust core. The Spitzer image shows a bright object at the center of the cold dust core.

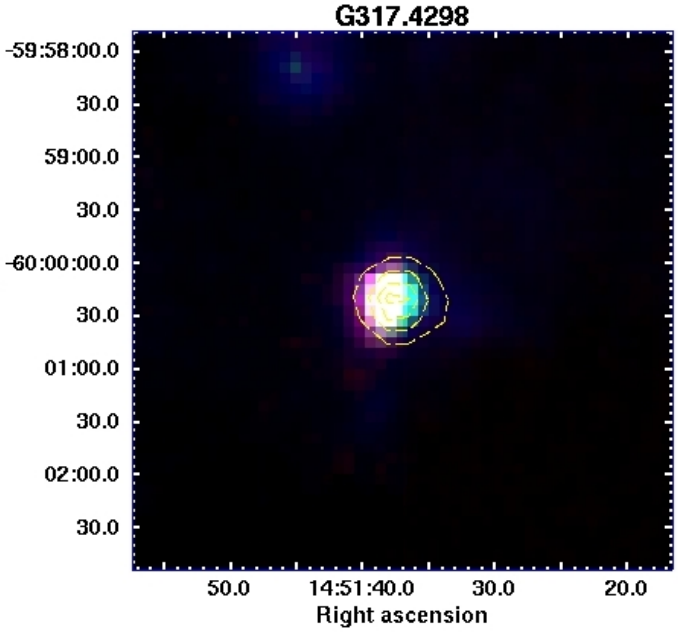

Figure 7b: MSX three color image

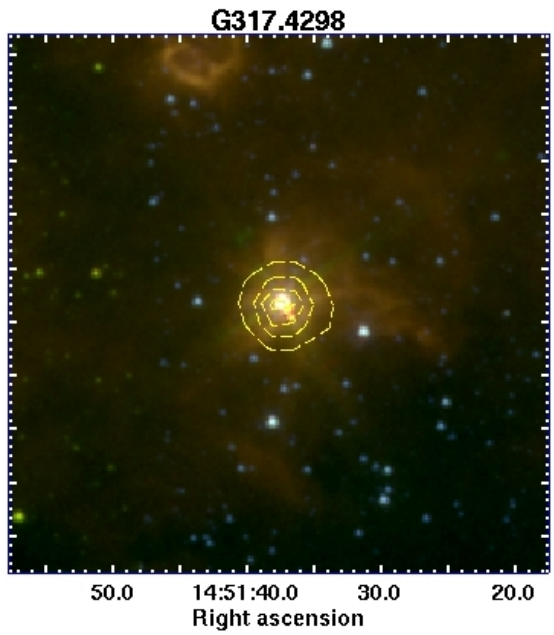

Figure 7c: Spitzer three color image

4.1.7 G317.8908-00.0578

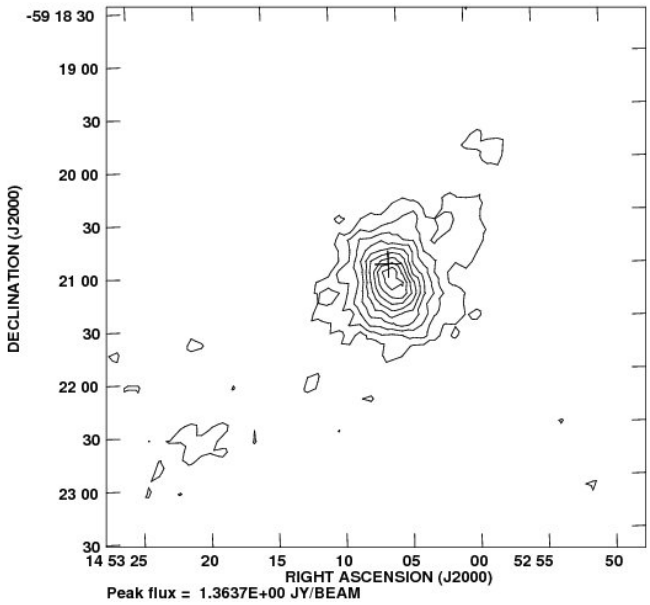

The 870 µm emission towards G317.8908-00.0578 arises from a single source with a Gaussian morphology. The region's total flux density and peak flux density are 4.64 Jy and 1.36 Jy/beam respectively. The map's rms noise is 50 mJy/beam. The radio source lies near the peak of the dust core.

The MSX image shows a bright source displaced to the northeast of the cold dust peak, and weak 8 µm extended emission. The Spitzer image shows an object in the position of the radio source, prominent at 8 µm.

Figure 8a: 870 µm emission, contour levels iv

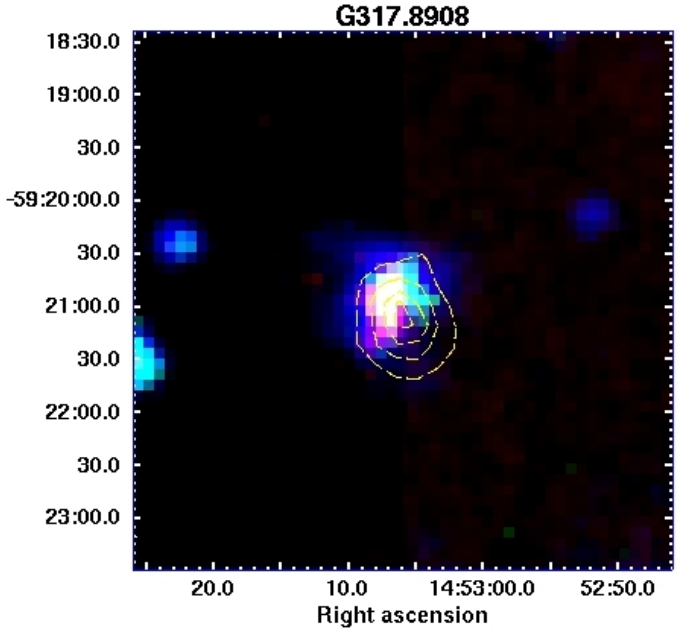

Figure 8b: MSX three color image

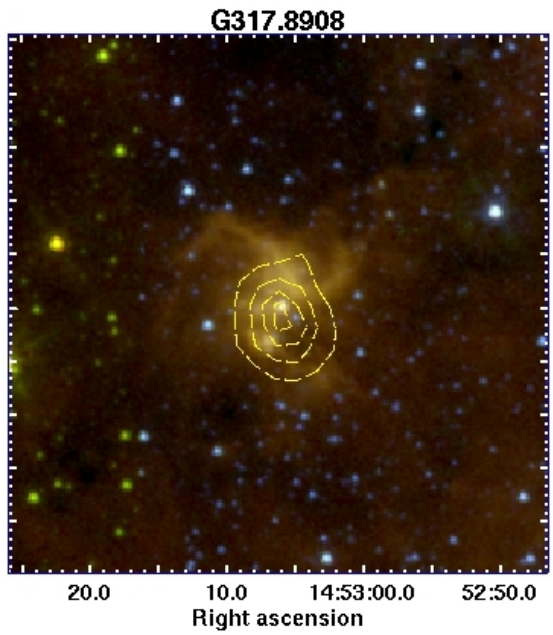

Figure 8c: Spitzer three color image

4.1.8 G326.5297-00.4186

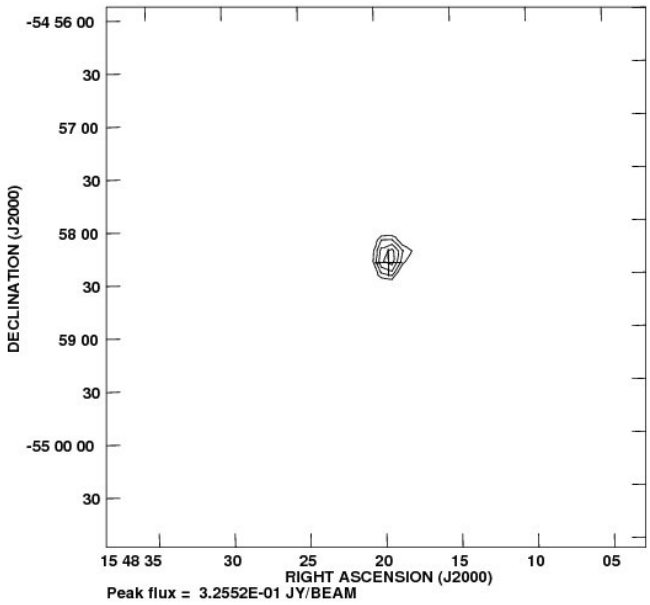

Figure 9a: 870 μm emission, contour levels, starting from 3-sigma (140 mJy/beam) and increasing in steps of 1-sigma (47 mJy/beam)

The 870 μm emission towards G326.5297-00.4186 arises from a single compact source, with a total flux density of 0.43 Jy. The peak flux density is 0.325 Jy/beam and the map's rms noise is 47 mJy/beam. The radio source lies near the peak of the compact core.

The MSX image shows an embedded bright object coincident with the 870 μm emission. The Spitzer image shows a very compact object in the center of the image.

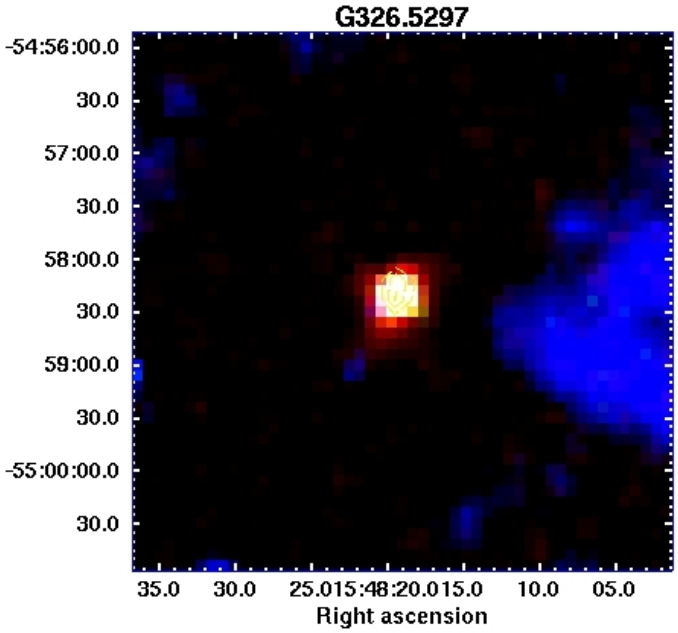

Figure 9b: MSX three color image

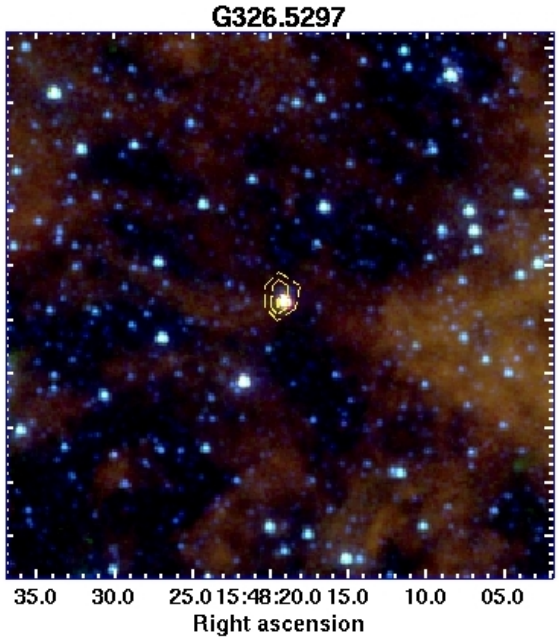

Figure 9c: Spitzer three color image

4.1.9 G326.7249+00.6159

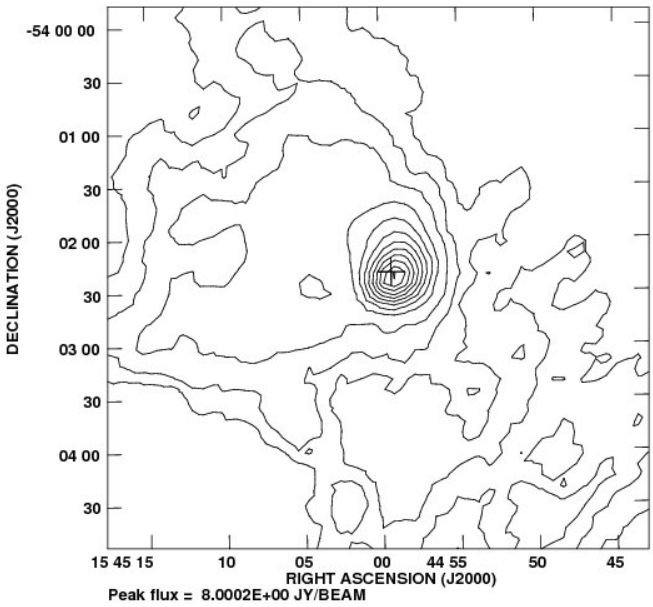

Figure 10a: 870 µm emission, contour levels ii

The 870 µm emission towards G326.7249+00.6159 exhibits a complex morphology with a bright compact component and a weak cometary component. The compact object has 27.33 Jy of total flux density, and the radio source lies in it's peak. The peak flux density is 8 Jy/beam and the map's rms noise is 44 mJy/beam.

The MSX image shows a bright object coincident with the cold dust core. The Spitzer image shows a bright object in the center of the image which exhibits a cometary morphology in the same direction as the 870µm emission.

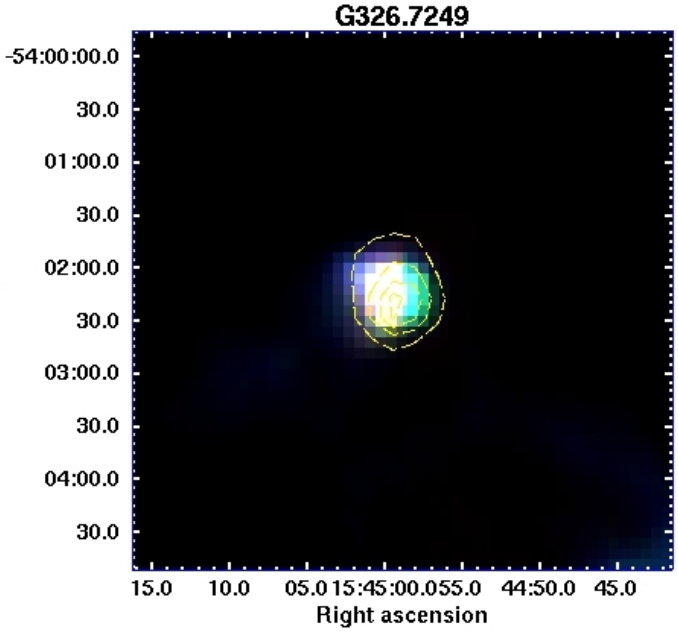

Figure 10b: MSX three color image

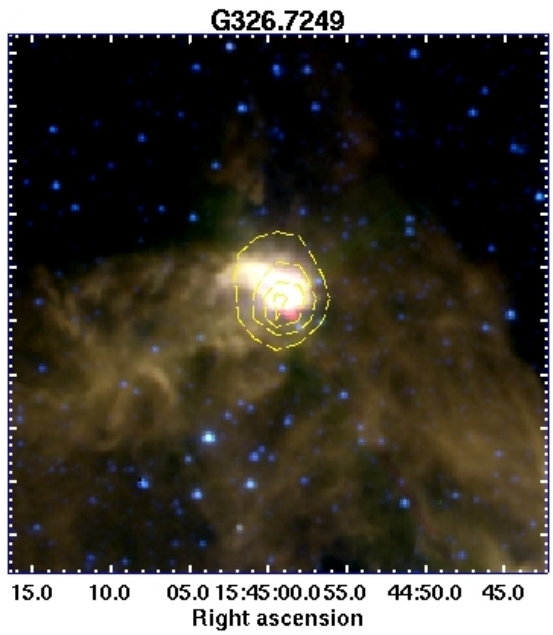

Figure 10c: Spitzer three color image

4.1.10 G329.4761+00.8414

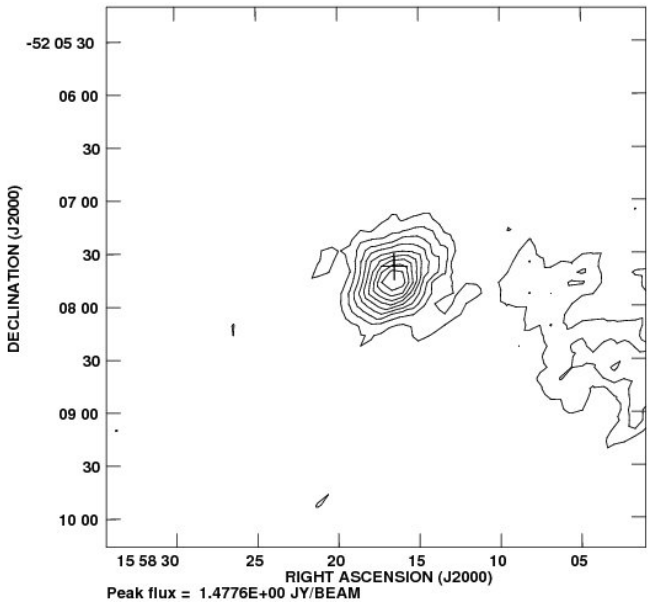

The 870 μm emission towards G329.4761+00.8414 arises from a single source with a Gaussian morphology, with a hint of a filament to the west. The radio source lies near the center of the central core, which has 4.86 Jy of total flux density. The region has a peak flux density of 1.47 Jy/beam and a rms noise of 48 mJy/beam.

The MSX image shows a bright core in the center of the image. The Spitzer image shows at least two objects within the cold dust core with the brighter one at the position of the radio source.

Figure 11a: 870 μm emission, contour levels iv

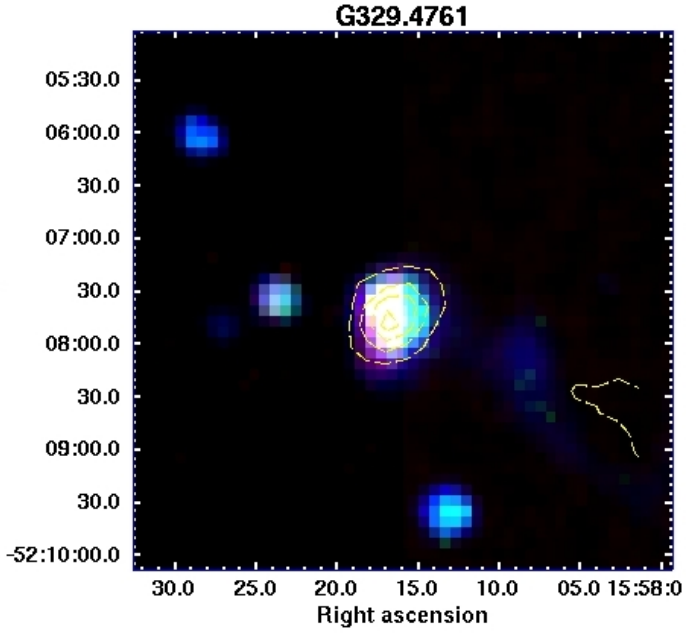

Figure 11b: MSX three color image

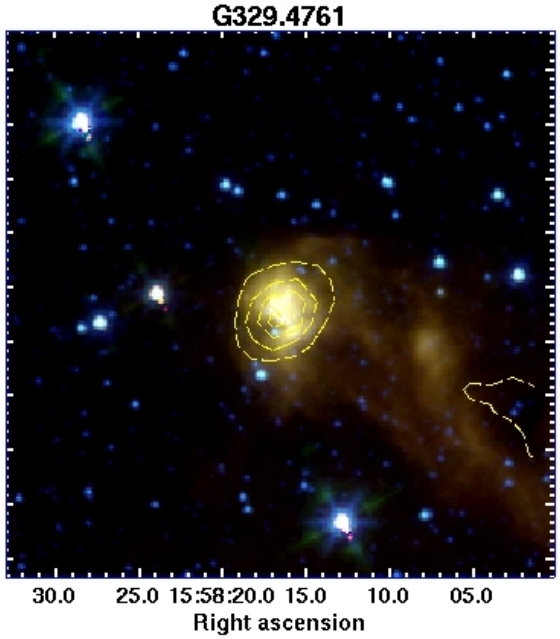

Figure 11c: Spitzer three color image

4.1.11 G330.2935-00.3946

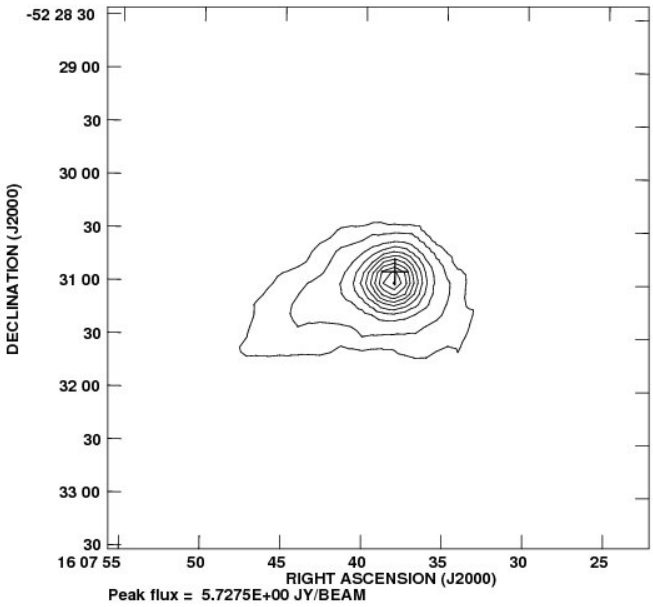

Figure 12a: 870 µm emission, contour levels iii

The 870 µm emission towards G330.2935-00.3946 arises from a single source with a centrally condensed morphology and a weak extended component. The total flux density and peak flux density are 16.47 Jy and 5.73 Jy/beam respectively. The map's rms noise is 50 mJy/beam. The radio source lies near the peak of the dust core.

The MSX bands show a compact core associated with the 870 µm emission. On the other hand the Spitzer image shows several compact sources, a cluster, at the center of the dust core that are surrounded by 8 µm emission.

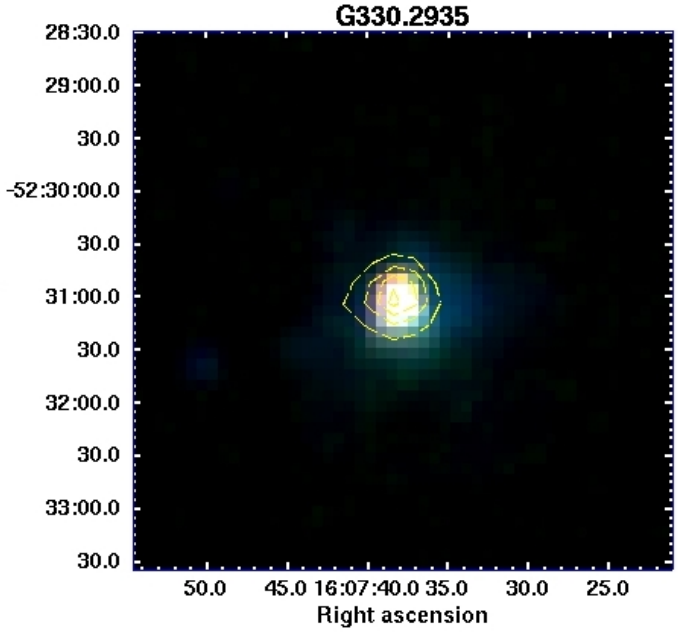

Figure 12b: MSX three color image

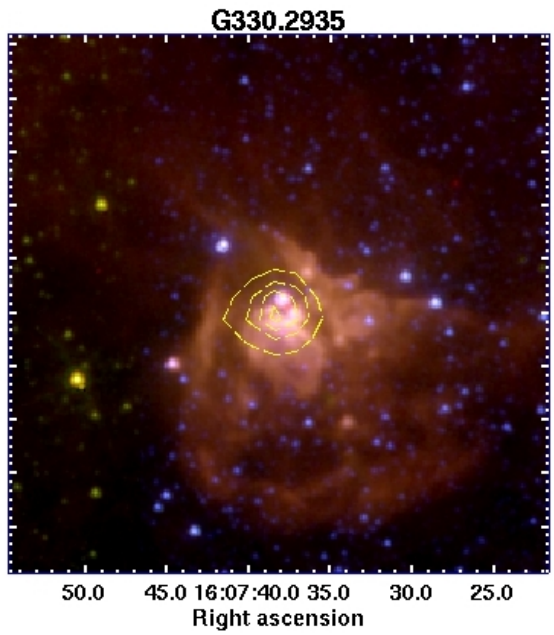

Figure 12c: Spitzer three color image

4.1.12 G332.8256-00.5498

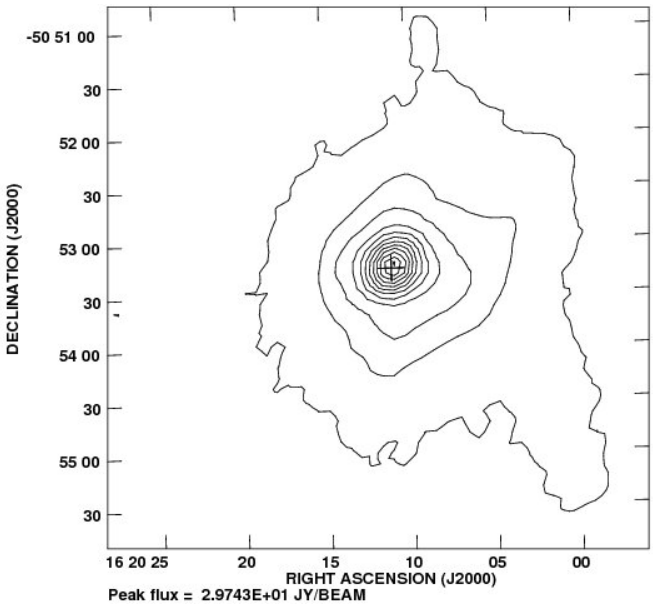

Figure 13a: 870 µm emission, contour levels i

The 870 µm emission towards G332.8256-00.5498 arises from a single source exhibits a centrally condensed component and a weak envelope extending a couple of arc-minutes. The core's (up to 2% of peak contour) total flux density and peak flux density are 97.2 Jy and 29.7 Jy/beam respectively. The map's rms noise is 53 mJy/beam. The radio source lies in the core's peak.

The MSX color image shows four objects in the field of view. Near the center of the image there is a bright red object, which coincides with the radio source, and two weaker objects seen towards the southwest and northeast in opposite directions of the bright object. The Spitzer resolution allows to separate the components and it confirms the presence of a bright compact object in the position of the radio source.

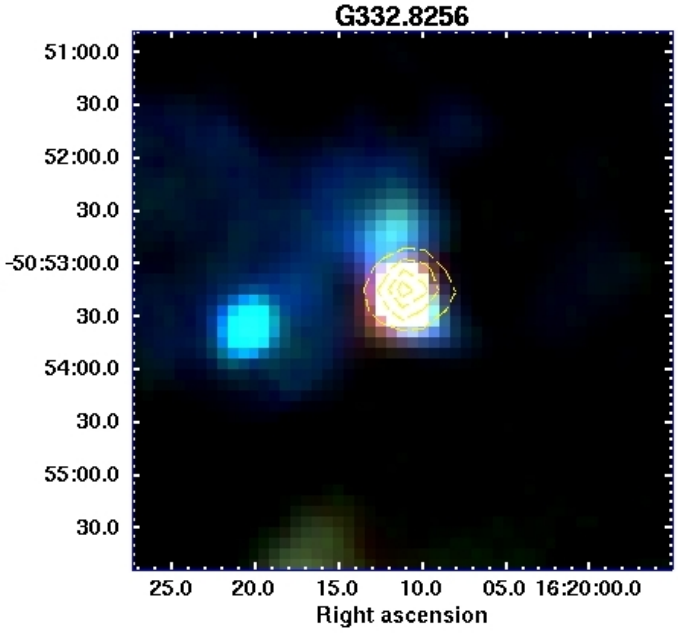

Figure 13b: MSX three color image

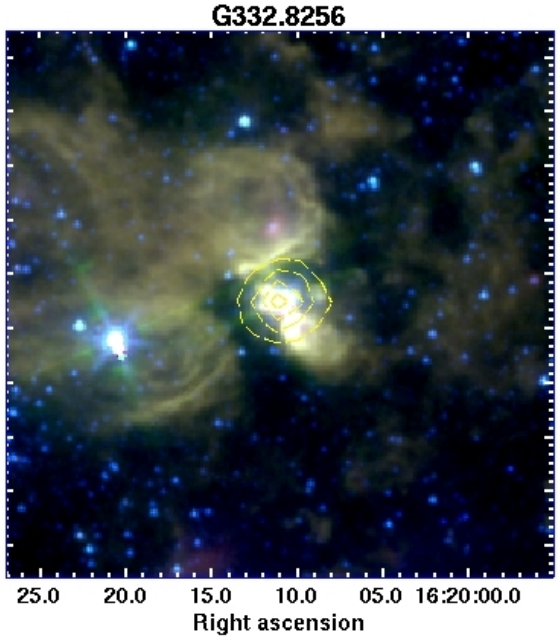

Figure 13c: Spitzer three color image

4.1.13 G333.0162+00.7615

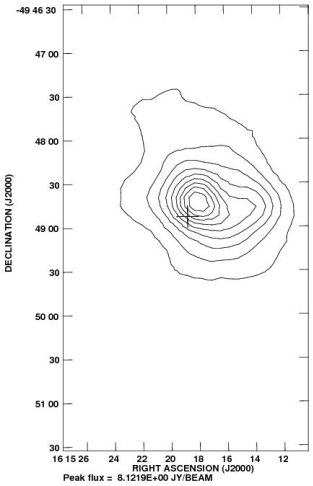

Figure 14a: 870 μm emission, contour levels iv

The 870 μm emission towards G333.0162+00.7615 arises from a single extended object possibly consisting of a bright core towards the east and a weaker core towards the west. The region's total flux density is 48.49 Jy, the peak flux density is 8.12 Jy/beam and the map's rms noise is 195 mJy/beam. The radio source lies 15" apart from the dust peak.

The MSX image shows a complex environment with several compact objects in the vicinity. The brightest and redder object is coincident with the radio source. The Spitzer image shows a bright object coincident with the radio source.

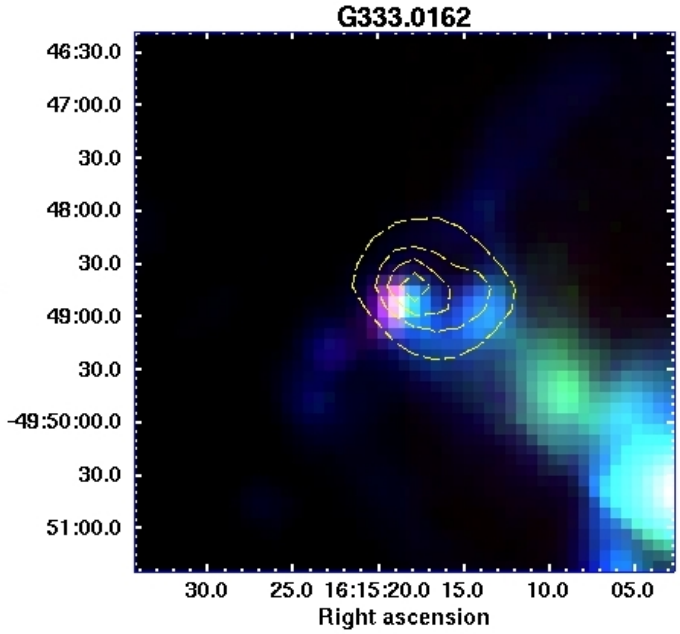

Figure 14b: MSX three color image

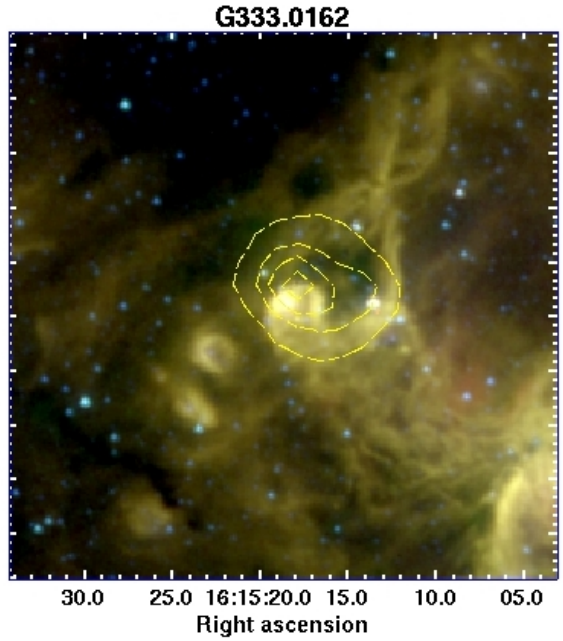

Figure 14c: Spitzer three color image

4.1.14 G333.1306-00.4275

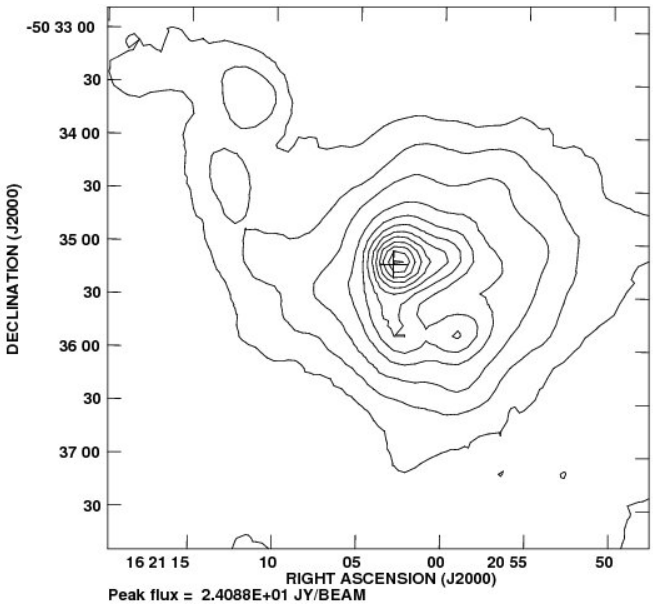

Figure 15a: 870 µm emission, contour levels ii

The 870 µm emission towards G333.1306-00.4275 arises from a complex morphology. The central regions exhibits three peaks (the peak flux of the fainter one is 40% of the brightest) within an extended envelope. The region's total flux density and peak flux density are 128 Jy, 24 Jy/beam respectively. The map's rms noise is 83 mJy/beam. The envelope has an angular size of ~ 3', and there is a tail that goes out of the envelope which itself has a few peaks within it. The radio source lies near the center of the brighter object in the map.

The MSX image shows a bright source towards the west of the cold dust peak and a weaker, redder object, that is coincident with the radio source. The Spitzer image shows extended 5-8µm emission and several compact objects within. One of these objects is associated with the radio source position, and another two are coincident with the MSX bright source.

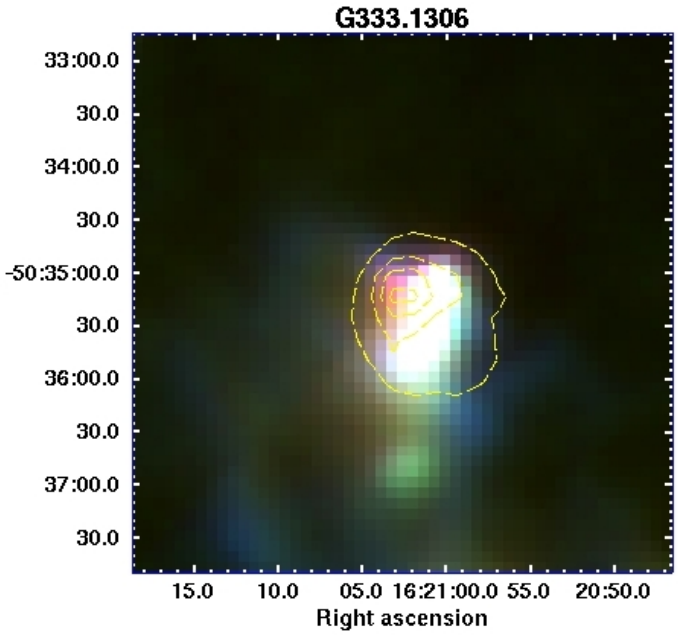

Figure 15b: MSX three color image

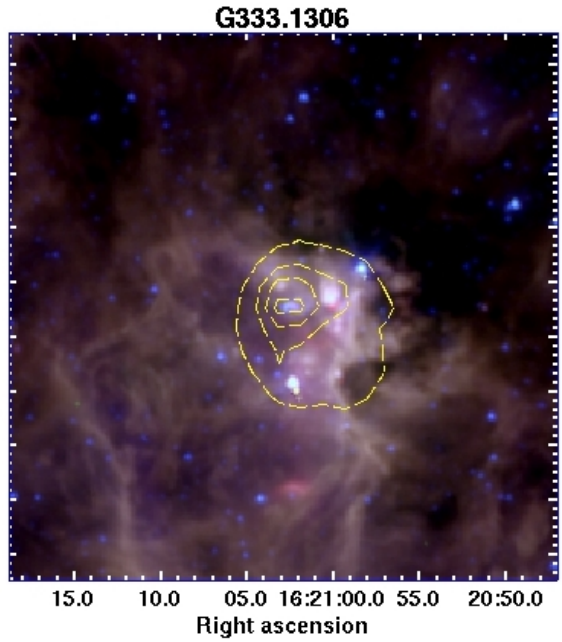

Figure 15c: Spitzer three color image

4.1.15 G336.9842-00.1835

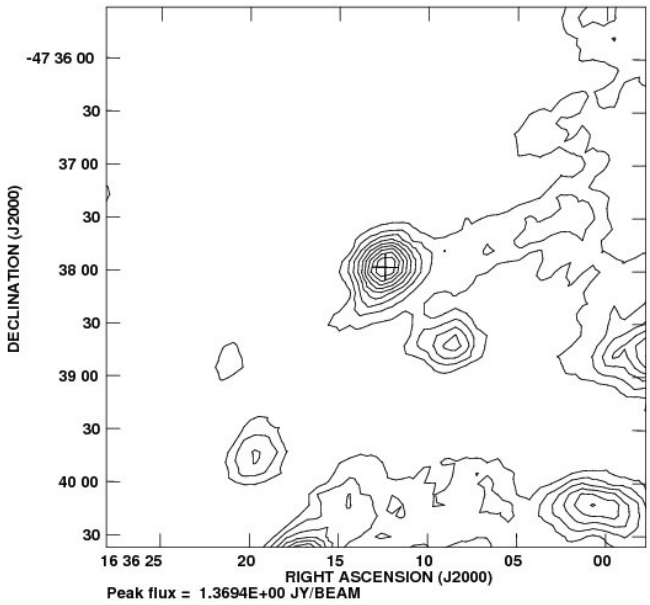

The 870 μm emission seen towards G336.9842-00.1835 is complex, consisting of a bright compact object at the center of the image, coincident with the radio source, and a few other compact objects as well as filamentary structures. The bright core's flux density and peak flux density are 4.73 Jy and 1.37 Jy/beam respectively. The map's rms noise is 41 mJy/beam respectively. The radio source is in the center of this dust core.

The MSX image shows a bright object coincident with the bright cold dust core. The Spitzer image shows a bright compact object at the position of the radio source.

Figure 16a: 870 μm emission, contour levels iv

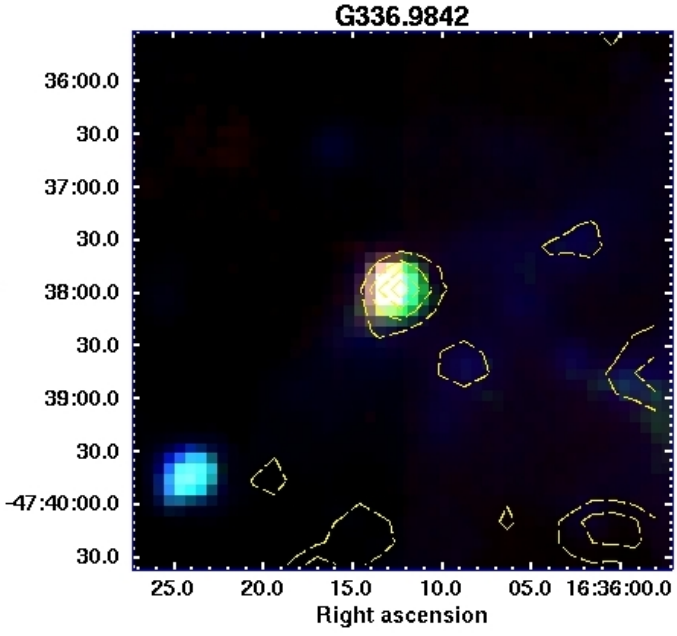

Figure 16b: MSX three color image

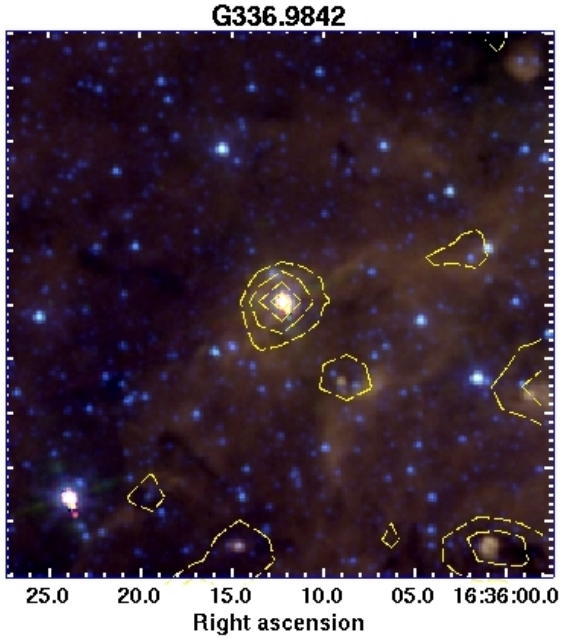

Figure 16c: Spitzer three color image

4.1.16 G337.4032-00.4037

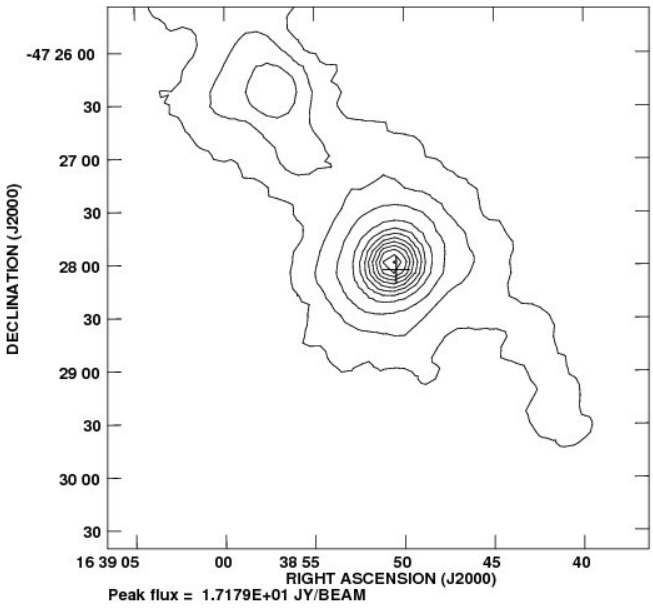

Figure 17a: 870 µm emission, contour levels ii

The 870 µm emission towards G337.4032-00.4037 arises from two compact sources within a filament: a bright central source with a centrally condensed morphology and associated with the radio source, and a weaker object about ~ 2' to the northeast. This core's (up to 10% of peak contour) flux and peak flux density are 51.96 Jy and 17.2 Jy/beam respectively. The map's rms noise is 67 mJy/beam.

The MSX image shows two bright objects and the filamentary structure. The brightest MSX object is associated with the radio source, and to the east of it there is a red component. The Spitzer image shows a compact bright object at the position of the radio source, while the embedded MSX object to the east is seen to divide into two different components. A bright emission is seen at the weaker 870 µm core position.

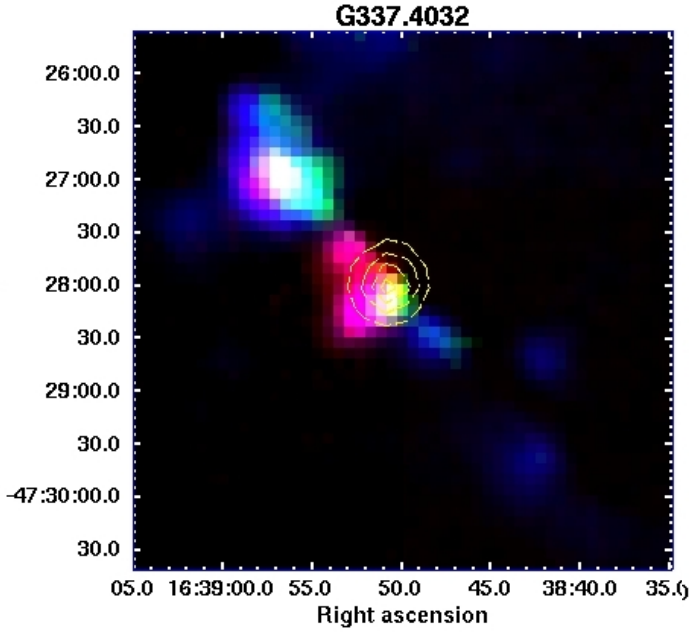

Figure 17b: MSX three color image

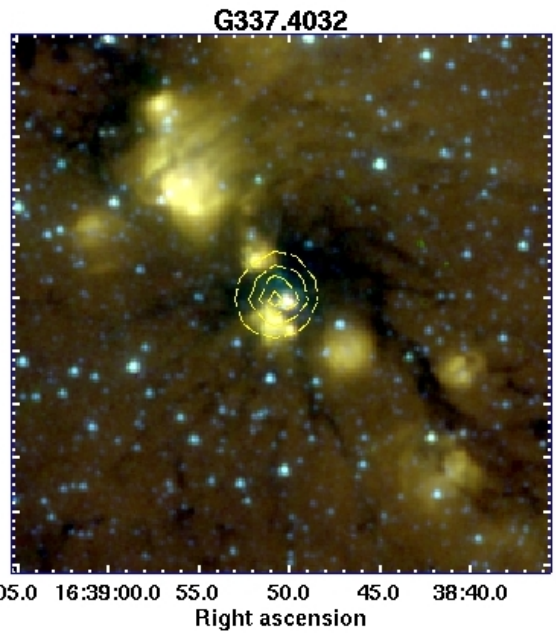

Figure 17c: Spitzer three color image

4.1.17 G337.7051-00.0575

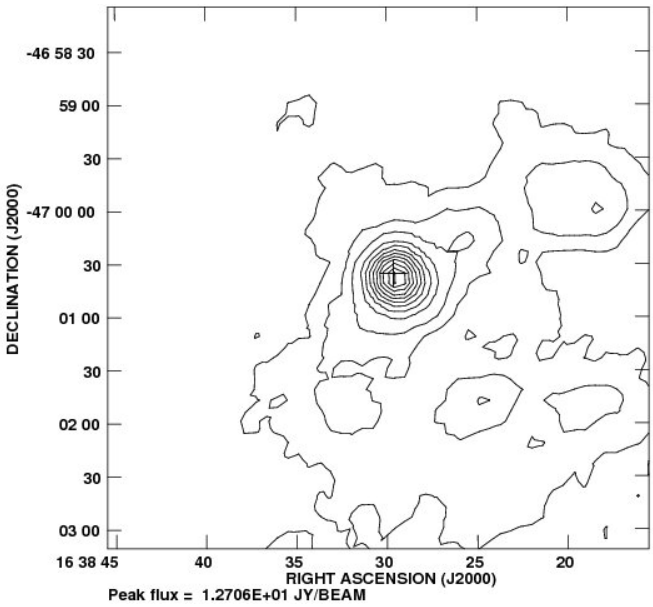

Figure 18a: 870 µm emission, contour levels ii

The 870 µm emission towards G337.7051-00.0575 is complex, arising from a compact object with a centrally condensed morphology, and an extended irregular envelope. The bright core has 35.34 Jy of total flux density and the radio source falls in the center of it. At the 2-5% of peak flux contours the envelope extends more than 2 arc-minutes away. The region's peak flux density is 12.7 Jy/beam and the map's rms noise is 68 mJy/beam.

The MSX image shows a bright object slightly offset to the east of the cold dust core. The Spitzer image shows an extended object, prominent at 8 µm emission, coincident with the MSX object.

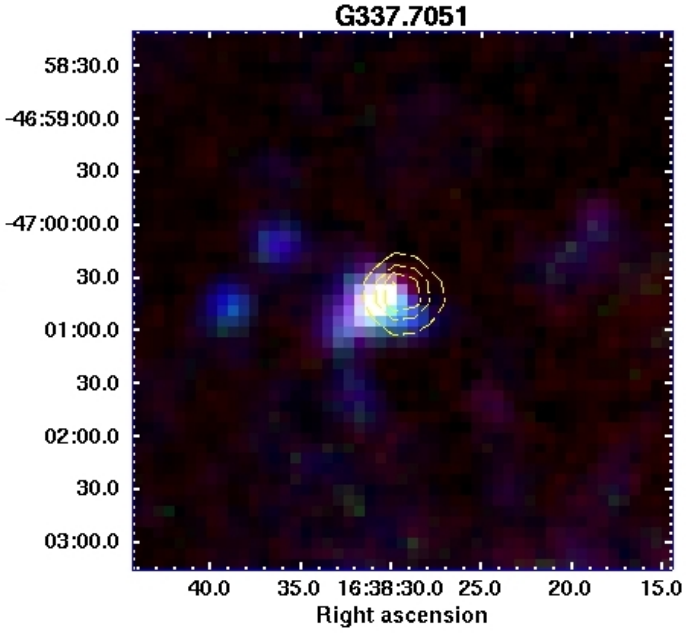

Figure 18b: MSX three color image

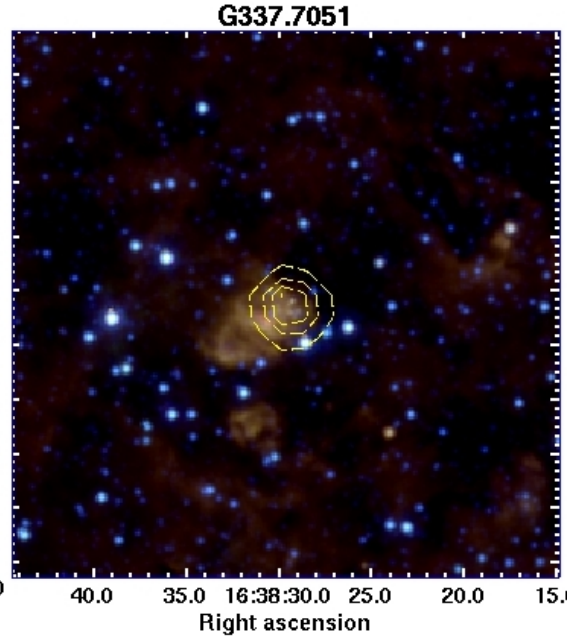

Figure 18c: Spitzer three color image

4.1.18 G337.7091+00.0932

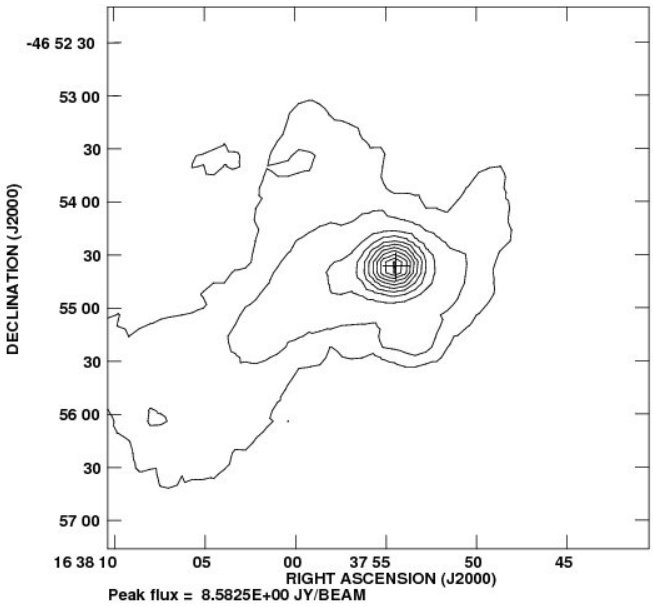

Figure 19a: 870 µm emission, contour levels iii

The 870 µm emission towards G337.7091+00.0932 arises from a compact bright source, a weak extended structure with a filamentary-like morphology. The total flux density of the core is 24.67 Jy and the peak flux density is 8.6 Jy/beam. The rms noise is 64 mJy/beam. The radio source lies at the peak of the compact dust source.

The MSX image shows two objects near the center of the image, a bright red object and a weaker red object associated with the radio source. The Spitzer image shows weak emission coincident with the two MSX objects.

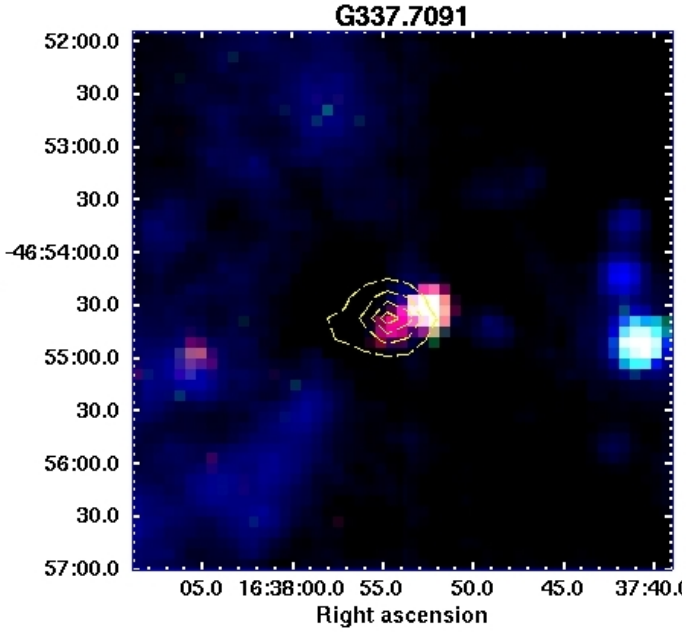

Figure 19b: MSX three color image

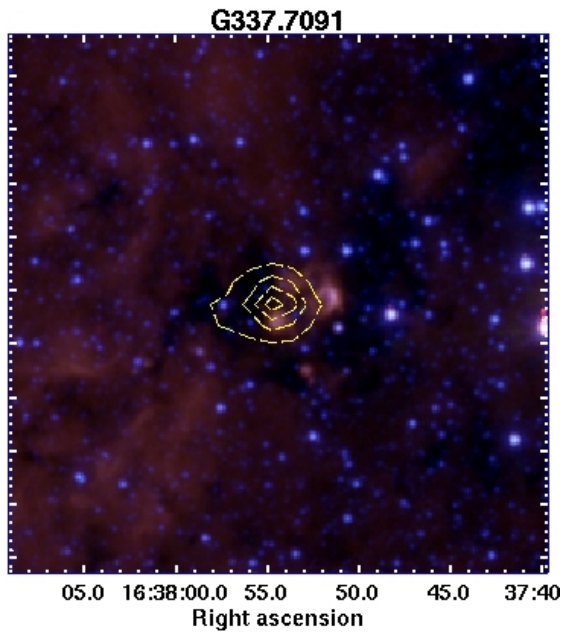

Figure 19c: Spitzer three color image

4.1.19 G337.8442-00.3748

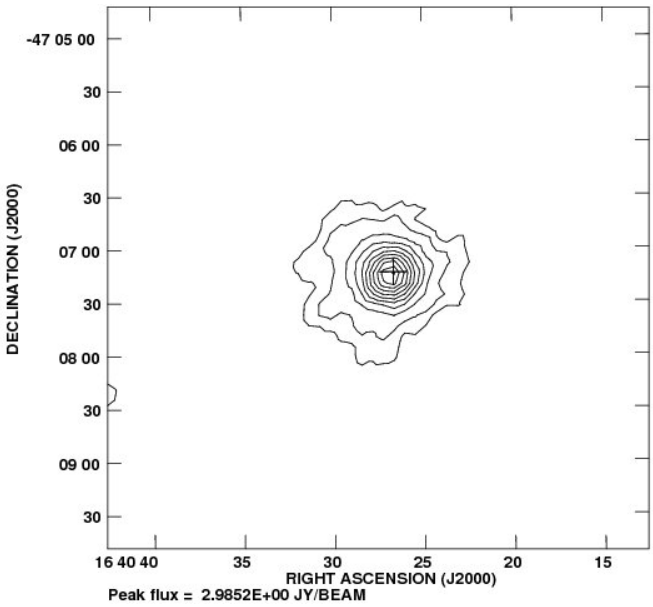

The 870 µm emission towards G337.8442-00.3748 arises from a single source with a centrally condensed morphology. The core's total flux density and peak flux density are 9.42 Jy and 2.98 Jy/beam respectively. The map's rms noise is 41 mJy/beam. The radio source lies in the center of the core.

The MSX image shows a bright compact object associated with the cold dust core. The Spitzer image shows a bright central object coincident with the cold dust peak. There is also a 8µm source that extends well beyond the 870 µm emission.

Figure 20a: 870 µm emission, contour levels iii

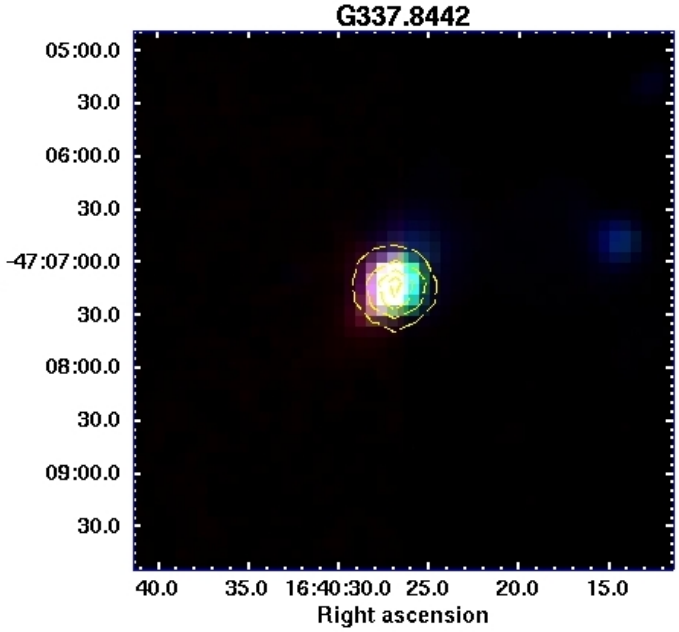

Figure 20b: MSX three color image

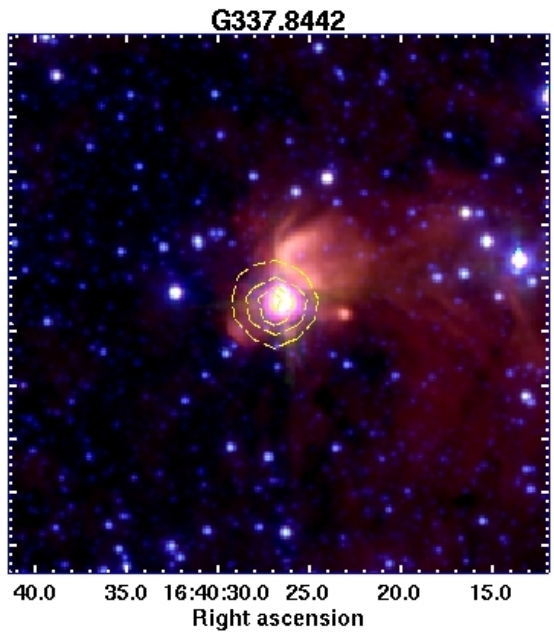

Figure 20c: Spitzer three color image

4.1.20 G338.9217+00.6233

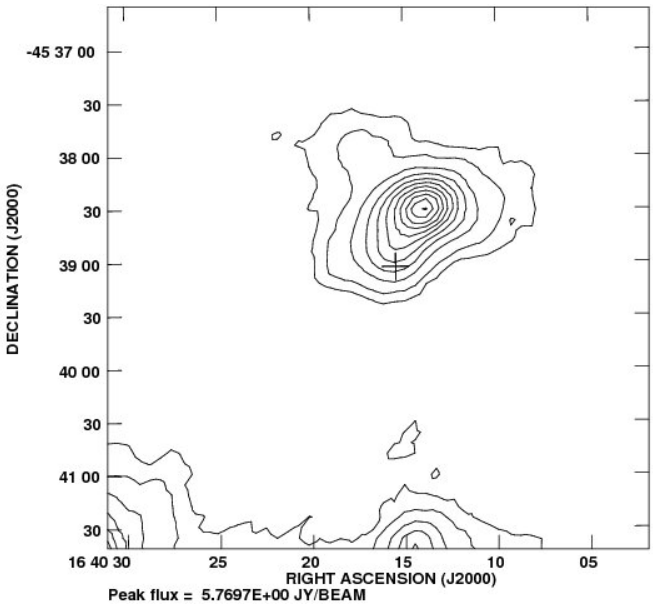

Figure 21a: 870 μm emission, contour levels iii

The 870 μm emission towards G338.9217+00.6233 arises from a single source with an irregular kidney-like morphology. The core's total flux density is 28.85 Jy. The region's peak flux density is 5.8 Jy/beam and the map's rms noirse is 65 mJy/beam respectively. The radio source is located ~35" from the peak of the dust emission.

The MSX image shows a bright object, associated with the radio source, and extended components towards the north, prominent at 8 μm, and towards the southeast, prominent at the longer wavelengths. The Spitzer image shows a bright compact object associated with the radio source, and a 8 μm extended emission. In both images, no emission is detected towards the sub-mm peak suggesting it is an infrared dark cloud (IRDC).

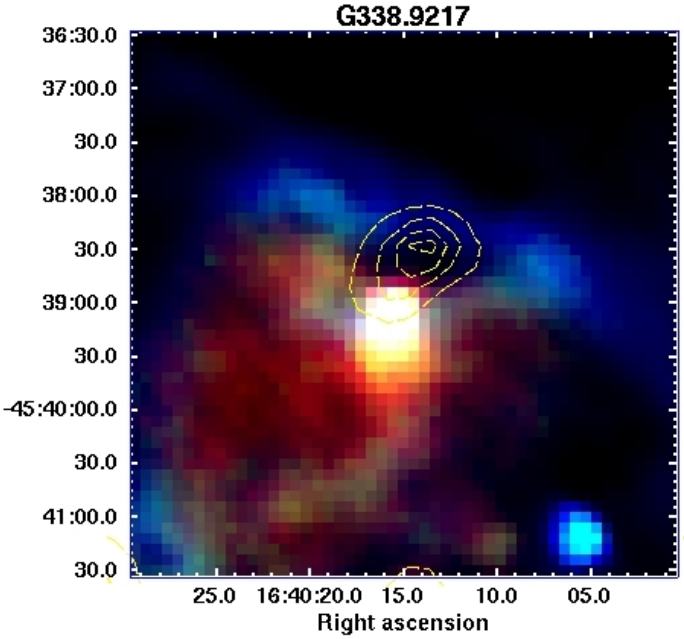

Figure 21b: MSX three color image

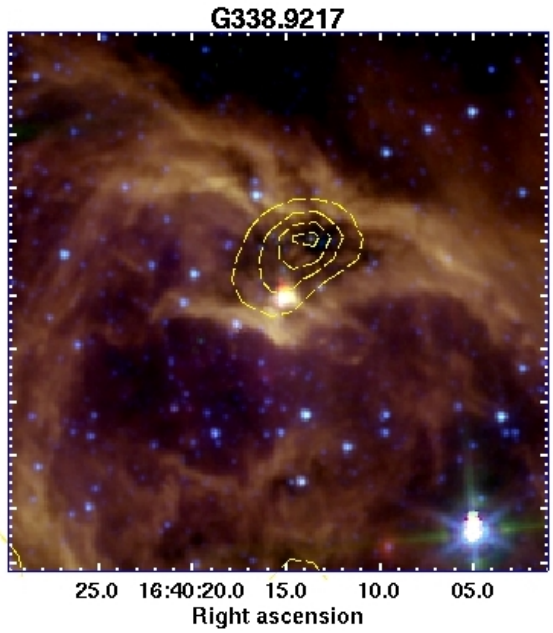

Figure 21c: Spitzer three color image

4.1.21 G340.2480-00.3725

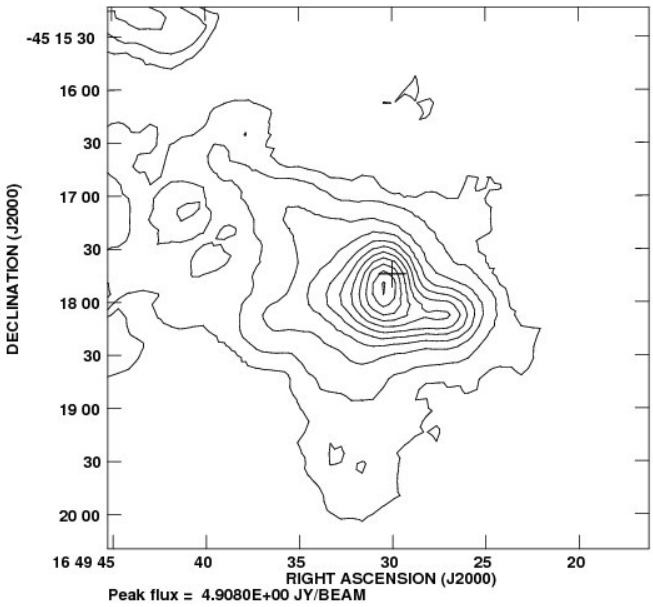

The 870 µm emission towards G340.2480-00.3725 has a complex morphology exhibiting two compact cores,and a weak, irregular and extended envelope. The central region's (up to 20% of peak contour) total flux density and peak flux density are 32.1 Jy and 4.9 Jy/beam respectively. The map's rms noise is 76 mJy/beam. The radio source lies ~15" from the bright dust peak.

The MSX image shows two objects within the cold dust structure. A red central component associated with the radio source and a blue component ~45" towards the southwest. The Spitzer image shows a handful of compact objects within the cold dust core associated with the MSX objects.

Figure 22a: 870 µm emission, contour levels iii

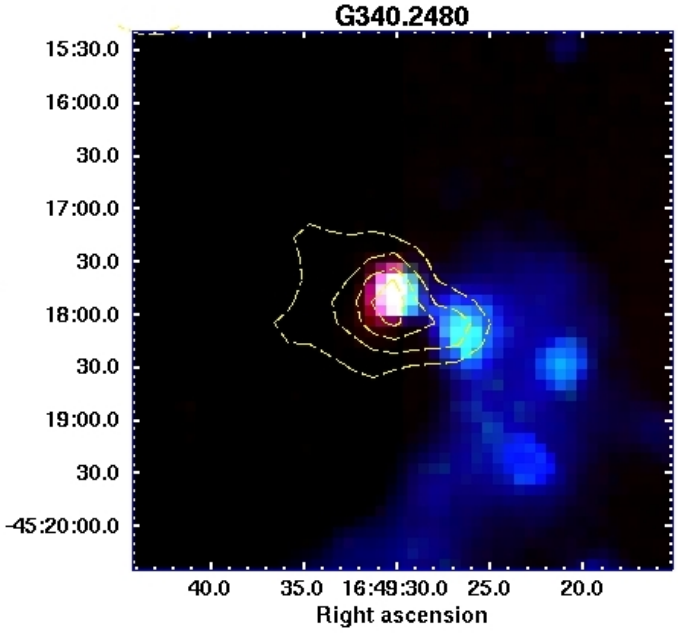

Figure 22b: MSX three color image

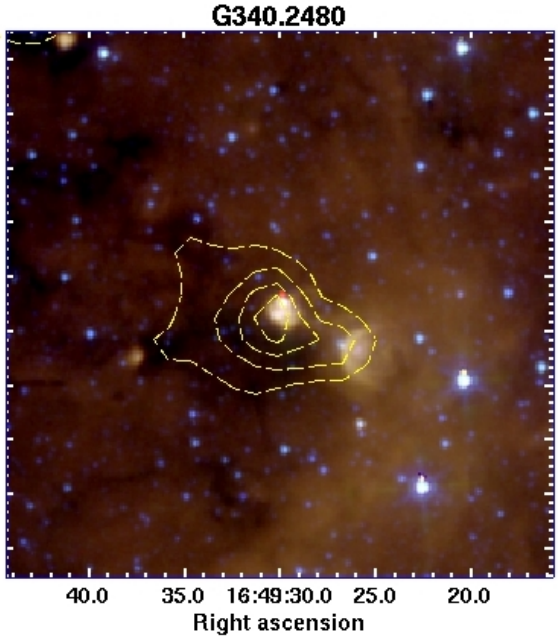

Figure 22c: Spitzer three color image

4.1.22 G345.4938+01.4677

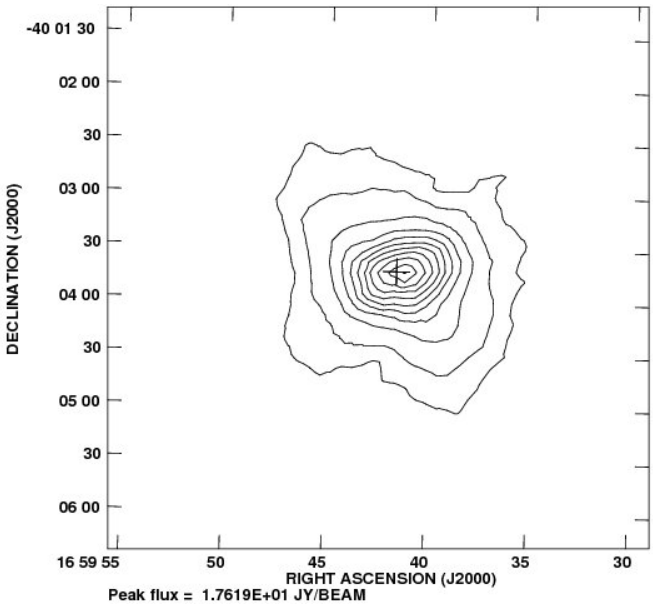

The 870 μm emission towards G345.4938+01.4677 arises from a single extended object. The total flux density is 132.82 Jy, and the peak flux density is 17.6 Jy/beam. The map's rms noise is 110 mJy/beam. The radio source lies near the center of the dust core.

The MSX image shows a bright object associated with the sub-mm emission. The Spitzer image shows a complex morphology with a central bright object that is saturated in the four IRAC bands. The 8μm emission extends mainly to the east of the source.

Figure 23a: 870 μm emission, contour levels iii

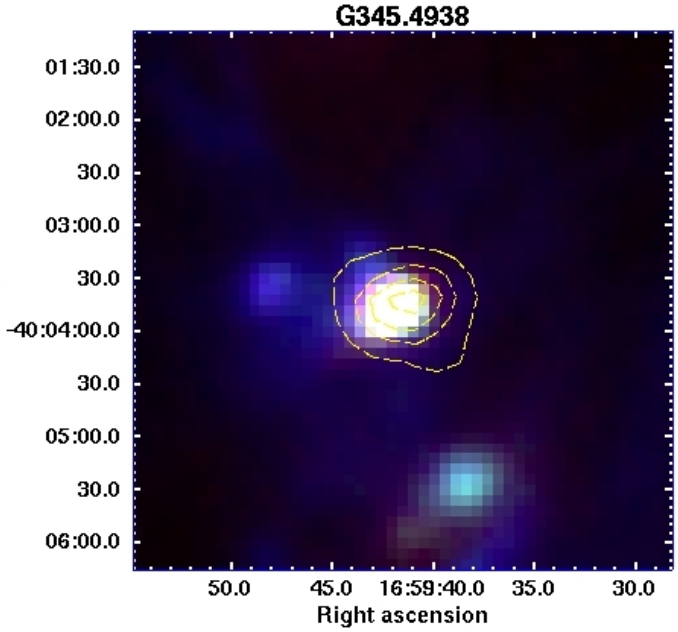

Figure 23b: MSX three color image

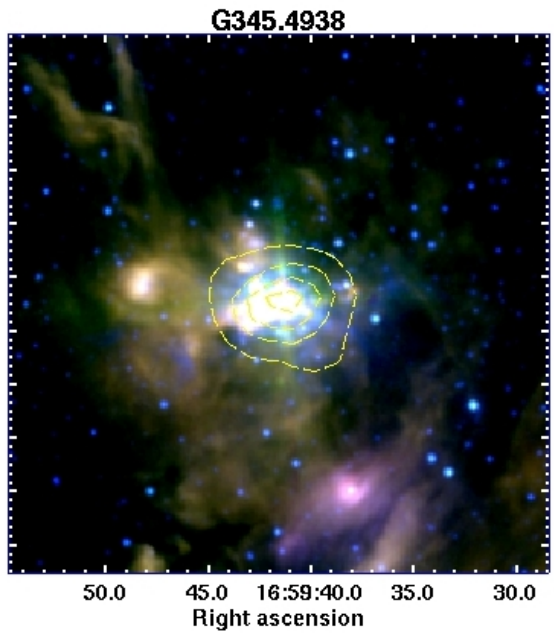

Figure 23c: Spitzer three color image

4.1.23 13134-6242

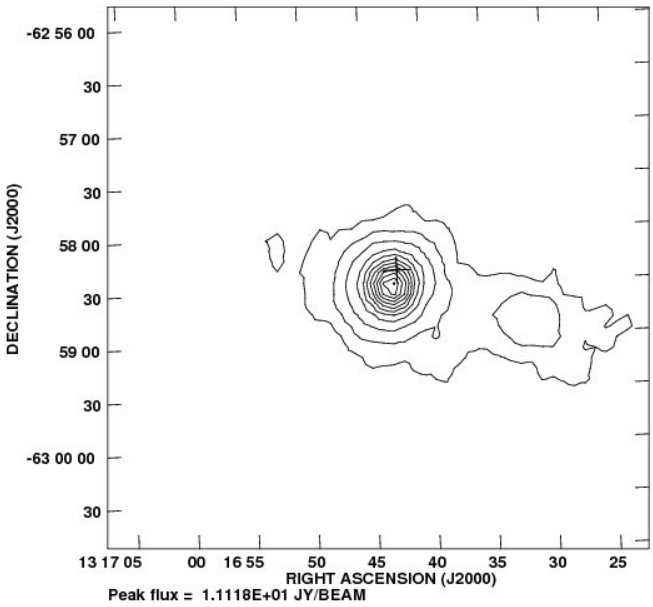

Figure 24a: 870 µm emission, contour levels ii

The 870 µm emission towards 13134-6242 arises from a bright object exhibiting a centrally condensed morphology and a weaker object located ~80" to the southwest. The bright compact core has a flux of 23.65 Jy. The peak flux density is 11.1 Jy/beam and map's rms noise is 60 mJy/beam. The radio source lies within the bright core at ~15" from its center.

The MSX image shows two sources within the bright core: a red object associated with the north part of the cold dust core (where the radio source lies), and a bright bluer object towards the south. The Spitzer image shows two 8 µm dominated objects associated with each of the MSX components.

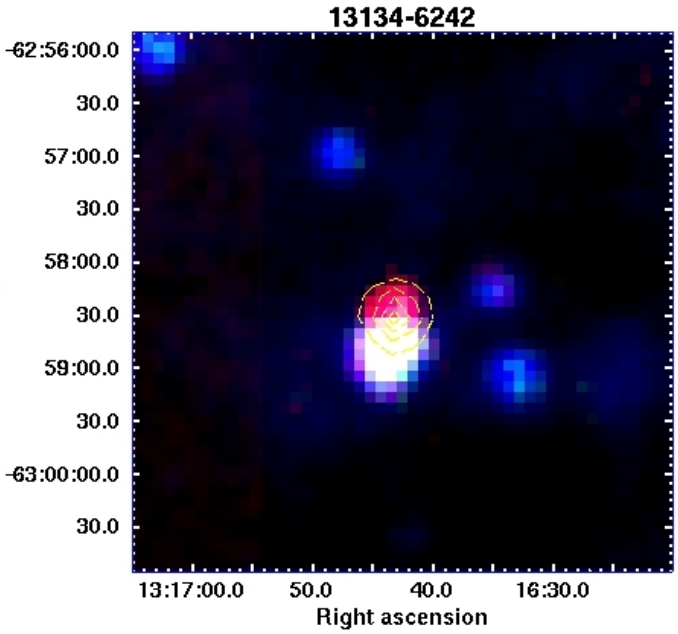

Figure 24b: MSX three color image

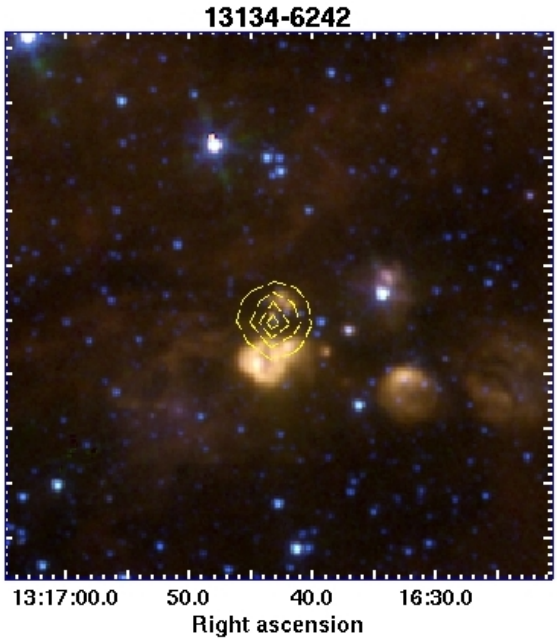

Figure 24c: Spitzer three color image

4.1.24 13471-6120

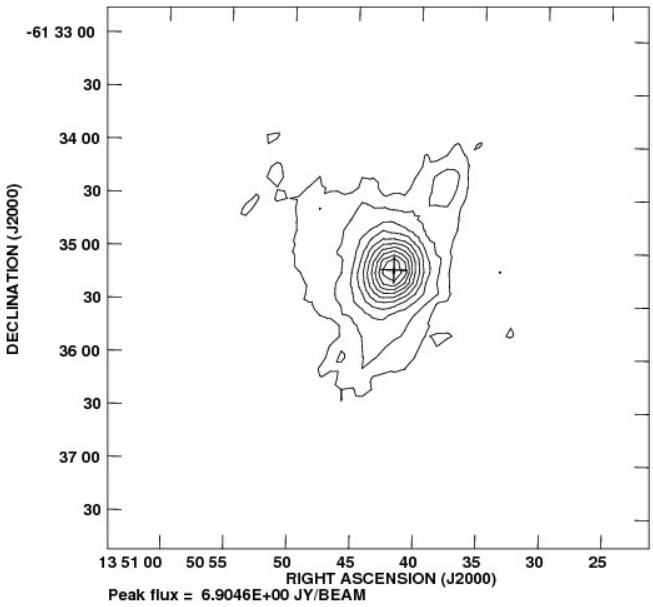

Figure 25a: 870 μm emission, contour levels iii

The 870 μm emission towards 13471-6120 arises from a single object which shows a centrally condensed component and a weak extended component. The central region's total flux density and peak flux density are 22.81 Jy and 6.9 Jy/beam respectively. The map's rms noise is 84 mJy/beam. The radio source lies at the peak of the compact component.

The MSX image shows a bright object coincident with the cold dust core. The west side of the source seems to have an 8μm excess, while the east seems to be dominated by the longer wavelengths. The Spitzer shows a very bright compact object at the center of the image, which is saturated in all IRAC bands.

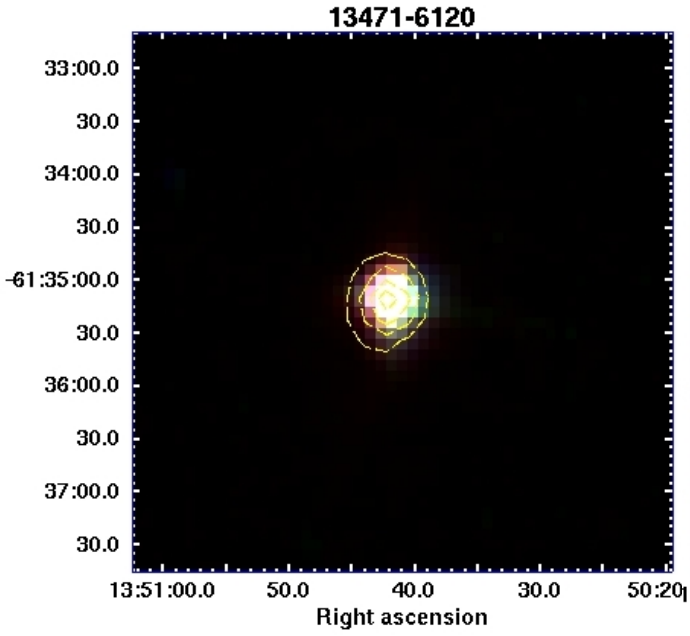

Figure 25b: MSX three color image

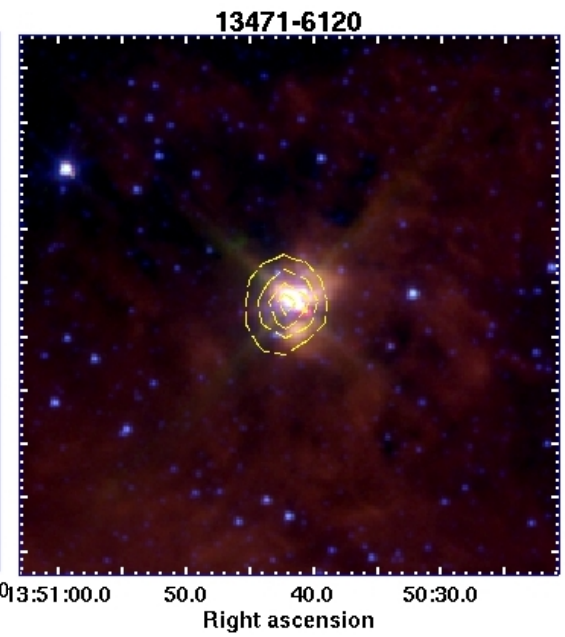

Figure 25c: Spitzer three color image

4.1.25 15437-5343

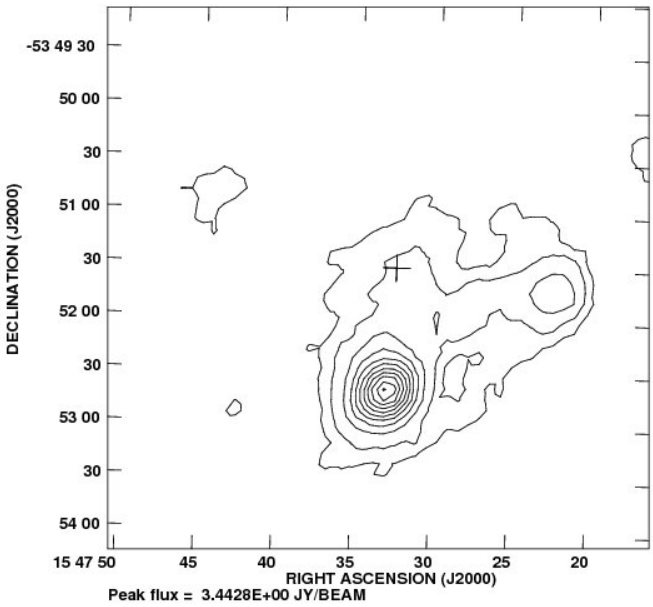

Figure 26a: 870 μm emission, contour levels iii

The 870μm emission towards 15437-5343 exhibits a complex morphology, with a bright compact object towards the south, and two weak objects towards the north and northwest. The bright core exhibits a centrally condensed morphology. This is the only object in the sample where the radio source lies more than 1' away from the core peak but still being within the envelope although in the 10% contour. The bright dust core has a total flux density of 10.04 Jy and peak flux density of 3.44 Jy/beam. The map's rms noise is 50 mJy/beam.

The MSX image shows a bright object associated with the sub-mm core. The Spitzer image shows a bright object in the center of the cold dust core. No emission is detected towards the position of the radio peak in each of the three color images.

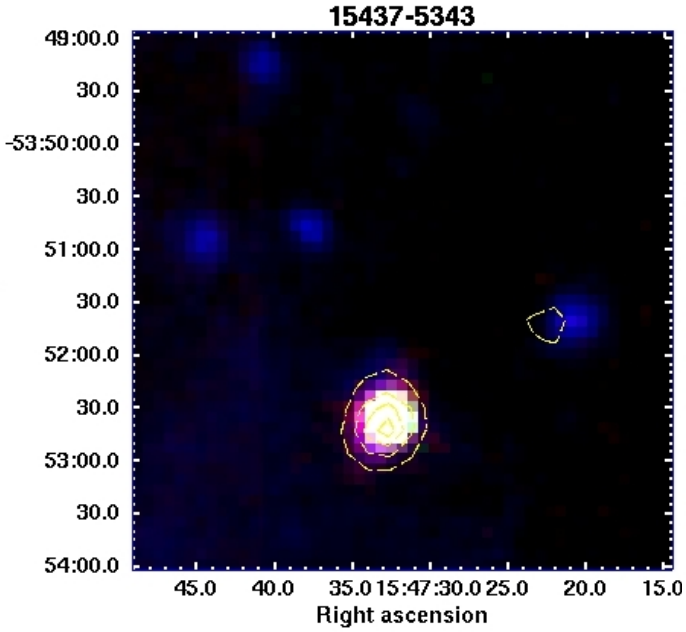

Figure 26b: MSX three color image

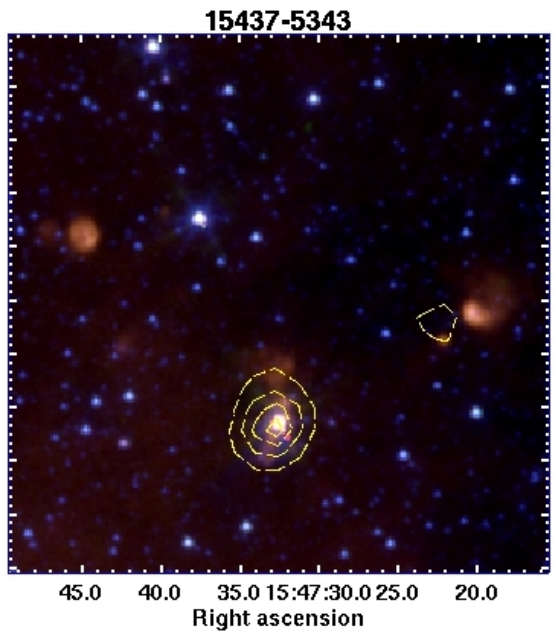

Figure 26c: Spitzer three color image

4.1.26 16547-4247

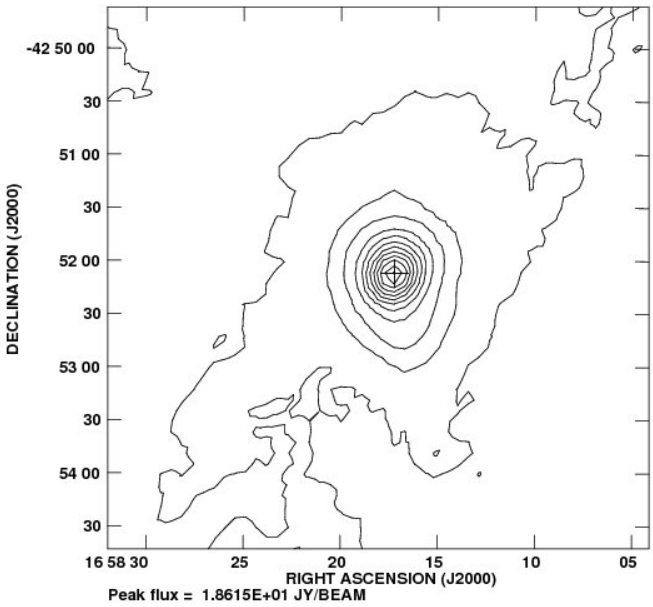

Figure 27a: 870 µm emission, contour levels i

The 870 µm emission towards 16547-4247 arises from a single source with a centrally condensed component and an extended envelope. The central region's total flux density and peak flux density are 58.38 Jy and 18.6 Jy/beam respectively. The map's rms noise is 42 mJy/beam. The radio source lies at the peak of the dust emission.

The MSX image shows the presence of a red, hence highly embedded source. And a 8µm extended emission to the northeast. The Spitzer image shows a couple of compact objects within the cold dust core.

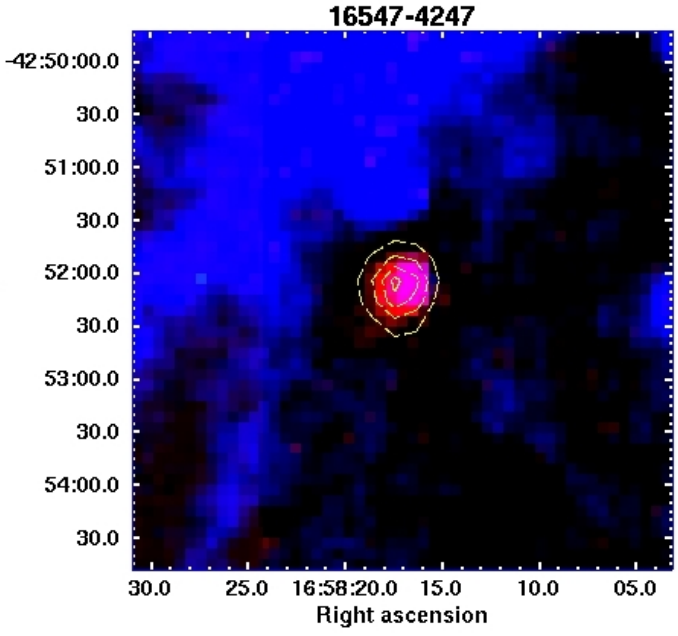

Figure 27b: MSX three color image

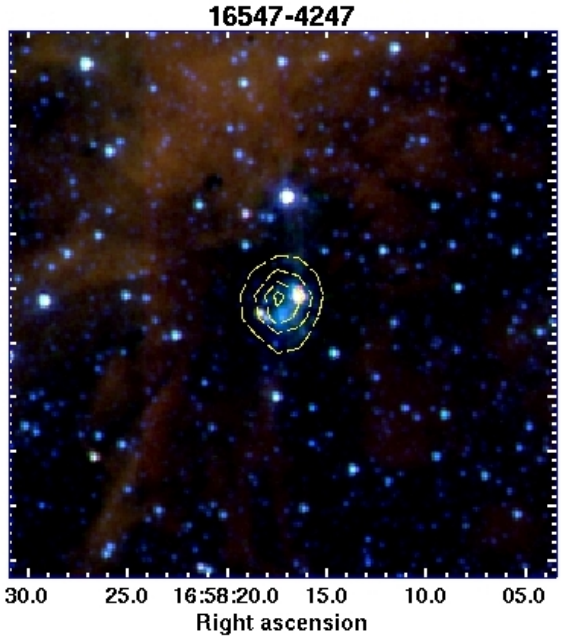

Figure 27c: Spitzer three color image

4.1.27 16561-4006

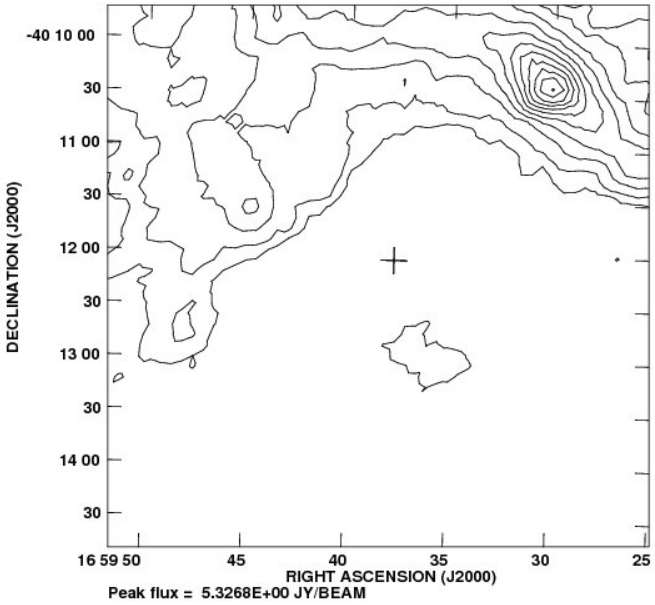

Figure 28: 870 μm emission, contour levels iii

16561-4006 is the only object of our list that is not associated with a 870μm emission. The bright compact dust core located ~2' northwest of the radio source is associated with the IRAS point source. The weak emission to the south is more than 30" away.

4.1.28 17238-3516

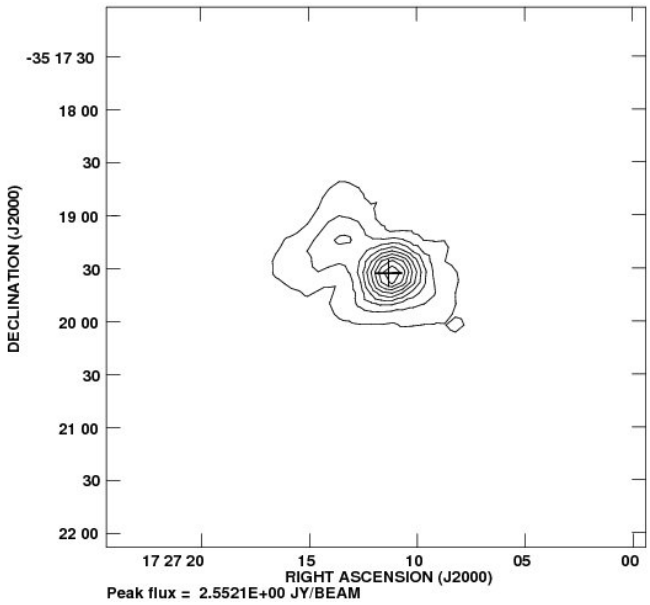

The 870 μm emission towards 17238-3516 arises from two sources, with the brighter one exhibiting a centrally condensed morphology. This region's total flux density and peak flux density are 6.4 Jy and 2.55 Jy/beam respectively. The map's rms noise is 50 mJy/beam. The radio source lies at the peak of the bright core

The MSX image shows a bright object with a peak located in between of two cold cores, and its emission exhibits a cometary morphology with the tail extending to the north. On the other hand the Spitzer image shows the cometary structure in the 8μm range, and at higher frequencies a couple of objects are seen within the cloud.

Figure 29a: 870 μm emission, contour levels iv

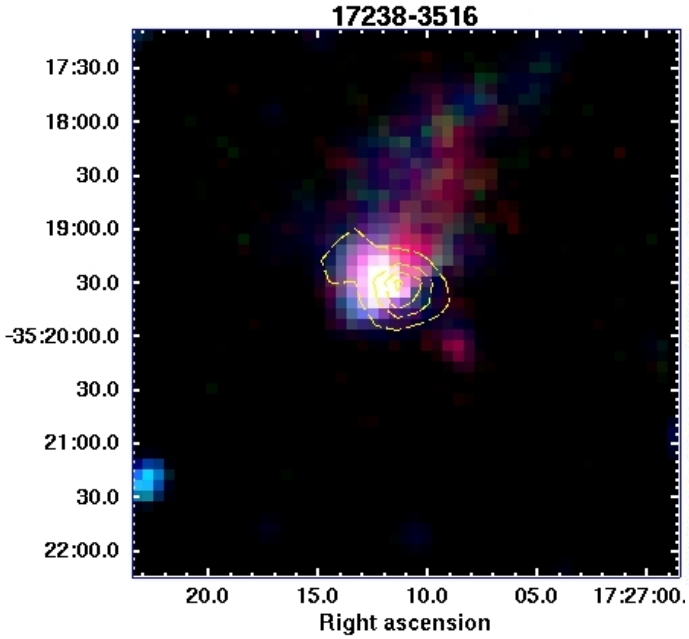

Figure 29b: MSX three color image

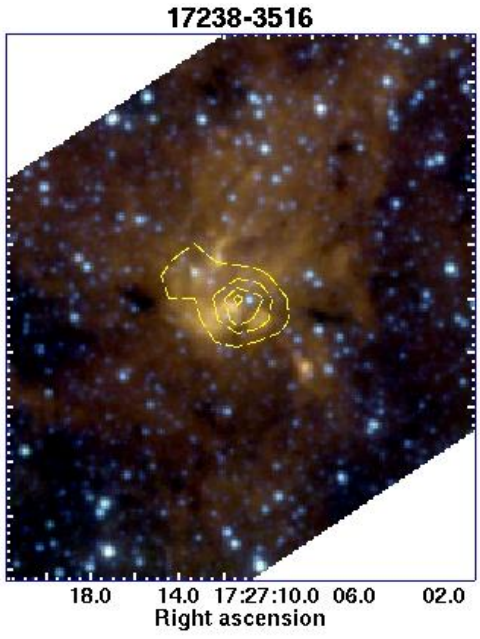

Figure 29c: Spitzer three color image

4.1.29 17439-2845

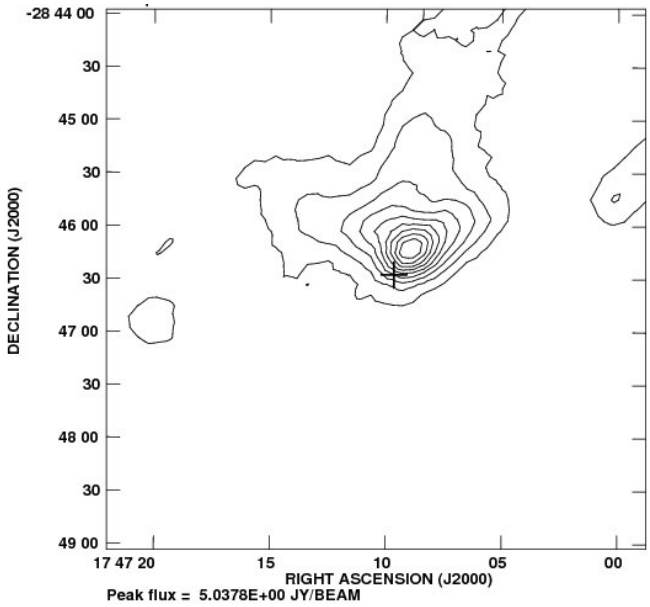

The 870 μm emission towards 17439-2845 exhibits a complex morphology consisting of a bright compact component and two weak filamentary structures extending a couple of arc minutes. The total flux density of the central core region (up to 30 % of peak contour) is 24.68 Jy. The peak flux density is 5 Jy/beam and the map's rms noise is 74 mJy/beam. The radio source lies within 15" of the peak of the bright core.

The MSX image shows the presence of two bright objects at the southwestern edge of the dust emission. The Spitzer image shows two 8 μm dominated objects at two ends of the cold dust core. The radio peak lies in southeast object.

Figure 30a: 870 μm emission, contour levels iv

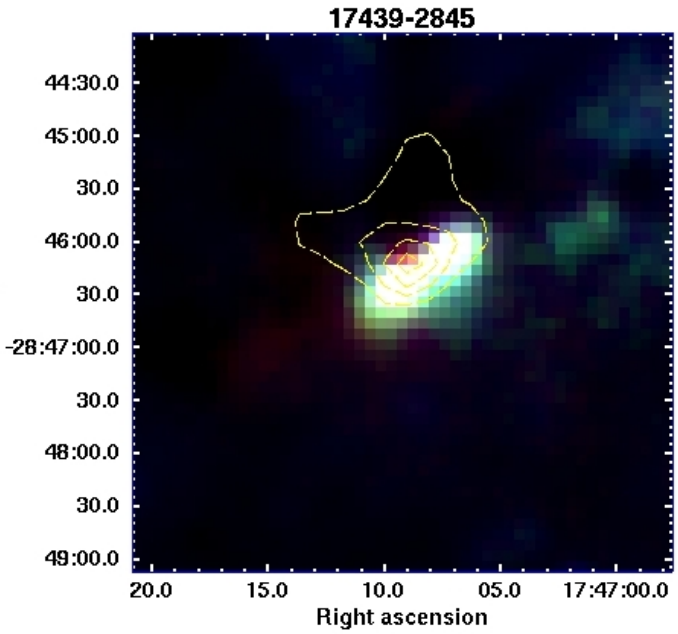

Figure 30b: MSX three color image

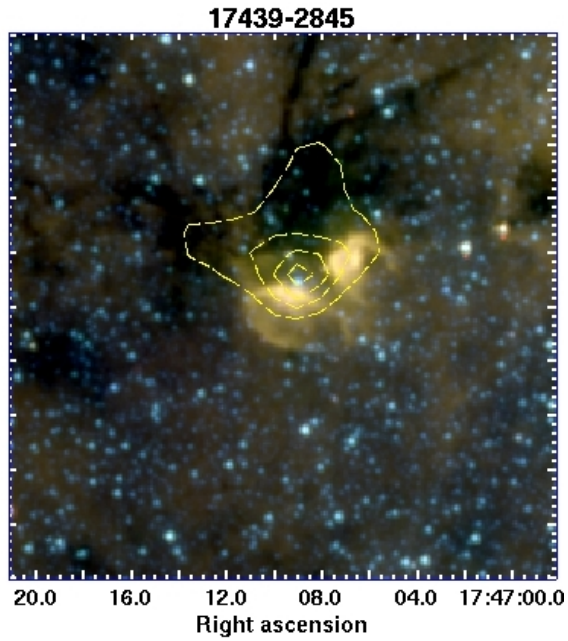

Figure 30c: Spitzer three color image

4.1.30 17559-2420

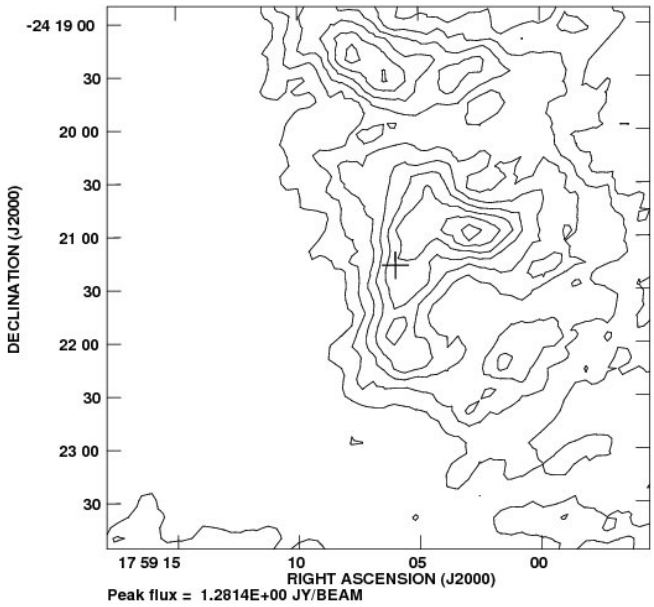

Figure 31: 870 μm emission, contour levels, starting from 3-sigma (150 mJy/beam) and increasing in steps of 3-sigma

The 870 μm emission towards 17559-2420 arises from a weak complex extended structure, with no distinct bright core. There are a few peaks of roughly the same peak flux density. The region's peak flux density is 1.28 Jy/beam and the map's rms noise is 50 mJy/beam. The radio source lies inside the overall dust emission but can't be associated clearly with any peak. The total flux density of the common cloud in which the radio source lies is 17.25 Jy.

The MSX image shows two objects within the 870 μm emission, with the brighter one coinciding with the position of the brighter sub-millimeter peak. The Spitzer image shows a widespread 8 μm emission which encompasses the same area as the sub-mm emission but has a different morphology. No emission is detected towards the radio source in any of the two three color images.

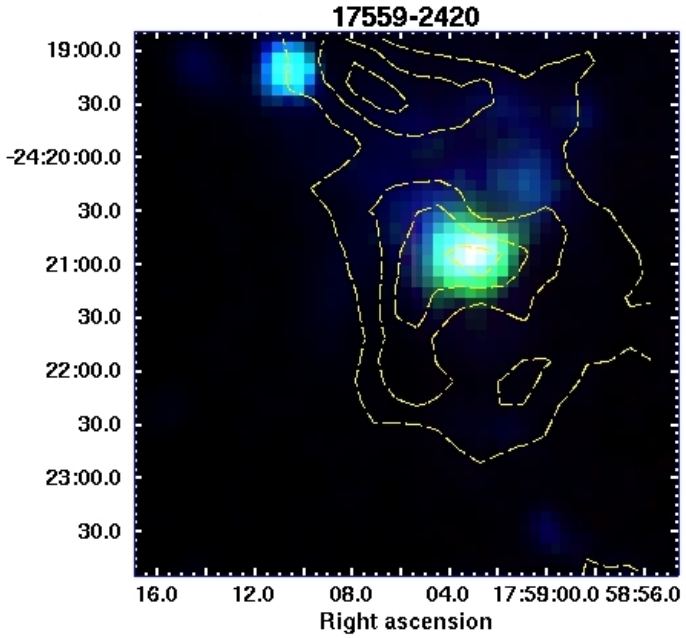

Figure 31b: MSX three color image

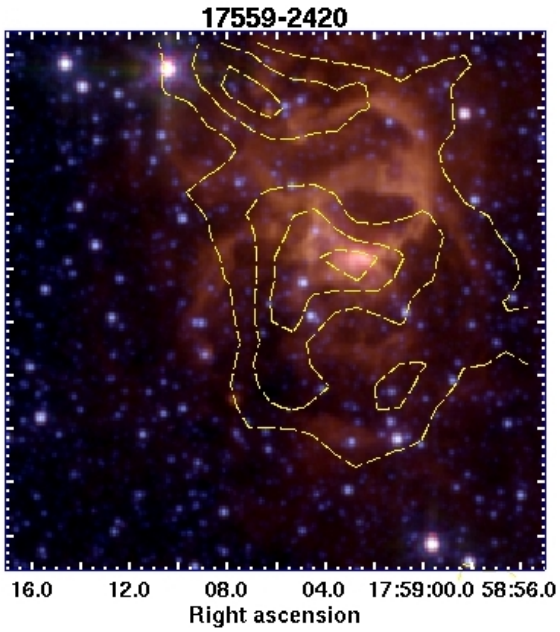

Figure 31c: Spitzer three color image

4.1.31 18048-2019

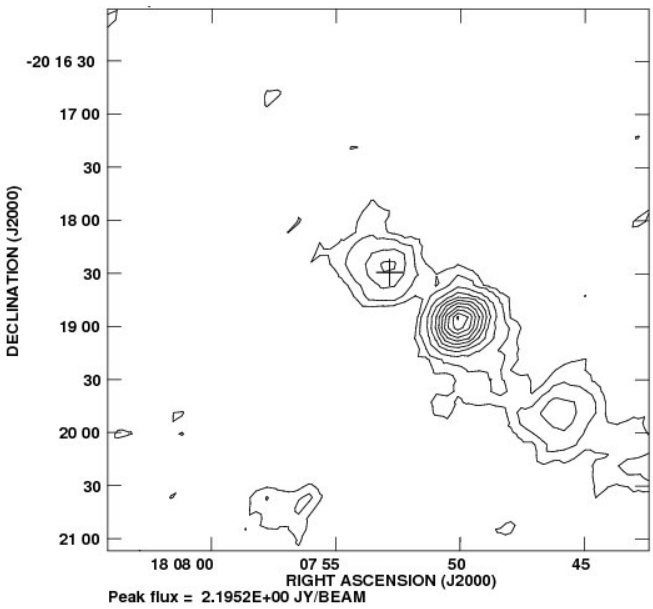

Figure 32a: 870 μm emission, contour levels iii

The 870 μm emission towards 18048-2019 shows the presence of three compact objects lying in a linear structure, with the brightest core being clearly centrally condensed. This is the only object in which the radio source is associated with a core but not the brightest one. The flux density of this weaker core is 1.72 Jy. The whole region's peak flux density is 2.2 Jy/beam and the map's rms noise is 40 mJy/beam respectively.

The MSX image shows a compact object associated with the cold core where the radio source lies. The Spitzer image shows a bright compact object at the location of the radio source and an extended weak 8 μm emission surrounding the core. No emission is seen associated with the brightest sub-mm core in both three color images, indicating it is an IRDC.

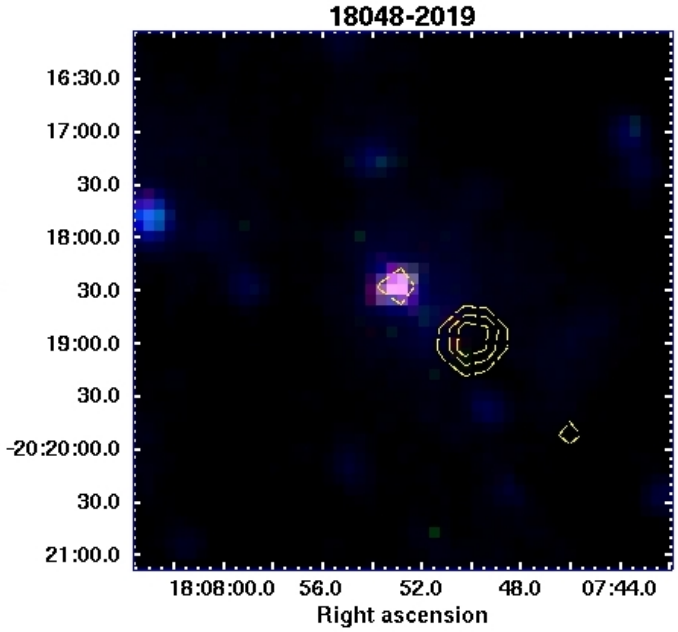

Figure 32b: MSX three color image

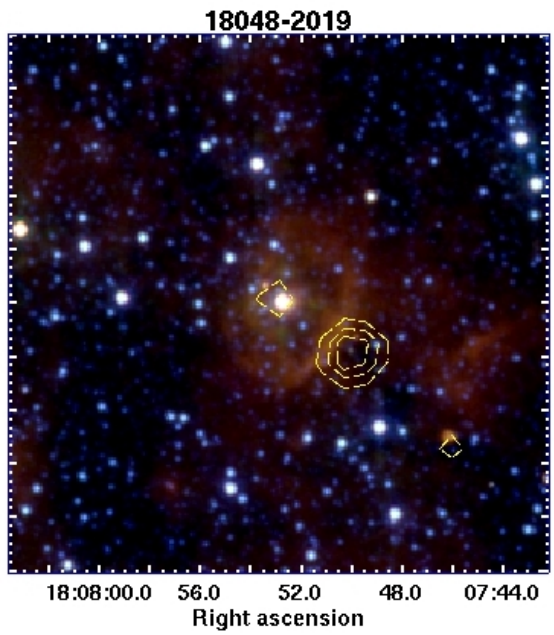

Figure 32c: Spitzer three color image

4.1.32 18064-2020

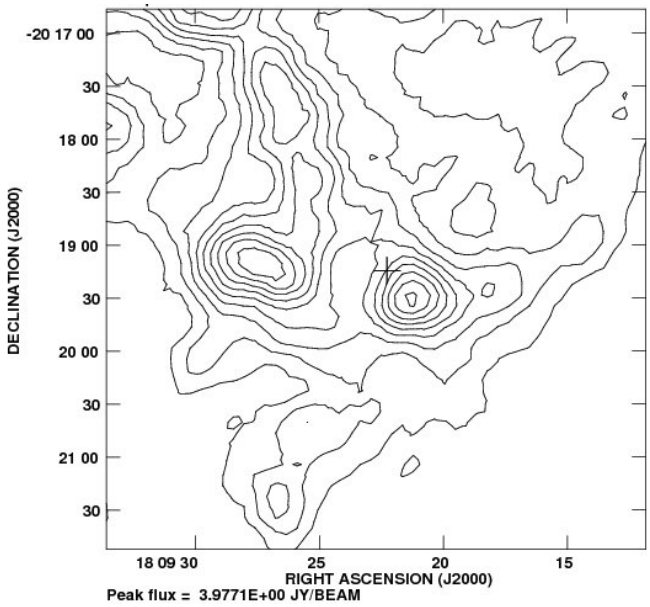

The 870 μm emission towards 18064-2020 arises from a complex region that has several peaks in a common envelope spanning several arc minutes. There are two compact, bright cores with roughly the same peak flux density that dominate the emission, and at least four other peaks. The radio source is located within one of the brightest cores, but not at its peak. The core's (up to 40% of peak contour) flux density is 22.16 Jy. The whole region's peak flux density is 3.98 Jy/beam and the map's rms noise is 57 mJy/beam.

The MSX image shows a bright source associated with the eastern 870 μm bright core. The Spitzer image shows an extended and diffuse 8μm emission. At the position of the radio source there is no distinct features in either of both images.

Figure 33a: 870 μm emission, contour levels iv

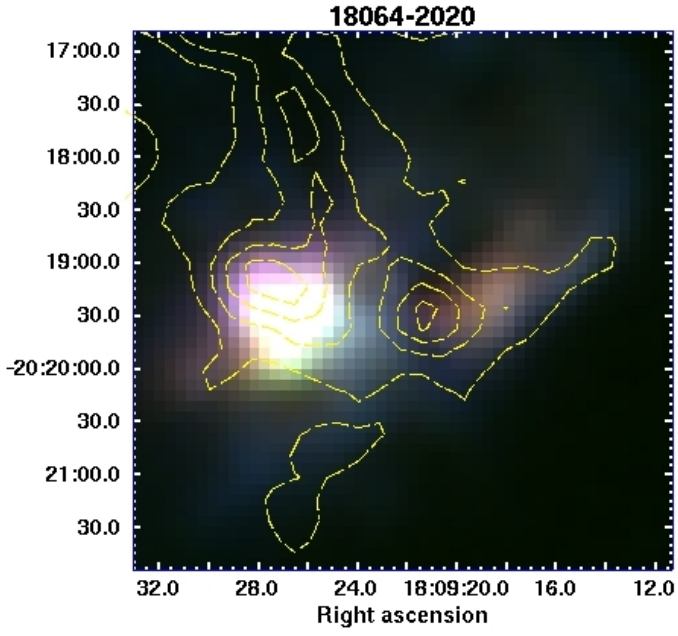

Figure 33b: MSX three color image

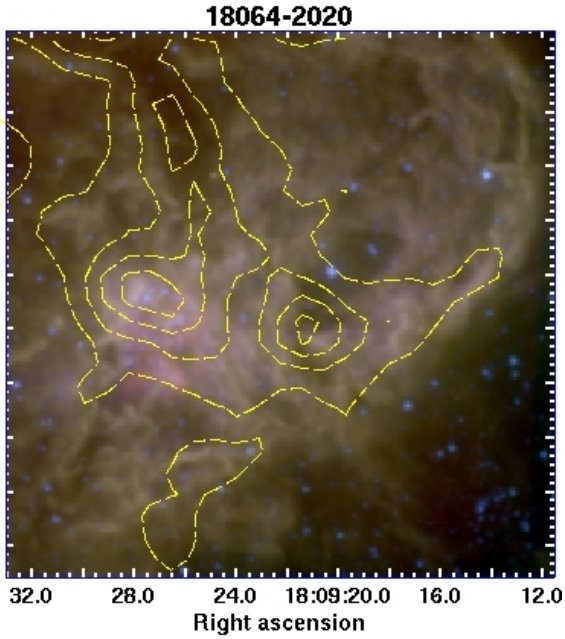

Figure 33c: Spitzer three color image

4.1.33 18314-0720

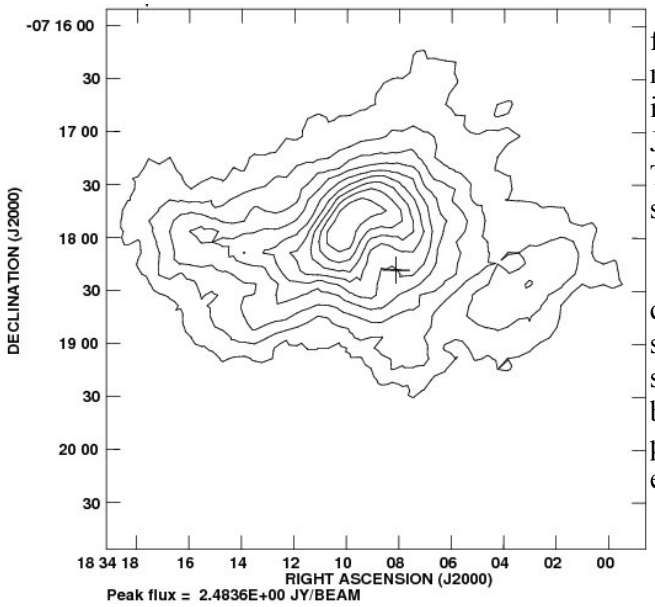

Figure 34a: 870 µm emission, contour levels iv

The 870 µm emission towards 18314-0720 arises from an extended region with an irregular morphology. The total flux density of this dust core is 39.74 Jy. The region's peak flux density is 2.48 Jy/beam and the map's rms noise is 43 mJy/beam. The radio source is located within the dust structure but at ~ 30" from its peak position.

The MSX image shows a bright object in the center of the sub-mm emission. The Spitzer image shows a beautiful morphology, consisting of several bubble-like structures, the brighter one being located at the peak of the dust core. At the position of the radio source there is no distinct emission.

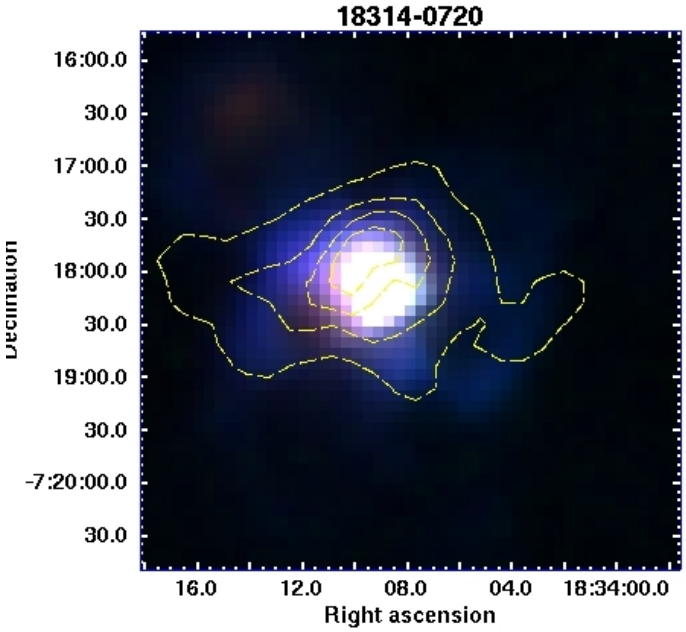

Figure 34b: MSX three color image

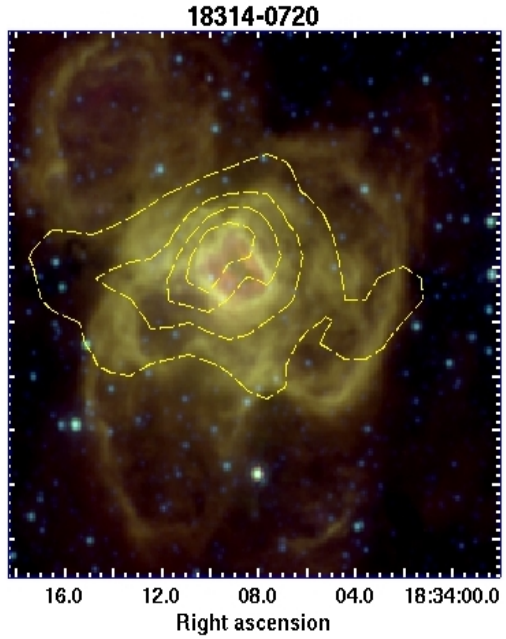

Figure 34c: Spitzer three color image

4.1.34 18316-0602

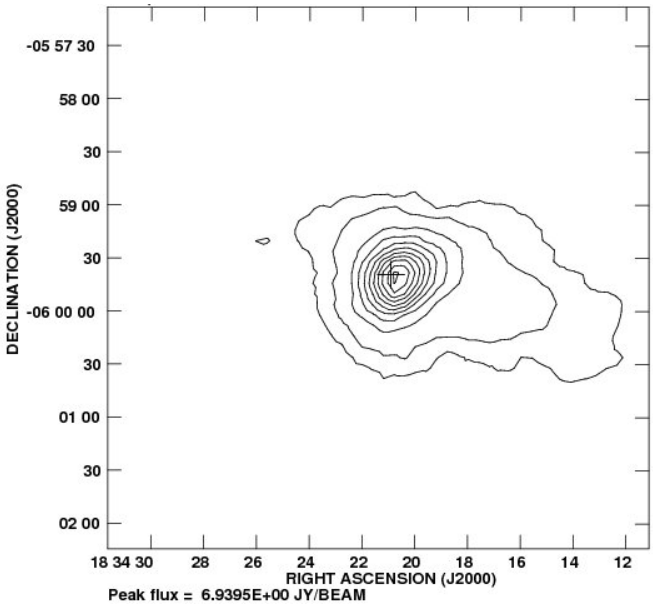

Figure 35a: 870 µm emission, contour levels iii

The 870 µm emission towards 18316-0602 arises from a single region showing a centrally condensed component and an weak envelope extending a couple of arc minutes. The total flux density of the bright component is 30.1 Jy. The central region's peak flux density is 6.9 Jy/beam and the map's rms noise is 63 mJy/beam. The radio source lies at the center of the compact component.

The MSX image shows the presence of a compact red object coinciding with the bright cold dust core. I do not show a Spitzer image due to the lack of data in some bands.

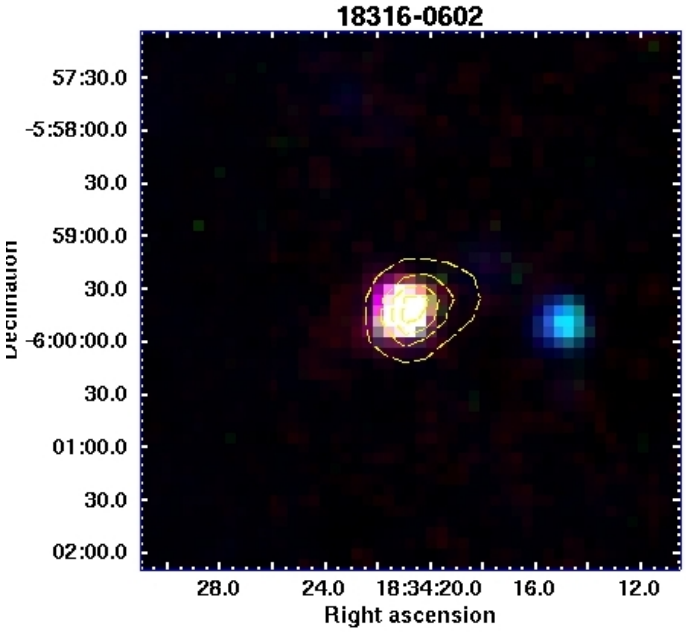

Figure 35b: MSX three color image

4.1.35 G9.62+0.19F

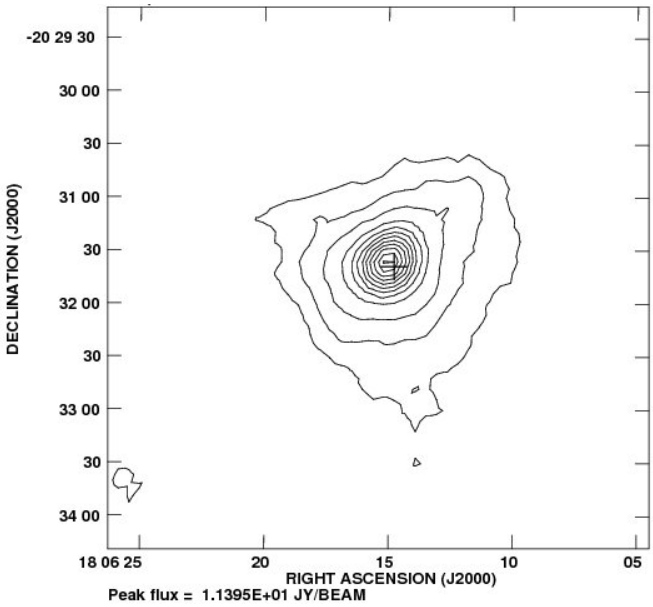

Figure 36a: 870 μm emission, contour levels ii

The 870 μm emission towards G9.62+0.19F arises from a single source with a centrally condensed morphology. The core's total flux density and peak flux density are 34.36 Jy and 11.4 Jy/beam respectively. The map's rms noise is 44 mJy/beam. The radio source lies close to the center of the core.

The MSX image shows a bright structure located to the west of the sub-mm core and a weak, redder component near the center of the core. The Spitzer image shows a clear 8μm extended emission to the west and a couple of compact objects near the cold dust core's center, but no emission to the east.

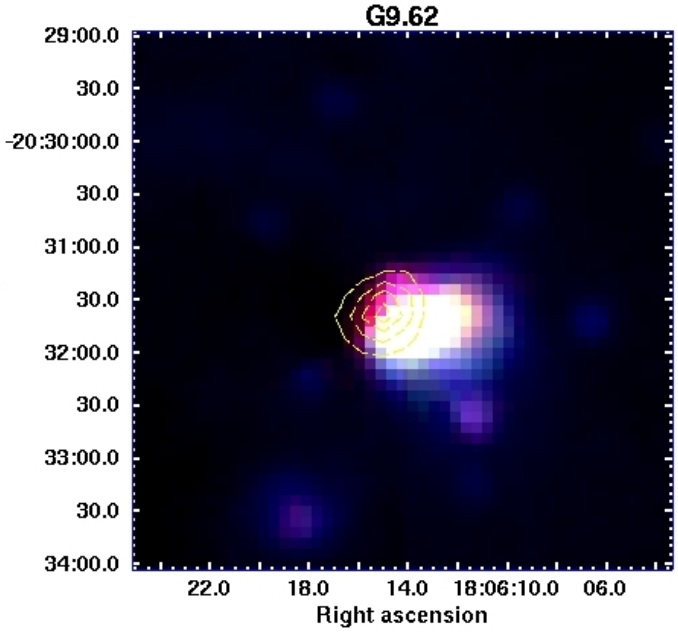

Figure 36b: MSX three color image

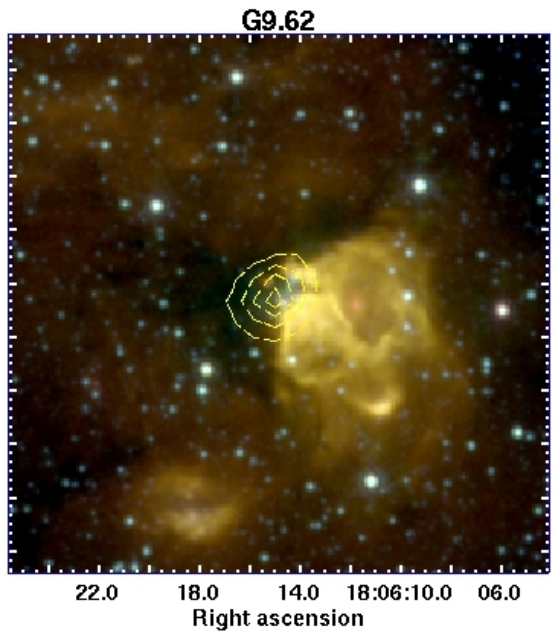

Figure 36c: Spitzer three color image

4.1.36 G10.47+0.03

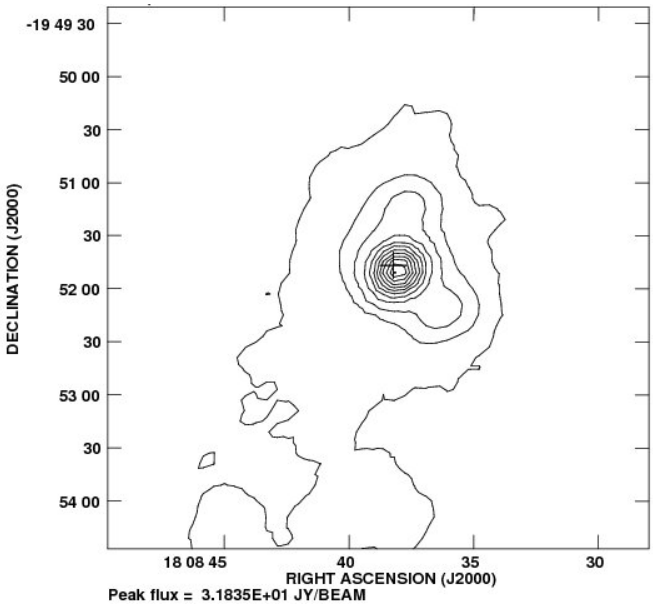

Figure 37a: 870 µm emission, contour levels i

The 870 µm emission towards G10.47+0.03 arises from a single region exhibiting a bright compact core, two weaker cores and an extended envelope. The central region's total flux density is 65.79 Jy. The peak flux density is 31.8 Jy/beam and map's rms noise is 83 mJy/beam. The radio source is located at the position of the bright core.

The MSX image shows three red objects within a common weak extended envelope prominent at 8 µm. The redder of these objects coincides with the bright compact core seen at 870 µm. The Spitzer image shows a cluster of objects viewable in blue, and around it extending to the south a 8 µm diffuse emission.

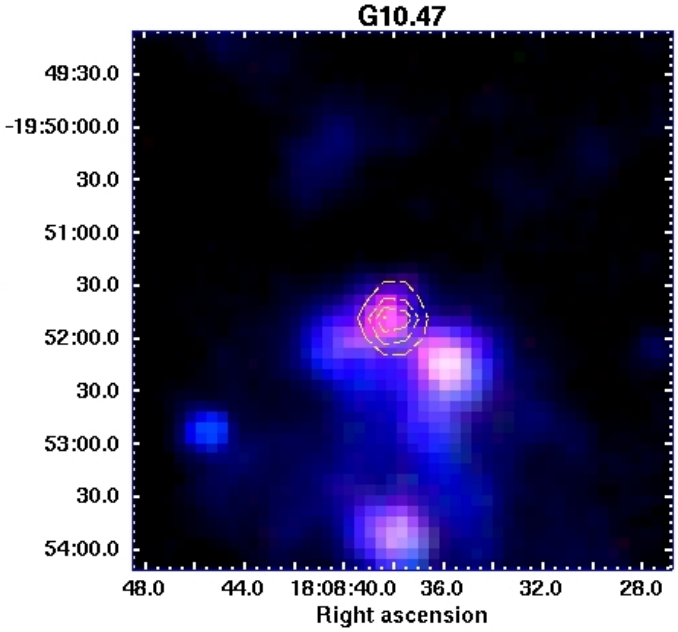

Figure 37b: MSX three color image

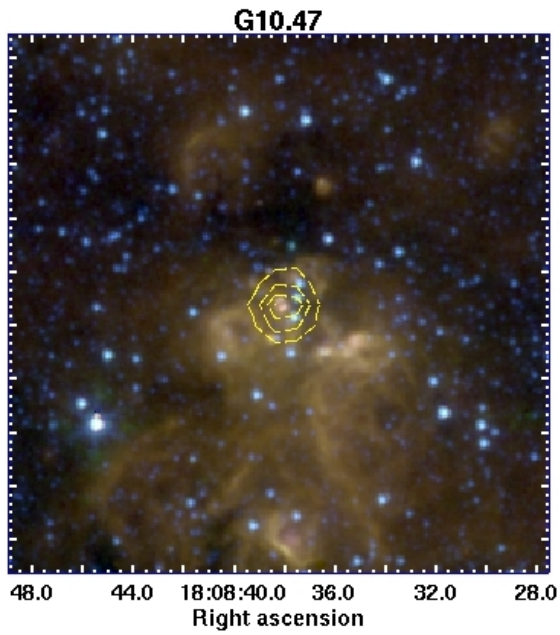

Figure 37c: Spitzer three color image

4.1.37 M17-UC1

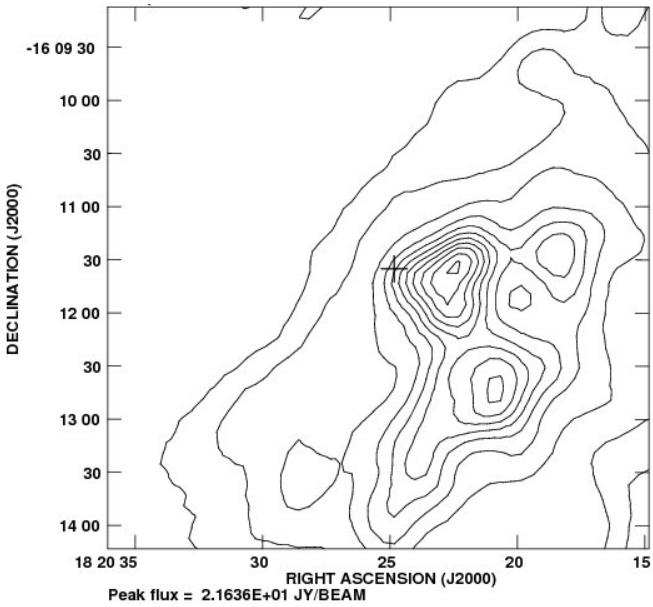

Figure 38a: 870 μm emission, contour levels iii

The 870 μm emission towards M17-UC1 arises from a complex region exhibiting three peaks within a common envelope. The brightest core has 196.03 Jy of flux (square of ~ 80" of side centered at the peak). The region's peak flux density is 21.6 Jy/beam. The map's rms noise is 300 mJy/beam. The radio source is associated with the brightest dust core, but displaced ~ 35" east from its center.

The MSX image shows a bright filament to the northeast of the sub-mm emission and a weaker filament passing through the emission. The Spitzer image also shows these two filaments, and the brightest cold dust core lies between them. The northeast one is dominated by longer wavelengths. On the other hand the southwest one, only appears to have flux from the 8μm and 5.6μm bands. Located in the position of the radio source peak there is a very compact and bright object.

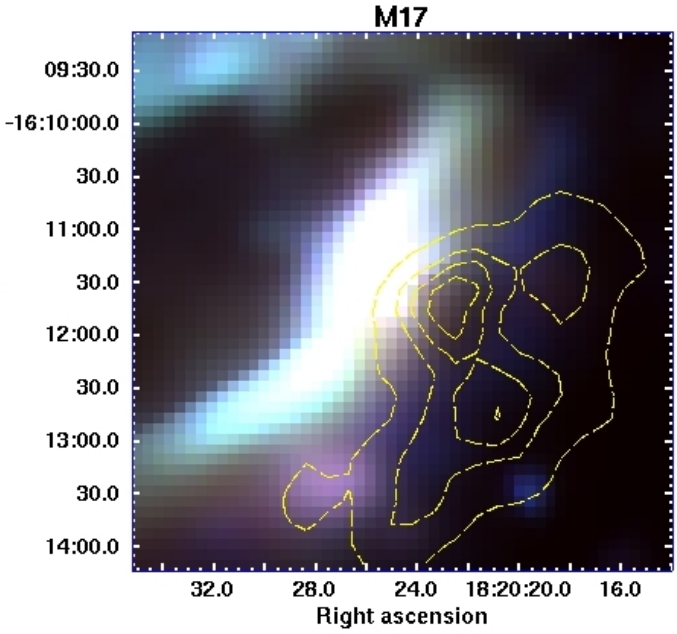

Figure 38b: MSX three color image

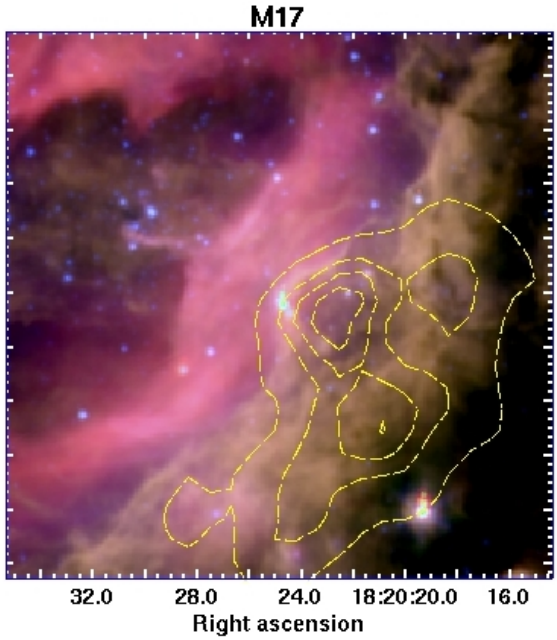

Figure 38c: Spitzer three color image

4.1.38 G20.08-0.14N

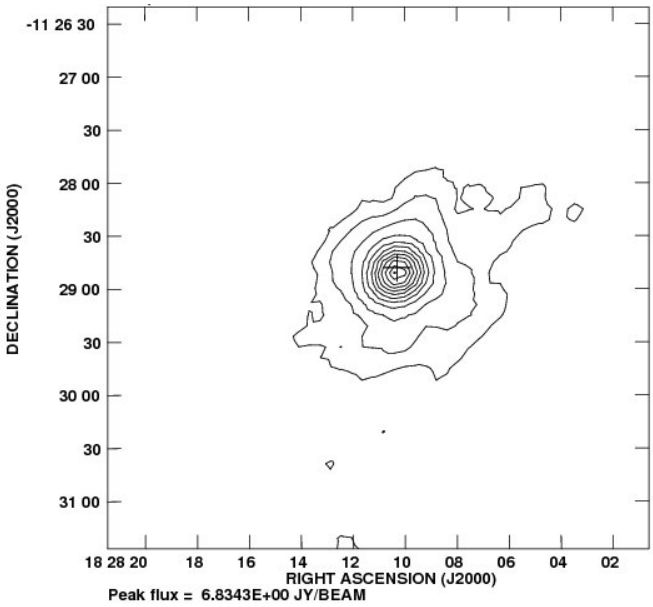

Figure 39a: 870 µm emission, contour levels ii

The 870 µm emission towards G20.08-0.14N arises from a single source with a centrally condensed morphology. The core's total flux density and peak flux density are 17.92 Jy and 6.8 Jy/beam respectively. The map's rms noise 36 mJy/beam. The radio source lies at the peak of the dust emission.

The MSX image shows two sources associated with the cold dust core: a red object located at the peak position of the dust core and a southern bright object. The Spitzer image shows a compact bright object associated with the radio source, and a diffuse 8 µm extending to the south.

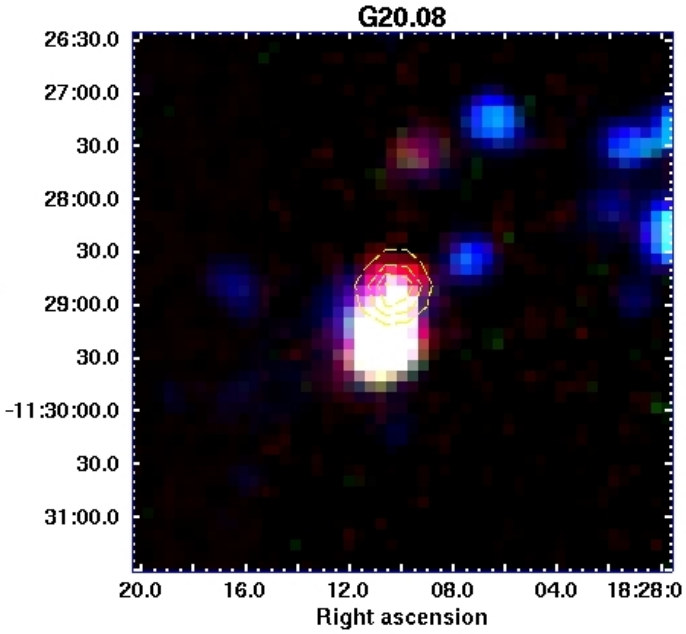

Figure 39b: MSX three color image

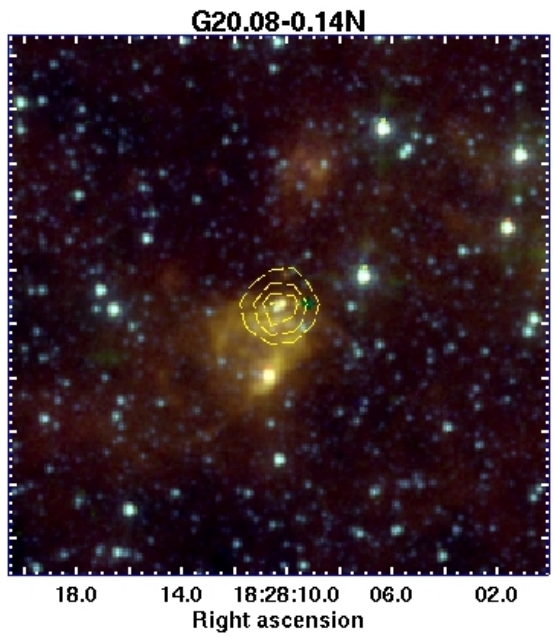

Figure 39c: Spitzer three color image

4.1.39 G24.78+0.08 A1

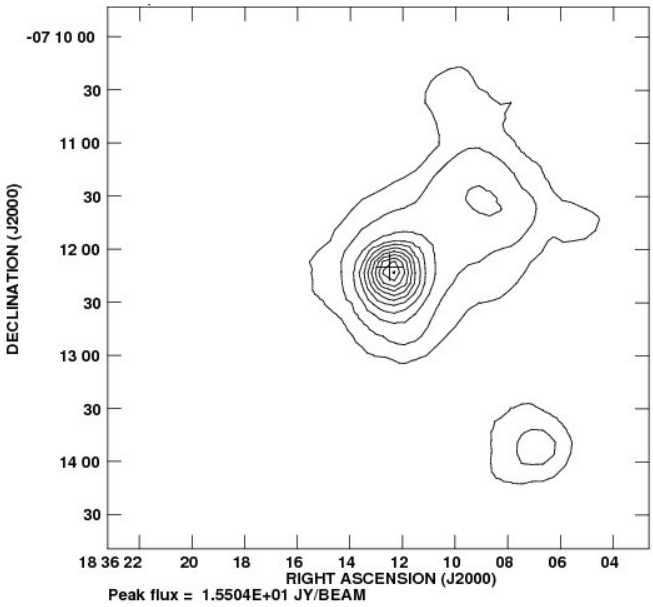

Figure 40a: 870 μm emission, contour levels iii

The 870μm towards G24.78+0.08 A1 emission arises from an elongated structure exhibiting two components. The bright core, in which the radio source lies, shows a centrally condensed morphology. The total flux density and peak flux density of the bright core are 50.48 Jy and 15.5 Jy/beam respectively. The map's rms noise is 160 mJy/beam.

The MSX image shows two filamentary structures right next to each other but prominent at different wavelengths, and each have a bright core in the middle. No emission is detected at the location of the cold core in the MSX image. The Spitzer image only shows one of the filaments as diffuse 8 μm emission. A bright compact object is located in the position of the radio source

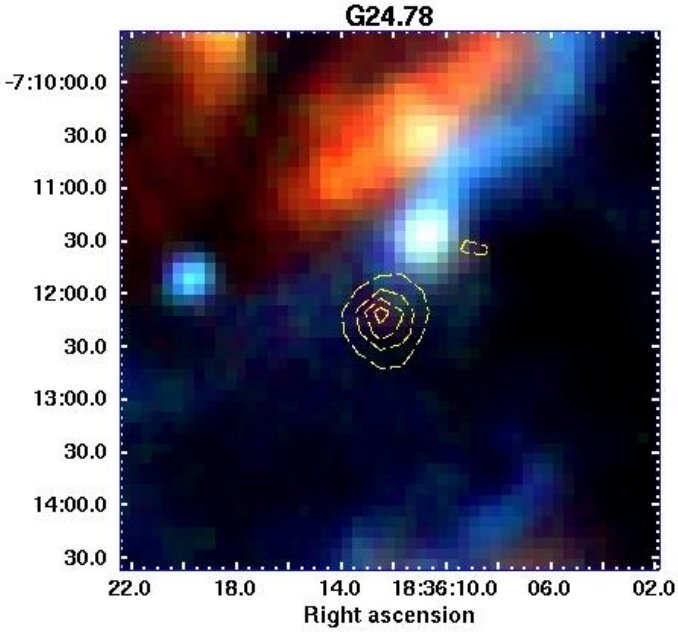

Figure 40b: MSX three color image

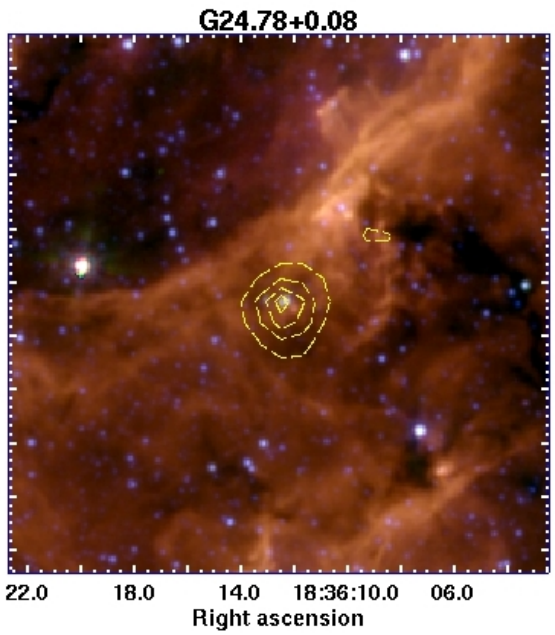

Figure 40c: Spitzer three color image

4.1.40 G28.20-0.04N

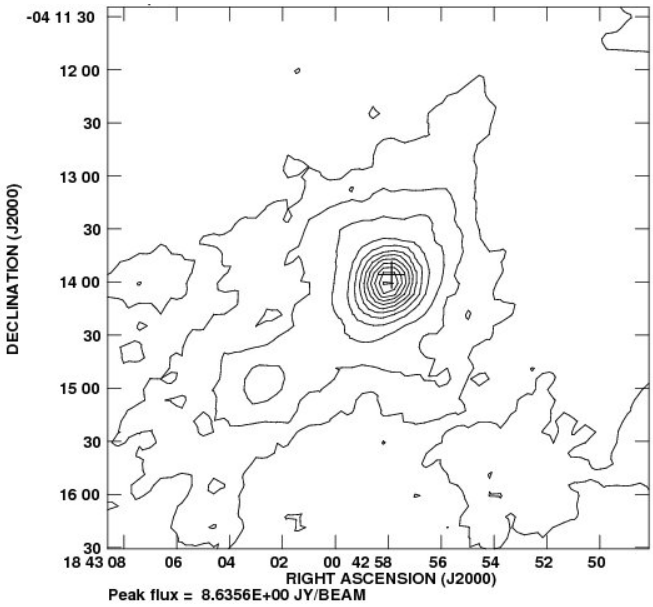

Figure 41a: 870 µm emission, contour levels ii

The 870 µm emission towards G28.20-0.04N arises from an irregular morphology exhibiting a centrally condensed object, and an elongated irregular envelope. The bright core has a total flux density of 25.98 Jy and the radio is within its center. The peak flux density is 8.6 Jy/beam and the map's rms noise is 57 mJy/beam. The radio source lies near the peak of the dust emission.

The MSX image shows a bright core coincident with the cold dust emission. The Spitzer image shows a bright compact object in the center of the sub-mm emission.

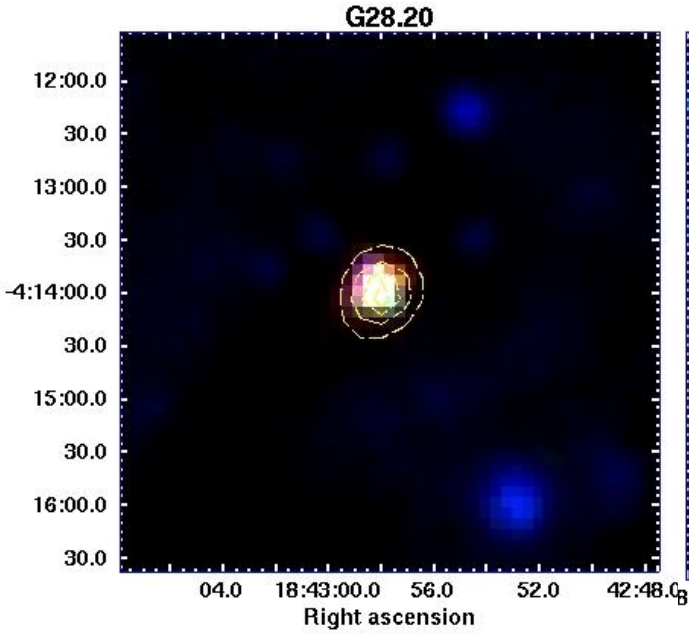

Figure 41b: MSX three color image

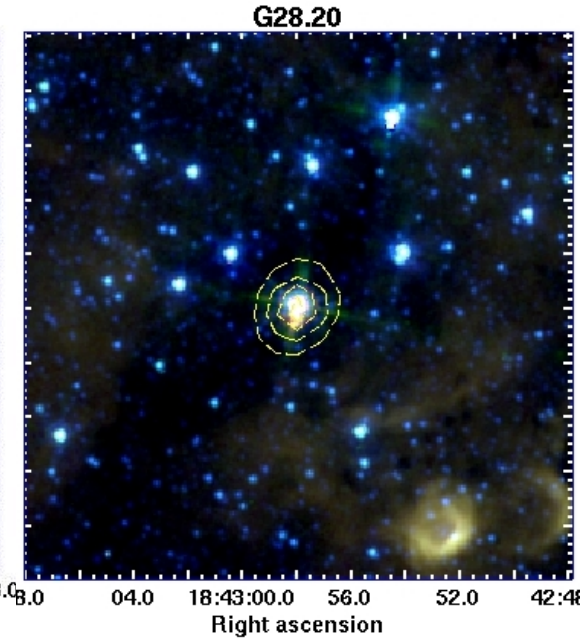

Figure 41c: Spitzer three color image

4.1.41 G34.26+0.15B

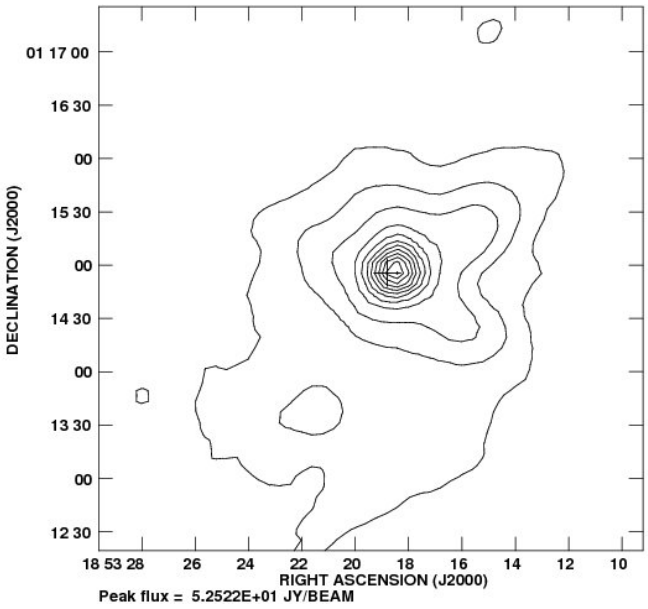

Figure 42a: 870 µm emission, contour levels ii

The 870 µm emission towards G34.26+0.15B arises from a single region with a bright centrally condensed object surrounded by an envelope. The core's (up to 10% of peak contour) total flux density and peak flux density are 145.77 Jy and 52.5 Jy/beam respectively. The map's rms noise is 230 mJy/beam. The radio source lies near the peak of the dust emission.

The MSX image shows a bright object to the southeast of the cold dust core, but no emission is seen in other directions. The Spitzer image clearly shows the complex morphology of the extended 8 µm southeast emission. Also shows the presence of a bright compact source at the position of the radio source.

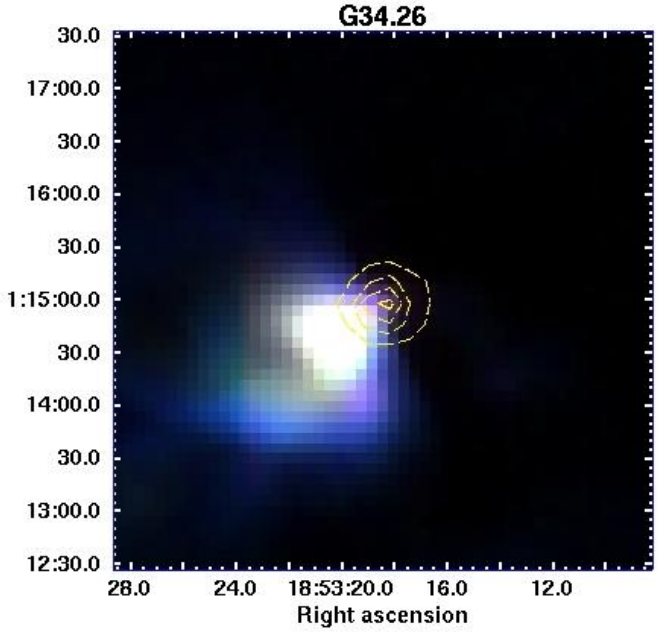

Figure 42b: MSX three color image

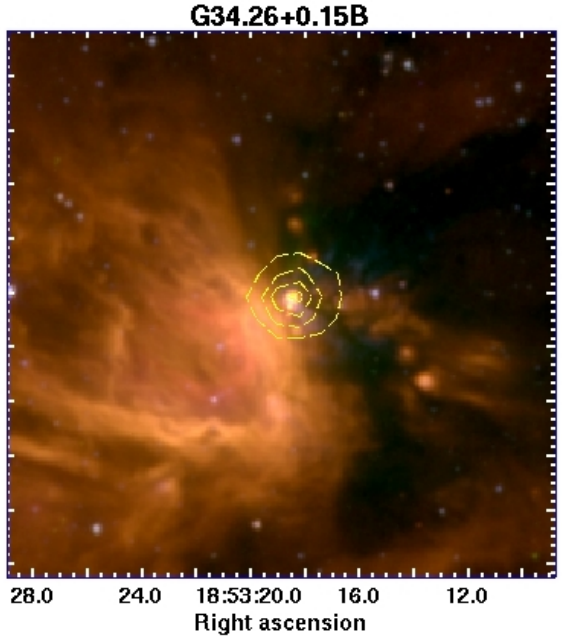

Figure 42c: Spitzer three color image

4.1.42 G12.89

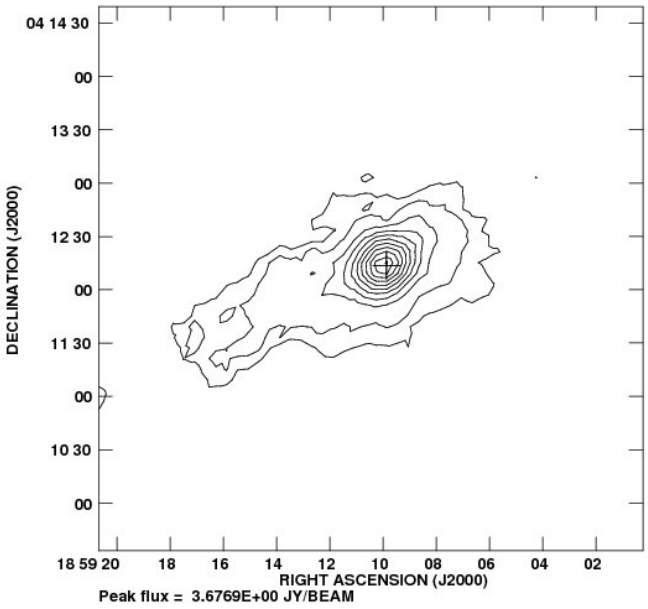

Figure 43a: 870 μm emission, contour levels iii

The 870 μm emission towards G12.89 arises from a single region exhibiting a bright core, within a weak filamentary structure. The dust core's total flux density and peak flux density are 11.07 Jy and 3.7 Jy/beam respectively. The map's rms noise is 60 mJy/beam. The radio source lies at the center of the bright core.

The MSX image shows a bright source coincident with the bright cold dust core. The Spitzer image shows a bright (even saturated) object in the center of the sub-mm emission. No extended 8μm emission is seen.

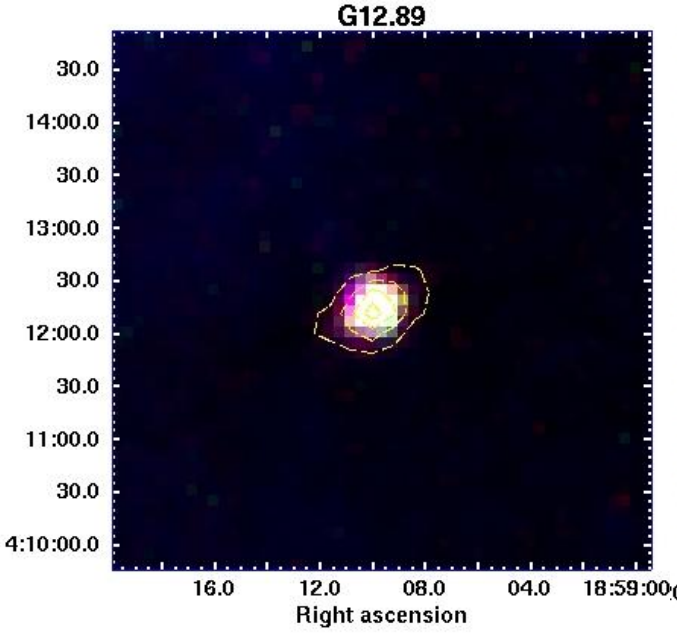

Figure 43b: MSX three color image

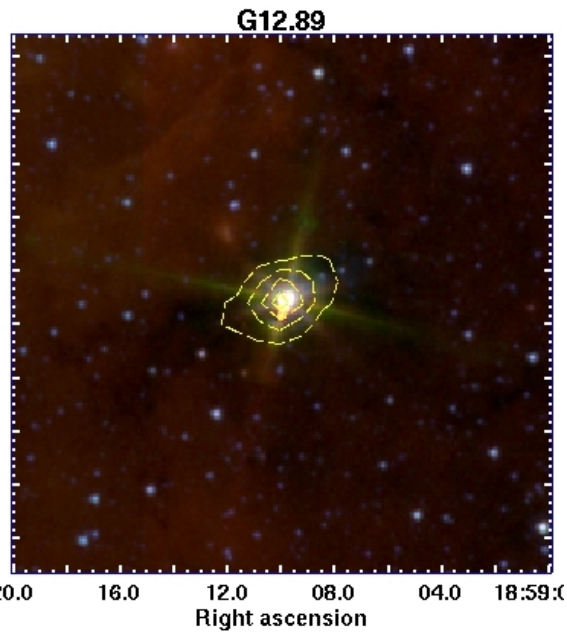

Figure 43c: Spitzer three color image

4.1.43 G43.80-0.13

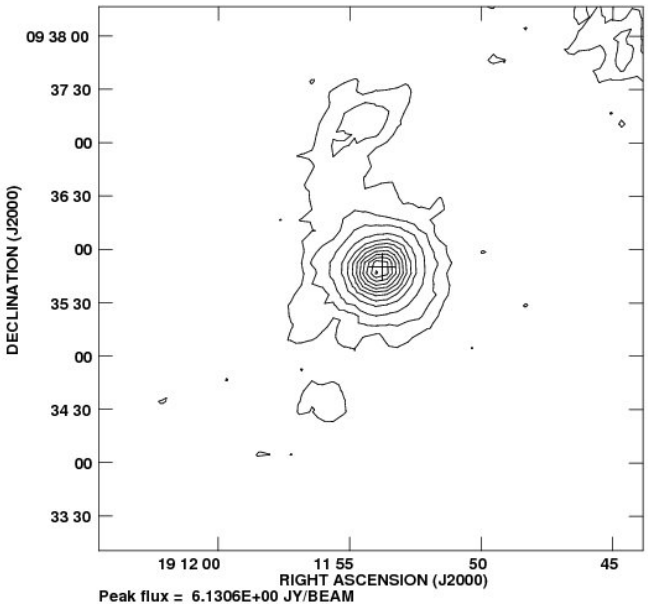

Figure 44a: 870 μm emission, contour levels ii

The 870 μm emission towards G43.80-0.13 arises from a single source with a centrally condensed morphology, within a weak filamentary envelope. The total flux density and peak flux density are 14.41 Jy and 6.1 Jy/beam respectively. The map's rms noise is 42 mJy/beam. The radio source lies near the center of the core.

The MSX image shows a bright object associated with the cold dust emission, with a 8 μm tail extending to the west. The Spitzer image shows a couple of bright compact objects within the sub-mm core.

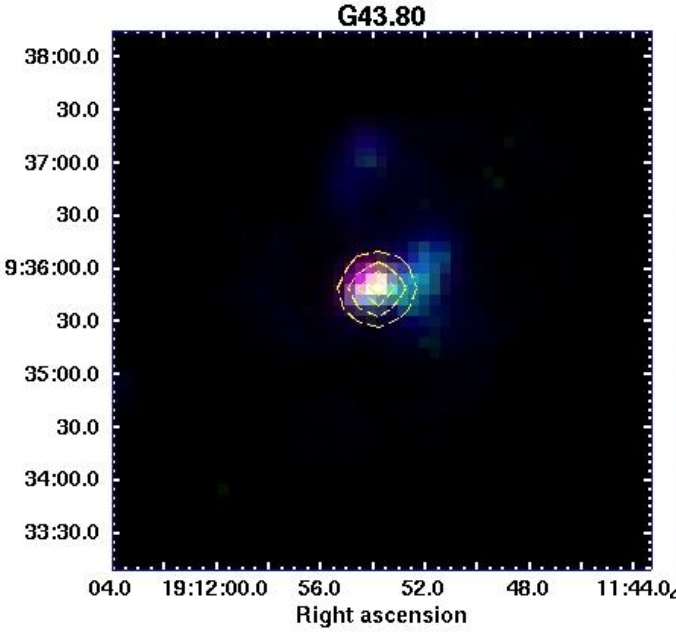

Figure 44b: MSX three color image

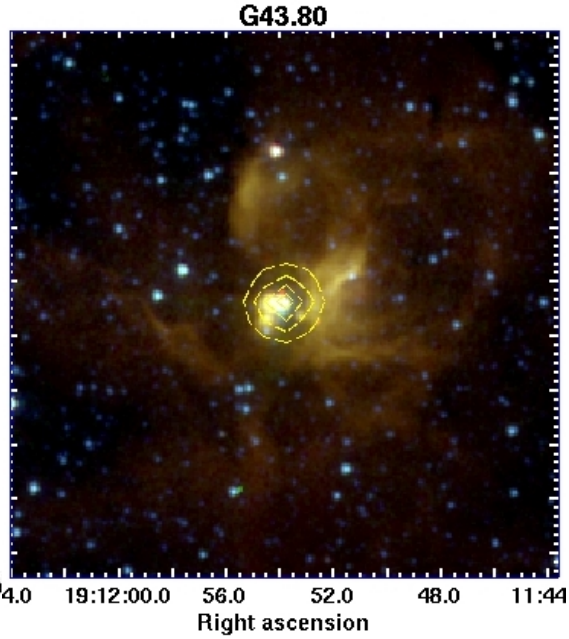

Figure 44c: Spitzer three color image

4.1.44 G45.07+0.13

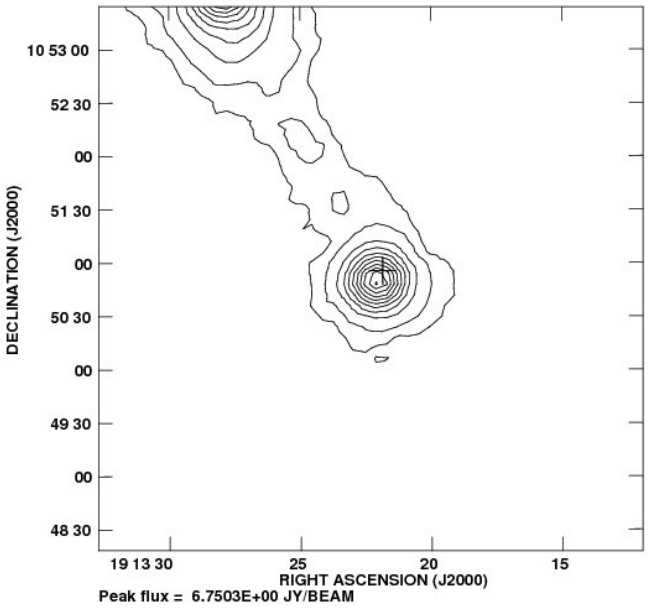

Figure 45a: 870 µm emission, contour levels iii

The 870 µm emission towards G45.07+0.13 shows a bright compact core located at the end of a filamentary structure which also harbors another core of roughly the same flux. The dust core's total flux density and peak flux density are 18.05 Jy and 6.75 Jy/beam respectively. The map's rms noise is 53 mJy/beam. The radio source lies near the center of the central bright core.

The MSX image shows a red object associated with the bright central dust core. The Spitzer image shows a very bright (saturated) object at the center of the cold dust core, and a weak diffuse 8 µm emission extending several arc minutes. The connecting filament is not seen in neither of the three color images.

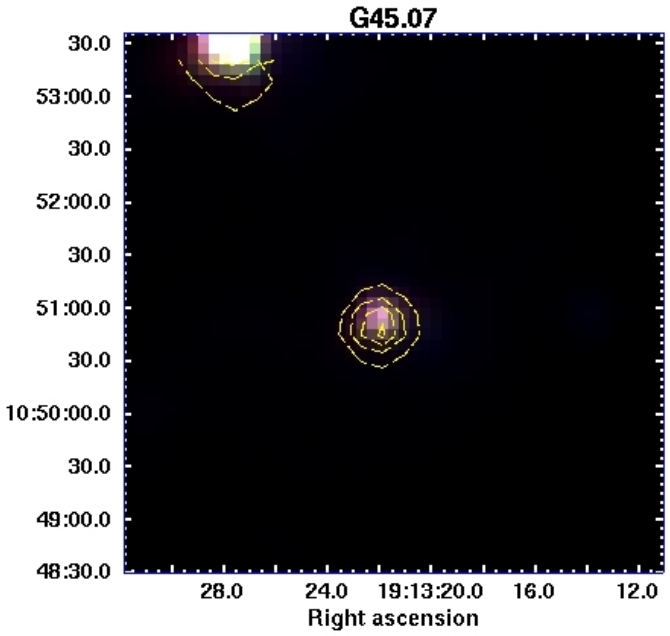

Figure 45b: MSX three color image

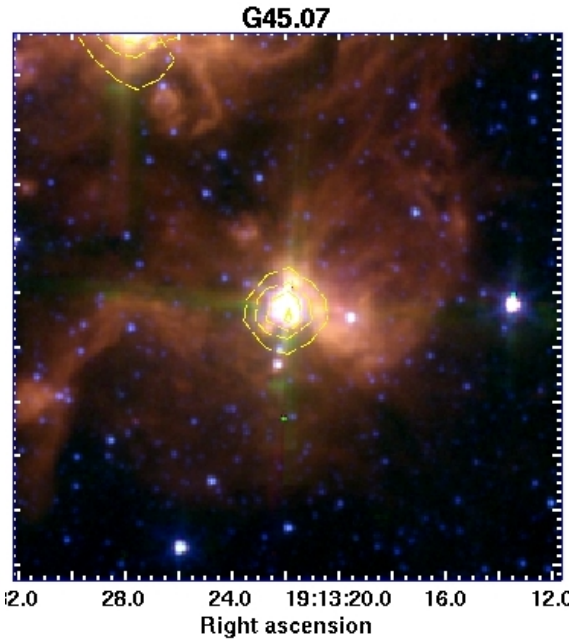

Figure 45c: Spitzer three color image

4.2 Overall Results

Of the 44 radio objects (from both lists) within the ATLASGAL coverage only one, 16561-4006, had no counterpart at 870 μm; all the others had at least a compact component as a counterpart. So 33 of the 34 sources of the Guzman sample that are within the coverage had a counterpart, which gives a 97% efficiency for the selection criteria to have a 870 μm emission visible by ATLASGAL.

The morphology of the cold dust counterparts consisted in most of the cases of a centrally condensed compact object, within either a filamentary structure, a spherical weak envelope or an irregular structure. Table 4 shows the morphology distribution. Column 2 shows the number of objects for the Guzman list, column 3 for the HCHII, column 4 for the total, and column 5 the percentage of the total that they represent. The most typical configuration is a bright compact central component plus a weaker extended emission.

To analyze the correlation between the position of the radio and sub-millimeter emission, I use the ratio of the linear distance between the radio source and the sub-millimeter peak (distlin) to the radius of the cold dust core. This ratio is shown in Table 5 and to illustrate the distribution I show a histogram on Figure 46. In 37 cases (86%) the ratio is less than 1.0 which shows that there is a high correlation between the emissions at the two different wavelengths, and in 28 cases (65%) the ratio is less than 0.5. This result indicates that the jet candidates are located at the center of the massive cores and most likely they are being formed there.

Table 4: Morphology

Morphology	Guzman List	HCHII	Total	Percentage
Compact	4	0	4	9%
C + Extended	18	6	24	56%
C + Filament	8	3	11	26%
Irregular	3	1	4	9%

Table 5: Linear distance between the radio source and the peak of the dust core (distlin) over radius

Distlin/radius	Guzman Sample	HCHII	Total
0.0-0.5	28	20	8
0.5-1.0	9	8	1
1.0-1.5	3	2	1
1.5-2.0	2	2	0
>2.0	1	1	0

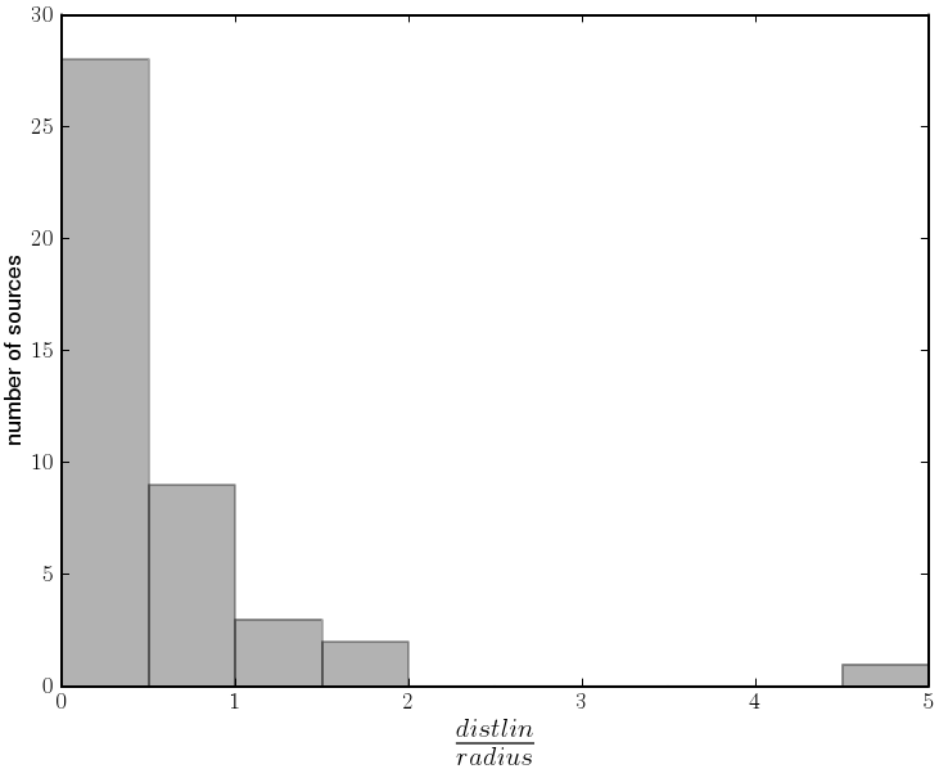

Figure 46: Linear distance between the radio source and the peak of the dust core (distlin) over radius, for the whole sample

Chapter 5

Spectral Energy Distributions

To derive physical parameters, such as column density and temperature, I fit the observed spectral energy distribution (SED) to a model. This is done in two steps as an iterative process: In the first step I use a simplified form of the model to obtain the temperature of a cold component and its column density, and in the second step I use those values in the full form of the model to obtain more information.

I followed the model used by Morales et al. (2009) that assumes the presence 3 spherical symmetric components: an extended cold component (c), an inner warm component (w) and a compact hot component (h). Each one is a gray blackbody and I include the radiation absorption by the enclosing envelopes. The total flux density, F_ν , is given by;

$$F_\nu = F_\nu^c + F_\nu^w + F_\nu^h \quad , \tag{5}$$

where,

$$F_\nu^h = \Omega_h B_\nu(T_h)(1-\mathrm{e}^{-\tau_\nu^h})\mathrm{e}^{(-\tau_\nu^c-\tau_\nu^w)/2} \quad , \tag{6}$$

$$F_\nu^w = \Omega_w B_\nu(T_w)(1-\mathrm{e}^{-\tau_\nu^w})\mathrm{e}^{-\tau_\nu^c/2} \quad , \tag{7}$$

$$F_\nu^c = \Omega_c B_\nu(T_c)(1-\mathrm{e}^{-\tau_\nu^c}) \quad , \tag{8}$$

and B_ν the Planck function, Ω the solid angle, T the temperature, and τ_ν the optical depth. The subscripts c, w and h denote the values for the cold, warm or hot components respectively.

5.1 SED Fit: First Step

In the first iteration I only use the ATLASGAL flux and the 4 IRAS fluxes, fitting the data with only two modified blackbody components F_ν^c and F_ν^w . This first step, of only using the longer wavelength data obtained with low angular resolution, is used to determine the parameters of the cold envelope of gas since it is in this spectral range and at the large spatial scales that the cold dust emits. The flux density, F_ν, is then given by,

$$F_\nu = F_\nu^c + F_\nu^w \quad , \tag{9}$$

$$F_{\nu}^{c,w} = \Omega_{c,w} B_{\nu}(T_{c,w})\{1-\exp(-\tau_{\nu}^{c,w})\} \quad , \tag{10}$$

In this step I assume that the optical depth depends with the frequency as,

$$\tau_{\nu}^{c,w} = \left(\frac{\nu}{\nu_0^{c,w}}\right)^{\beta_{c,w}} \quad , \tag{11}$$

where β is the power law index, and ν_0 which I refer as the turnover frequency is where optical depth is unity.

For the cold component I used the angular size obtained from the Gaussian fit to the data, and I fixed the power law index, β_w, of the warmer component to 1. With this I had 5 data points and 6 variables, which gives a family of solutions depending on one parameter. In this case I used the size of the warmer component Ω_w as the dependent parameter for each solution because the only assumption for its value is that it was smaller than Ω_c. I iterated for different values of Ω_w ranging from 16 to 2500 times smaller of Ω_c (radius 4 to 50 times smaller). For each iteration the final chi-square was retained and the iteration with the lower value was the one used.

To fit I used a least square method to approximate the solution. This method minimizes the sum of the squares of the errors made in solving each equation, see Appendix A. As starting values the mean values obtained by Faundez et al (2004) using the same method were used. The results are given in Tables (6) and (7), for the two lists lists of objects, respectively.

Table 6: SED parameters from first list, Guzman list

Object	T_c [°K]	$\nu_{0,c}$ [THz]	β	τ_{870} model	T_w [°K]	$\nu_{0,w}$ [THz]	θ_w ["]	τ_{870} obs
G300.9674+01.1499	37.54	4.67	1.75	1.05E-02	143.16	1608.9	7.29	1.04E-02
G301.1364-00.2249	46.29	3.35	1.37	4.45E-02	99.98	142.5	4.32	4.46E-02
G302.1515-00.9488	32.67	20	1.53	2.01E-03	127.4	27.88	0.53	2.23E-03
G308.9176+00.1231	36.79	7.88	1.75	4.19E-03	171.87	47.1	1.24	4.28E-03
G311.1359-00.2372	30.98	27.43	1.6	9.11E-04	130.39	234.27	0.88	9.22E-04
G317.4298-00.5612	37.76	12.43	1.51	4.46E-03	142.81	2745.73	5.29	4.47E-03
G317.8908-00.0578	35.61	41.82	1.27	2.26E-03	133.25	741.94	1.73	2.24E-03
G326.5297-00.4186	41.52	2.36	3.35	1.60E-03	121.34	20.55	0.67	1.85E-03
G326.7249+00.6159	35.93	1.07	3.78	1.37E-02	123.77	43.14	3.2	1.41E-02
G329.4761+00.8414	32.27	9.95	1.7	3.30E-03	131.16	41.36	0.75	3.28E-03
G330.2935-00.3946	35.75	4.9	1.64	1.29E-02	125.73	22.55	1.05	1.28E-02
G332.8256-00.5498	43.76	1.63	1.87	5.50E-02	114.69	71.89	5.44	5.57E-02
G333.0162+00.7615	31.26	7.15	1.46	1.20E-02	122.51	115.08	1.69	1.18E-02
G333.1306-00.4275	37.33	2.4	1.84	2.82E-02	126.94	15.1	2.31	2.84E-02

Object	T_c [°K]	$\nu_{0,c}$ [THz]	β	τ_{870} model	T_w [°K]	$\nu_{0,w}$ [THz]	θ_w ["]	τ_{870} obs
G336.9842-00.1835	39.54	8.23	1.8	3.32E-03	152.57	45.27	0.57	3.30E-03
G337.4032-00.4037	37.55	2.14	1.75	4.09E-02	117.22	16.5	0.84	4.12E-02
G337.7051-00.0575	31.36	0.98	3	4.34E-02	132.25	842.1	2.28	4.33E-02
G337.7091+00.0932	31.32	2.73	1.81	2.37E-02	142.8	89.5	0.64	2.36E-02
G337.8442-00.3748	34.81	7.35	1.61	7.27E-03	155.6	43.53	1.06	7.33E-03
G338.9217+00.6233	31.82	3.5	1.95	1.09E-02	125.36	1588.37	8.06	1.09E-02
G340.2480-00.3725	32.15	15.14	1.3	7.33E-03	111.08	801.01	5.12	7.42E-03
G345.4938+01.4677	38.79	6.29	1.27	2.51E-02	119.93	173.59	5.03	2.54E-02
13134-6242	37.94	4.38	1.32	3.49E-02	120.54	47.98	0.92	3.46E-02
13471-6120	41.92	7.71	1.4	1.29E-02	142.2	4.9	0.92	1.32E-02
15437-5343	37.72	14.46	1.35	6.46E-03	118.61	46.48	0.92	6.59E-03
16547-4247	35.39	2.57	1.55	4.45E-02	106.37	27.16	0.89	4.47E-02
17238-3516	30.2	2.14	2.74	6.72E-03	128.25	46.15	0.5	6.70E-03
17439-2845	29.61	2.97	2.21	8.60E-03	124.62	163.8	2.94	8.58E-03
17559-2420	30.92	30.67	1.54	9.97E-04	125.8	129.19	2.12	9.80E-04
18048-2019	28.13	4.74	2.34	2.17E-03	146.04	1415.77	1.2	2.17E-03
18064-2020	33.76	2.08	3.02	4.42E-03	144.2	10.38	2.08	4.67E-03
18314-0720	33.29	10.79	1.68	3.08E-03	145.27	195.12	3.44	3.11E-03
18316-0602	32.85	10.92	1.23	1.43E-02	134.79	73.49	1.17	1.44E-02

Table 7: SED parameters from first fit, HCHII regions

Object	T_c [°K]	$\nu_{0,c}$ [THz]	β	τ_{870} model	T_w [°K]	$\nu_{0,w}$ [THz]	θ_w ["]	τ_{870} obs
G9.62+0.19F	38.04	2.85	1.75	2.48E-02	136.25	15.74	0.87	2.47E-02
G10.47+0.03	42.66	0.86	2.66	8.81E-02	119.78	74.39	1.21	8.82E-02
M17-UC1	38.08	1.69	2.33	2.47E-02	141.31	7.62	2.5	2.49E-02
G20.08-0.14N	35.87	4.17	1.55	2.10E-02	119.45	272.81	2.12	2.11E-02
G24.78+0.08A1	29.89	0.99	3	4.20E-02	123.56	93.93	1.14	4.21E-02
G28.20-0.04N	33.09	3.25	1.71	2.16E-02	130.54	23.92	0.88	2.18E-02
G34.26+0.15B	45.53	0.87	2.66	8.45E-02	131.44	44.21	2.66	8.46E-02
G12.89	37.23	25.32	1.16	6.85E-03	134.16	327.76	1.88	6.99E-03
G43.80-0.13	37.69	4.57	1.56	1.78E-02	105.97	29.23	1.34	1.77E-02
G45.07+0.13	42.62	3.52	1.84	1.39E-02	129.98	29.37	1.56	1.42E-02

5.1.1 Optical Depth

I calculated the beam-averaged optical depth at 870 μm using the expression,

$$\tau_{870\,obs} = -\ln\left|1 - \frac{F_{\nu\,,\,peak}}{\Omega_B B_\nu(T_c)}\right| \quad , \tag{12}$$

where for the temperature I use the value of T_c . The values are listed in column 9 of tables 6 and 7. The maximum value is 0.088, so the assumption of optically thin at 870 μm is correct and I can also use this result for further analysis.

5.1.2 Column Density

Knowing the temperature of the cold component and assuming that the dust emission is optically thin at 870 μm, I calculate the column density from the expression,

$$N(H_2)_{870\mu m} = \frac{S^{peak}_{870\mu m}}{\Omega_B B_{870\mu m}(T_c)\,\sigma_{870\mu m}} \quad , \tag{13}$$

where Ω_B is the beam solid angle (in this case 18.22"x18.22") and $S^{peak}_{870\,\mu m}$ is the peak value of the 870 μm flux density emission. $\sigma_{870\,\mu m}$ is the cross section per hydrogen molecule and is given by,

$$\sigma_\nu = R_{dg}\,\mu\, m_H\, \kappa_\nu \quad , \tag{14}$$

where R_{dg} is the dust-to-gas mass ratio, μ is the mean molecular weight per hydrogen molecule, m_H is the hydrogen mass, and κ_ν is the absorption opacity per mass of dust. I used R_{dg} = 1/100, μ = 2.8, and for κ_ν = 1.73 $cm^2\ g^{-1}$ (interpolated to 870 μm from Table 1, Col. 5 of Ossenkopf & Henning (1994)). The column densities of the cold gas are listed in column 5 of tables 8 and 9.

5.2 SED Fit: Second step

In this step I use the full model (expressions 5 to 8), incorporating the GLIMPSE and MSX flux data. For the warm and hot components the optical depth τ_ν is not parametrized but computed from,

$$\tau_\nu^{w,h} = N_{w,h} * \sigma_\nu \quad , \tag{15}$$

where N is the H_2 column density and σ_ν is the dust opacity. I considered 4 models for the dust opacities: the Weingartner & Draine (2001) models with RV = 5.5 ,like Morales et al (2009), and RV= 3.1, and the models from Ossenkopf & Henning (1994) for thin and thick ices each with 10^6 cm^{-3} as number density. For the cold component I use the same expression as in step one. Thus,

$$F_\nu = F_\nu^c + F_\nu^w + F_\nu^h \quad , \tag{16}$$

where,

$$F_\nu^h = \Omega_h B_\nu(T_h)(1 - e^{-N_h \sigma_\nu}) e^{-(N_c + N_w)\sigma_\nu/2} \quad , \tag{17}$$

$$F_\nu^w = \Omega_w B_\nu(T_w)(1 - e^{-N_w \sigma_\nu}) e^{-N_c \sigma_\nu/2} \quad , \tag{18}$$

$$F_\nu^c = \Omega_c B_\nu(T_c)(1 - e^{-(\nu/\nu_0)^\beta}) \quad , \tag{19}$$

Without assumptions there are 11 unknowns of the model to solve; 3 temperatures, 3 column densities, 3 angular sizes, β and ν_0. The cold component parameters T_c, Ω_c and N_c, were taken as fixed; with T_c equal to the value obtained in the previous step (see column 2 of tables 6 and 7), Ω_c the geometric mean of the minor and major axes of the fitted ellipse of the intensity distribution map (see columns 5 and 6 of Table 3), and N_c the value calculated in chapter 5.1.2 (see column 5 of tables 8 and 9).

The values of N_w and N_h are small enough that the $(1 - e^{-N_{w,h}\sigma_\nu})$ terms of the model become $N_{w,h}\sigma_\nu$ so they depend linearly with N. This term is then multiplied by $\Omega_{w,h}$ in the model, becoming degenerate as both terms can't be fitted simultaneously. To solve this problem I constrain one parameter in terms of the other: I assume a constant density for all regions, which implies that $N_{w,h} = \sqrt{\Omega_{w,h}/\Omega_c}\, N_c$ for the warm and hot regions. The densities are unlikely to be uniform, but because the SED is a very simple model, a more realistic density distribution is unnecessary at this level. I ended with ν_0 , β, Ω_h , Ω_w , T_h, and T_w as free parameters for the model.

At first I have 13 points (flux densities) that I can use to fit the parameters of the SED: 1 from ATLASGAL (at 870 μm), 4 from IRAS (12, 25, 60, 100 μm), 4 from MSX (8.3, 12.1, 14.7, 21.3 μm) and 4 from GLIMPSE (3.6, 4.5, 5.8, 8.0 μm). But I ignored the IRAS 12 μm flux from the fitting because its different resolution with MSX and the very close proximity between those two bands (IRAS 12 μm and MSX 12.1 μm). In the Spitzer bands when more than one object falls inside the cold dust, for the contribution to the SED I chose the closest one to the dust peak. So I ended with 12 data points and 6 unknowns, and I solved it using a least squares method with constrains. Appendix A shows this method in

more detail and details the typical errors in the obtained parameters of this model. As starting values for the warm and hot temperatures I used the mean values obtained by Morales et al 2009. For the N_w and N_h I started with 1/5 and 1/20 of the N_e value respectively, and for the turnover frequency and power law index I used the mean obtained by the previous SED fitting. But I have 4 dust absorption models, so for each of these models I fitted the values of the parameters for all the sources. To choose between the 4 solutions models for each source, I used the chi-square value of the fits and I used the one with lower chi-square.

5.3 SED fits: results and analysis

Figures 47, 48, 49 and 50 show the SEDs and their corresponding fits for all the sources. Flux symbols are a filled triangle for 0.87 mm ATLASGAL, circles for IRAS, squares for MSX, and stars for GLIMPSE. All the fitted values are listed in tables 8 and 9.

Table 8: SED results, Guzman list

Name	Tc [°K]	ν_{0c} [THz]	β	NH2c [10^{22} cm^{-2}]	Tw [°K]	NH2w [10^{22} cm^{-2}]	Th [°K]	NH2h [10^{22} cm^{-2}]	χ^2_ν
G300.9674+01.1499	37.5	5.27	1.67	7.81	66.7	2.6	321.4	9.87E-02	0.20
G301.1364-00.2249	46.3	3.26	1.38	19.95	180.4	1.28	522.2	9.97E-02	0.48
G302.1515-00.9488	32.7	23.21	1.46	1.33	85.8	0.21	400.4	1.14E-02	0.15
G308.9176+00.1231	36.8	7.71	1.76	3.29	176.6	0.23	408.3	6.46E-02	0.04
G311.1359-00.2372	31.0	27.25	1.6	0.73	98.6	0.06	405.6	3.66E-03	0.10
G317.4298-00.5612	37.8	12.23	1.52	2.64	141.8	0.16	476.3	2.33E-02	0.07
G317.8908-00.0578	35.6	41.44	1.27	1.69	93.5	0.14	385.8	8.92E-03	0.07
G326.5297-00.4186	41.5	2.33	3.3	0.4	106.1	0.11	472.4	4.04E-03	0.04
G326.7249+00.6159	35.9	1.2	3.43	9.61	195.6	0.69	599.9	4.81E-02	0.29
G329.4761+00.8414	32.3	10.69	1.67	2.17	78.5	0.41	403.3	2.05E-02	0.12
G330.2935-00.3946	35.8	4.8	1.66	7.14	137.3	0.55	432.2	5.91E-02	0.18
G332.8256-00.5498	43.8	1.61	1.87	27.59	200.0	4.32	504.1	6.85E-01	1.11
G333.0162+00.7615	31.3	7.54	1.44	10.79	88.2	1.04	384.4	8.66E-02	0.32
G333.1306-00.4275	37.3	2.41	1.81	24.63	199.9	2.19	517.2	2.81E-01	0.89
G336.9842-00.1835	39.5	8.16	1.81	1.6	142.8	0.11	451.5	1.61E-02	0.05
G337.4032-00.4037	37.6	2.16	1.74	20.08	98.1	2.36	395.2	2.58E-01	1.02
G337.7051-00.0575	31.4	1.12	2.67	19.61	198.7	0.76	438.4	9.80E-02	0.88
G337.7091+00.0932	31.3	2.9	1.76	12.11	73.0	1.96	353.6	1.01E-01	0.32
G337.8442-00.3748	34.8	7.1	1.63	3.77	157.2	0.31	445.3	5.10E-02	0.05
G338.9217+00.6233	31.8	3.64	1.91	7.55	81.5	1.25	382.1	7.32E-02	0.17
G340.2480-00.3725	32.2	15.07	1.3	6.83	102.0	0.45	354.0	4.30E-02	0.04
G345.4938+01.4677	38.8	6.27	1.27	17.68	151.9	1.3	455.0	2.31E-01	0.26
13134-6242	37.9	4.8	1.28	13.44	76.3	3.03	380.8	1.18E-01	0.49
13471-6120	41.9	7.45	1.41	7.12	135.6	0.87	430.3	9.72E-02	0.07
15437-5343	37.7	14.02	1.36	4.01	115.0	0.29	482.9	2.14E-02	0.06
16547-4247	35.4	2.78	1.49	22.87	80.6	4.11	600.0	1.42E-01	0.91

Name	Tc [°K]	ν_{0c} [THz]	β	NH2c [10^{22} cm^{-2}]	Tw [°K]	NH2w [10^{22} cm^{-2}]	Th [°K]	NH2h [10^{22} cm^{-2}]	χ^2_ν
17238-3516	30.2	2.18	2.72	3.88	61.0	1.06	382.7	2.74E-02	0.19
17439-2845	29.6	3.15	2.15	6.95	72.2	1.56	437.8	5.52E-02	0.20
17559-2420	30.9	30.5	1.55	1.55	109.4	0.08	380.2	6.87E-03	0.12
18048-2019	28.1	4.9	2.31	1.22	80.6	0.11	484.0	7.93E-03	0.05
18064-2020	33.8	2.06	3.01	4.78	80.5	1.19	333.6	4.78E-02	0.48
18314-0720	33.3	10.53	1.69	3.17	142.0	0.16	366.4	1.58E-02	0.27
18316-0602	32.9	12.9	1.17	9.5	83.3	1.39	436.9	1.07E-01	0.07

Table 9: SED results, HCHII regions

Name	Tc [°K]	V0c [THz]	β	NH2c [10^{22} cm^{-2}]	Tw [°K]	NH2w [10^{22} cm^{-2}]	Th [°K]	NH2h [10^{22} cm^{-2}]	χ^2_ν
G9.62+0.19F	38.0	2.91	1.73	13.3	99.1	1.99	387.4	2.44E-01	0.47
G10.47+0.03	42.7	0.92	2.47	32.8	197.2	1.28	430.0	3.02E-01	1.36
M17-UC1	38.1	1.65	2.36	24.67	200.0	2.26	597.8	1.72E-01	0.90
G20.08-0.14N	35.9	4.17	1.55	8.59	102.4	0.86	378.4	6.58E-02	0.13
G24.78+0.08A1	29.9	1.09	2.76	23.05	83.4	3.09	454.4	1.71E-01	0.75
G28.20-0.04N	33.1	3.21	1.71	12.1	162.6	0.72	443.1	1.24E-01	0.05
G34.26+0.15B	45.5	1.09	2.15	46.54	--	--	350.9	4.05E+00	2.73
G12.89	37.2	24.52	1.16	4.22	146.2	0.2	511.2	3.27E-02	0.13
G43.80-0.13	37.7	4.87	1.52	7.62	77.2	1.97	400.0	6.89E-02	0.02
G45.07+0.13	42.6	3.5	1.84	6.86	129.2	0.86	453.6	9.95E-02	0.07

5.3.1 Analysis of the model fits

All the fits were obtained using the same method but not all used the same constrains due to some technical issues. They can be summarized in four problems that arise from lose initial restrictions;

- Sometimes a couple of parameters diverged and better constrains were used
- A particular problem of diverging parameters was that of T_w and N_w. For the 3.6 μm point the hot component is the dominant term, and if T_w starts to become too big the $\{\exp(h\nu/kT_w)-1\}$ term in the Planck law becomes $h\nu/kT_w$ so T_w becomes a linear term with N_w, making a degeneracy between these terms.
- The other 2 are because physical assumptions of the model were not achieved, specifically I had assumed a 3 model component and in two cases this does not apply to the fitted results.
    - N_h becomes larger than N_w in the fit making the hot component larger than the warm one, and so it dominates in the entire spectrum relegating the warm component to be very small and so contradicting the model assumption of 3 components.
    - T_h becomes equal to T_w, and so the warm and hot components are intrinsically the same, making it a 2 component model.

To solve these issues, stronger restrictions were used like forcing a maximum ratio between the N_h and N_w values. The more important restriction was the upper limit for T_h, and was set at 600°K. In the case of G34.26+0.15B even after imposing restrictions for three components, a two component model was a better fit for the data so I kept this model.

5.3.2 Reduced Chi-square

To assess the goodness of fit I computed the reduced chi-square (Appendix A) for each object. Conservative flux uncertainties of 20% were taken for IRAS, MSX and IRAC data, and 15% for ATLASGAL. The obtained values are in the range of 0.02 to 2.04 with a mean of 0.36. Only two values were over 1.2 which indicates that almost all the values were well fitted within the given uncertainties, and these two values (G10.47 and G34.26) were not too far from 1.0 as not to contradict the conclusion of a obtaining a good fit. This result was expected for G34.26 as a three component model converged into a two component one, which limits lowers the probability to achieve a good fit ti the data. The majority of the values were under 0.5 probable due to the fact that I assumed a conservative uncertainty. Were I to use a more exact uncertainty the obtained reduced chi-square should not be so over-fitted.

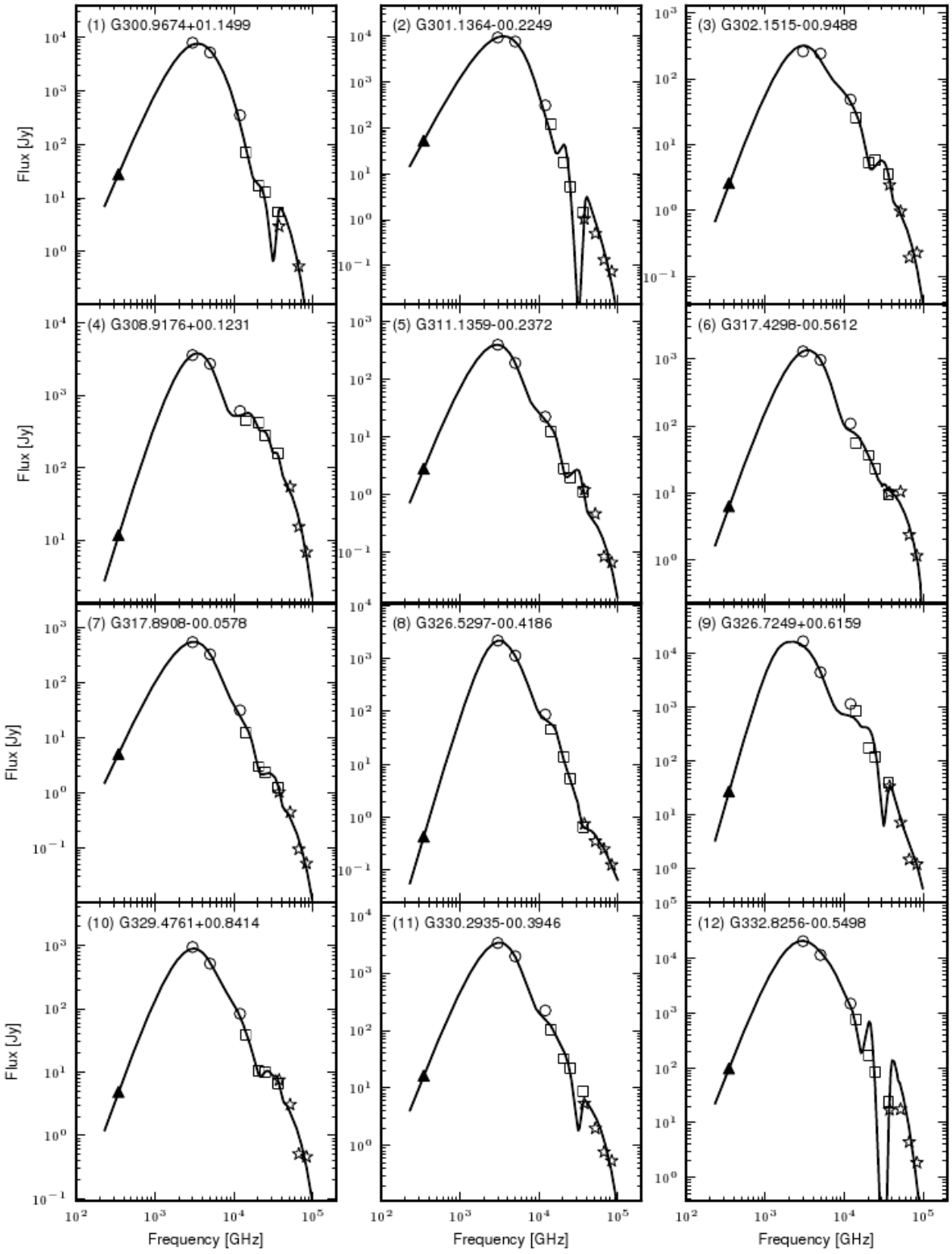

Figure 47: SEDs and their corresponding fits as described in section 5.2 Flux symbols are a filled triangle for 0.87 mm ATLASGAL, circles for IRAS, squares for MSX, and stars for GLIMPSE.

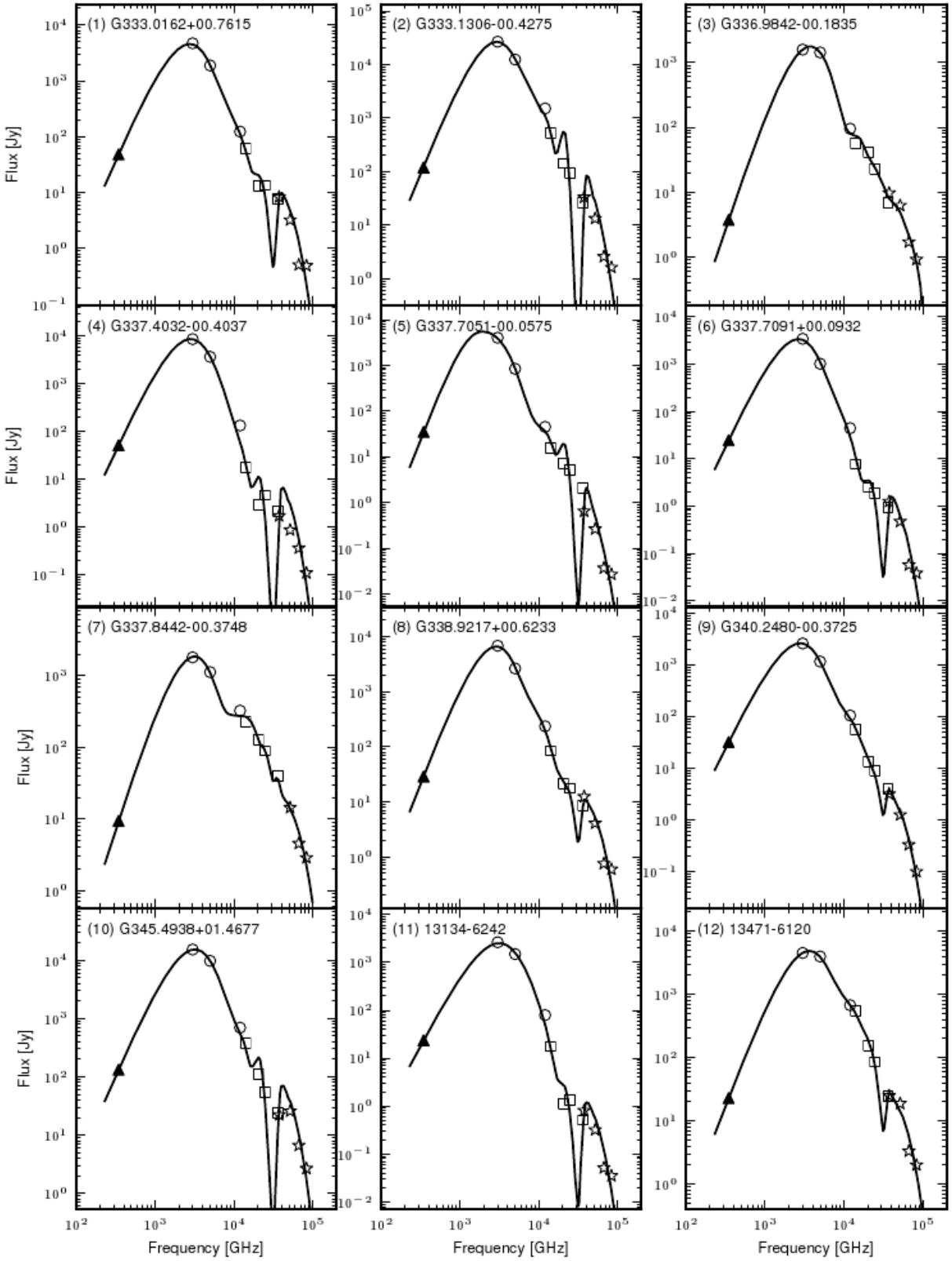

Figure 48: SEDs and their corresponding fits as described in section 5.2 Flux symbols are a filled triangle for 0.87 mm ATLASGAL, circles for IRAS, squares for MSX, and stars for GLIMPSE.

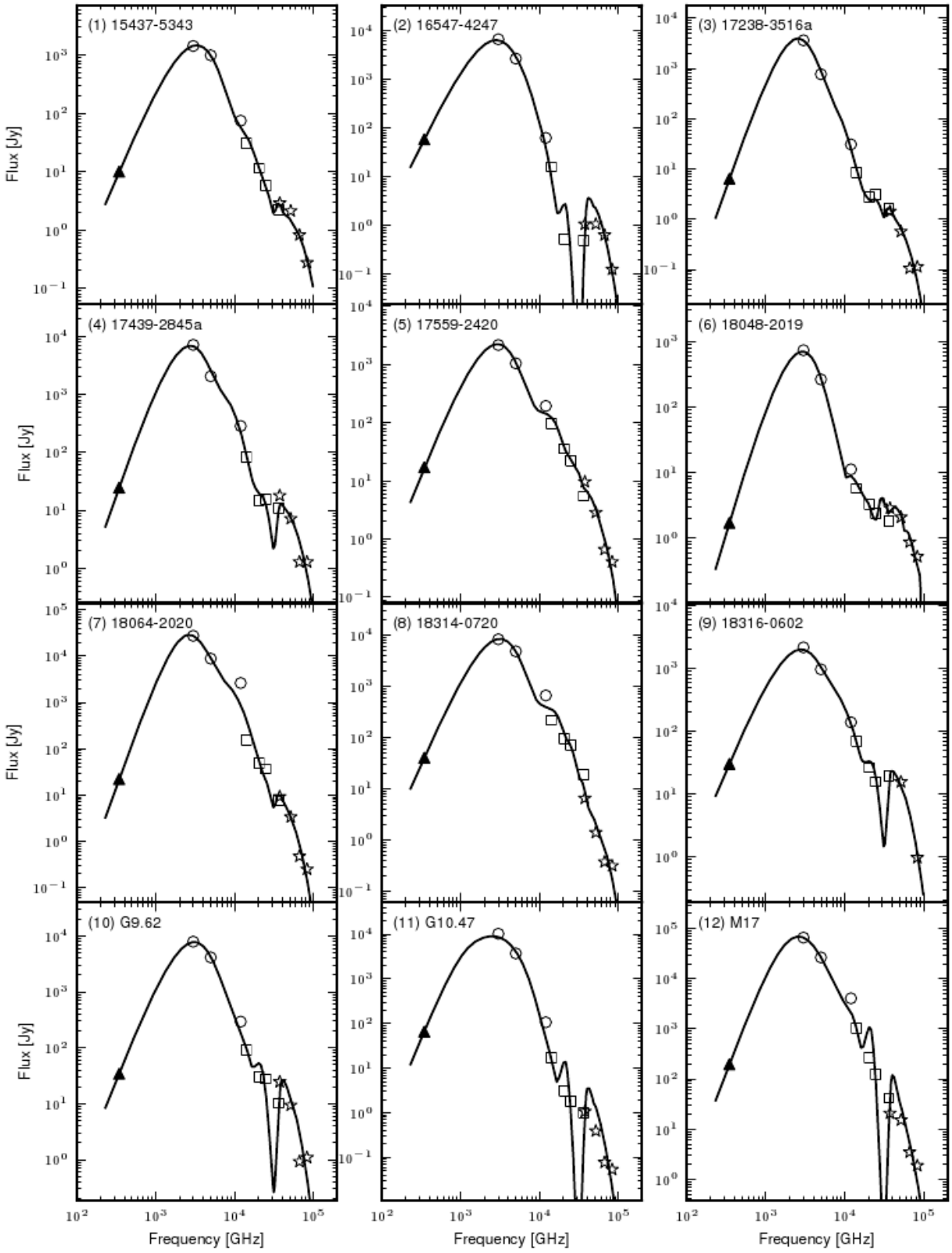

Figure 49: SEDs and their corresponding fits as described in section 5.2 Flux symbols are a filled triangle for 0.87 mm ATLASGAL, circles for IRAS, squares for MSX, and stars for GLIMPSE.

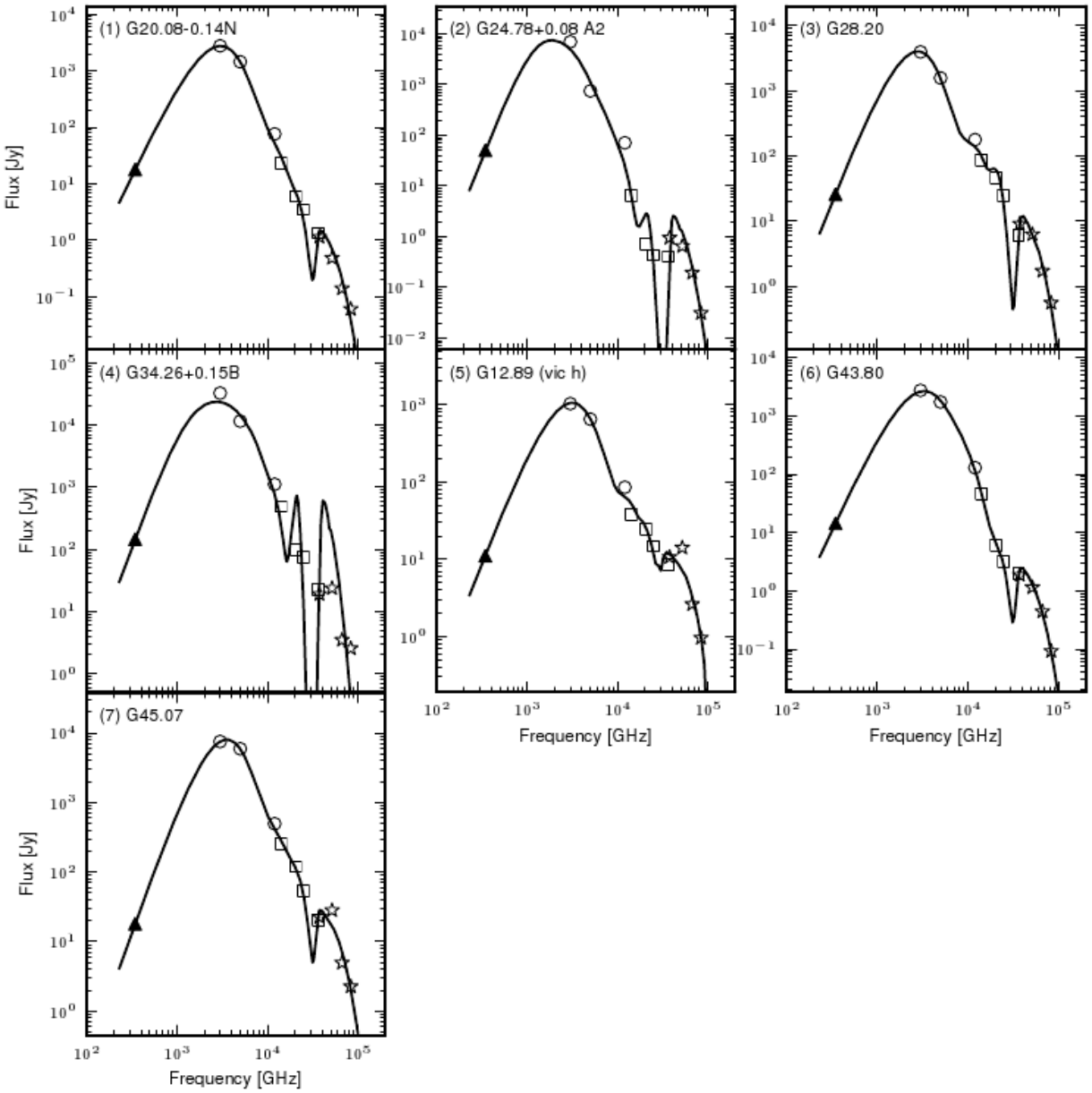

Figure 50: SEDs and their corresponding fits as described in section 5.2 Flux symbols are a filled triangle for 0.87 mm ATLASGAL, circles for IRAS, squares for MSX, and stars for GLIMPSE.

5.3.3 Dust Opacity Models

I had considered 4 models; Weingartner & Draine (2001) RV = 3.1 (model 1) and RV= 5.5 (model 2) models, plus the thin (model 3) and thick (model 4) ice models with 1e6 of number density of Ossenkopf & Henning (1994). A comparison of the four models used is shown in Figure 51. As I fitted the data to each model, I kept the one with lower chi-square.

I ended with 34 objects using model 1, 4 using model 2, 4 using model 3, and only one using model 4. But Figure 51 shows that both Draine models are almost identical, and between both of them they have 38 objects (88%). So the Draine models better adjust the observed fluxes to this three components model.

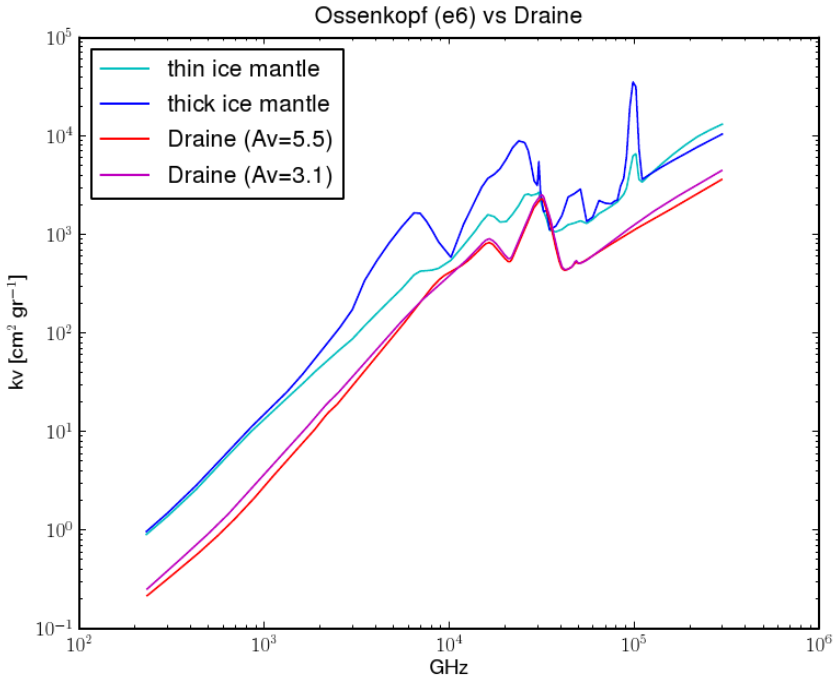

Figure 51: Dust Opacity Models

Chapter 6

Physical characteristics of the regions

From the 870 μm emission maps and the SED fits, I obtained several physical parameters of the regions which characterize these environments. In this section I present the summary of these characteristics, including histograms, for the Guzman sample (33 objects).

6.1 Sizes

As I have the distance to the objects I convert the angular sizes to sizes (column 5 table 10). I found that the mean size of the cores is 0.48 pc, with a standard deviation of 0.36 pc. Although, as seen in the histogram, the median, 0.35 pc, should be a better indicator of the typical value as there is a high peak in the 0.2-0.4 pc range, which contains half of the whole sample (17 objects).

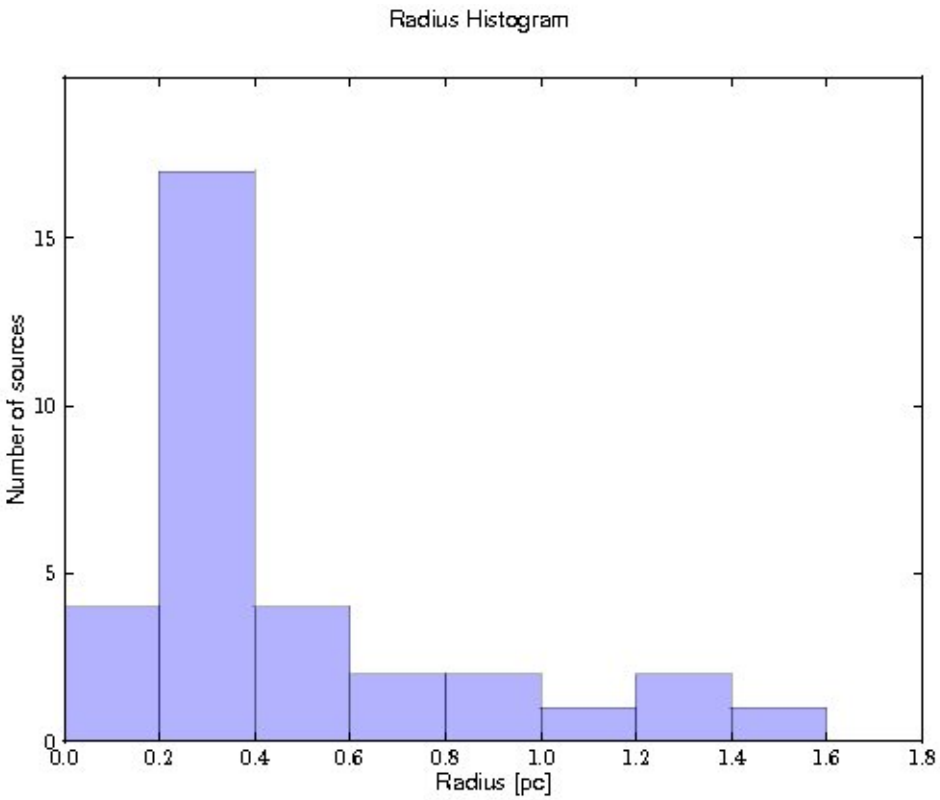

Figure 52: Histogram of radius

6.2 Temperatures

6.2.1 Cold component temperature

The temperatures of the cold component are in the range 28-47 °K (but mainly in the 30-40 °K range, 27 of 33 objects) with a mean value of 35.3°K and standard deviation of 4.2 °K

.

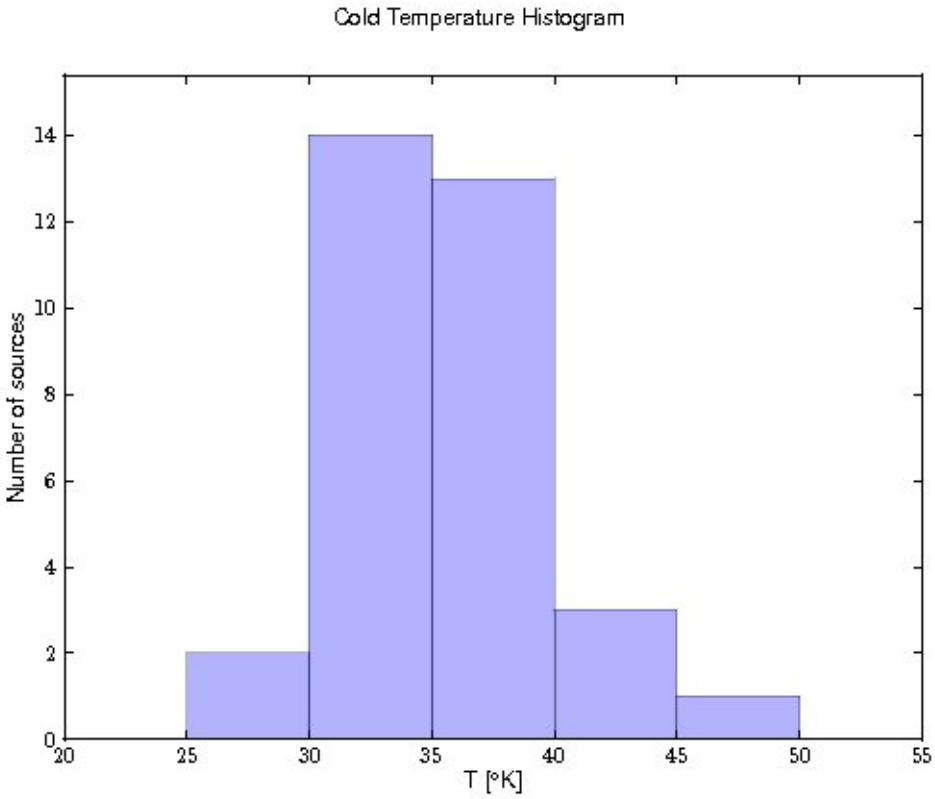

Figure 53: Histogram of temperature of cold component

6.2.2 Warm and hot component temperature

The warm and hot component temperatures are in the 60-200 °K, 320-600 °K range, and with mean values of 118 °K and 430 °K, respectively. Histograms are shown in figures 54 and 55, respectively.

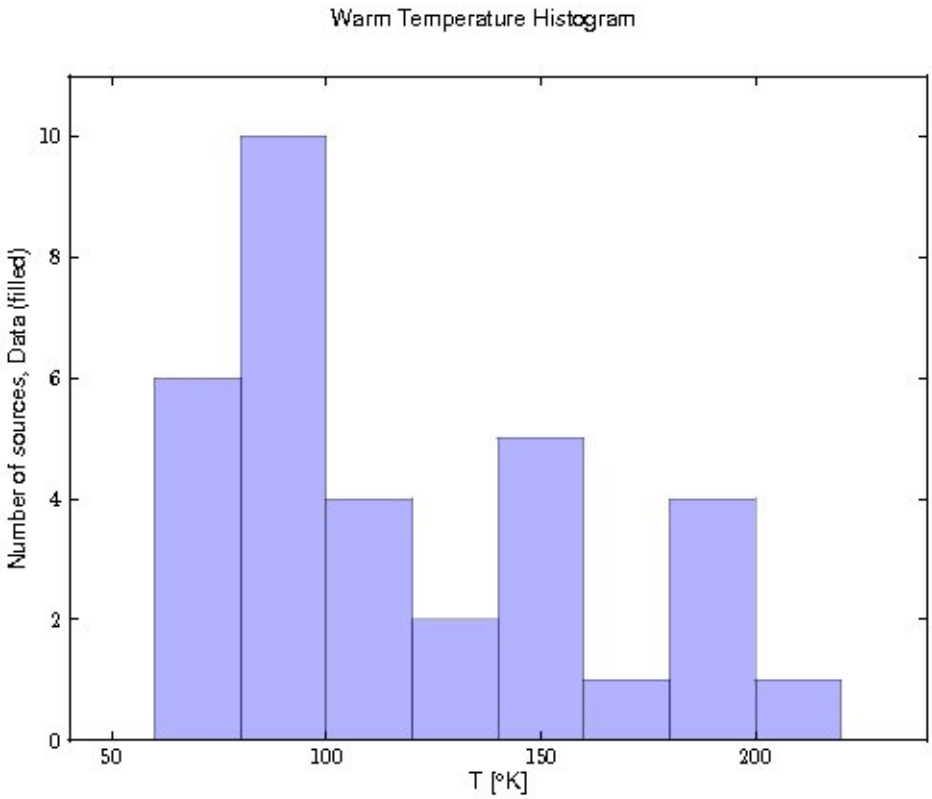

Figure 54: Histogram of temperature of warm component

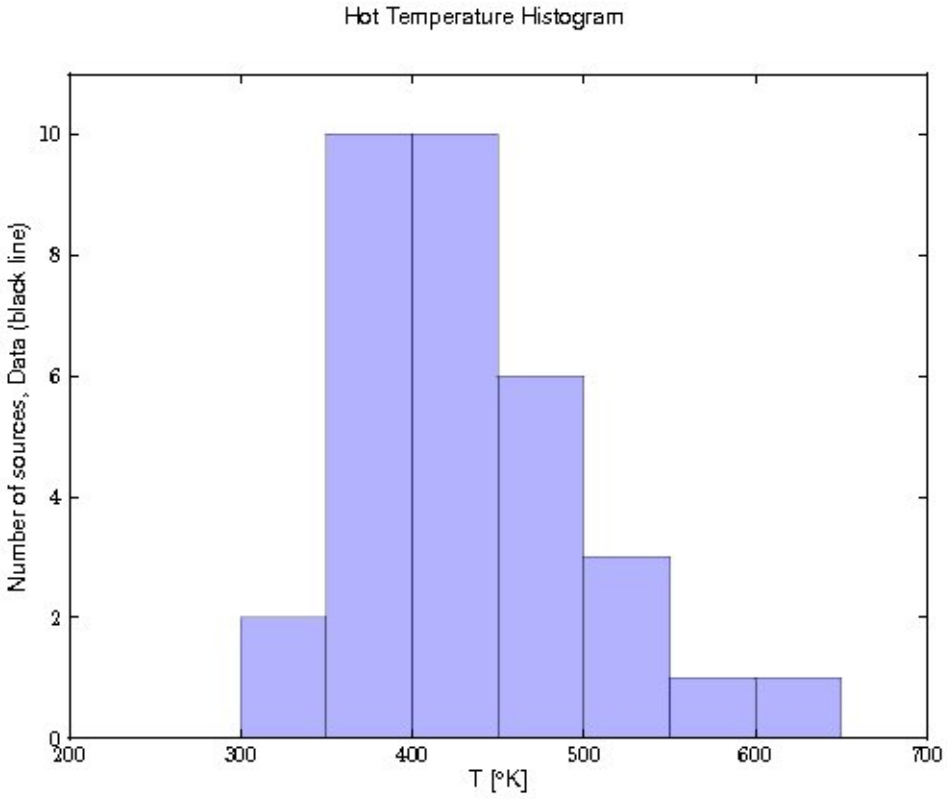

Figure 55: Histogram of temperature of hot component

6.3 Column Density

The cold component column density ranges from 0.4 to 28.6 (x 10^{22} cm^{-2}) with a mean of 8.71.

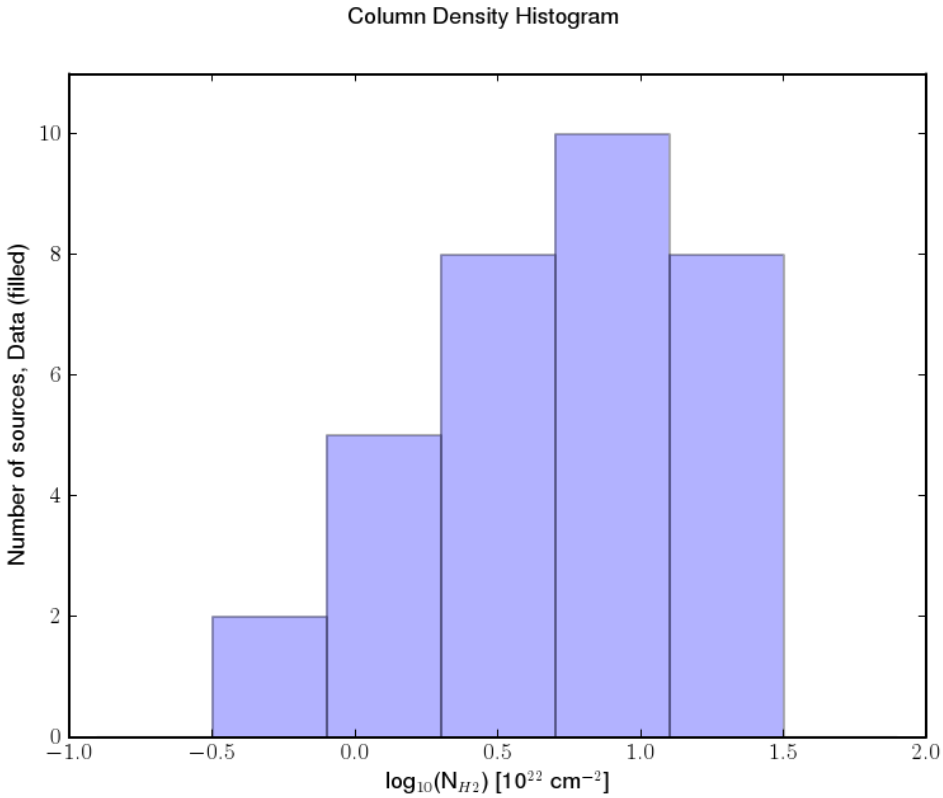

Figure 56: Histogram of column density

6.4 Mass

As the objects are optically thin at 870μm, following Hildebrand (1983), I use the following expression to obtain the mass of the core.

$$M = \frac{D^2 F_\nu R}{B_\nu(T_d)\kappa_\nu} \quad . \tag{20}$$

I used the same values than for the column density, R = 100, μ = 2.8, and for κν = 1.73 $cm^2\ g^{-1}$ (Ossenkopf & Henning 1994). I adopted this value for the absorption opacity per mass of dust because it is from the same table used by the two main comparison studies, so as not to have to rescale the results to be able to compare the samples. The masses are listed in column 2 table 10.

For the Guzman list the masses obtained range from 8.66 to 1.6 x 10^4 $M_\odot$, with a mean value of 1.94 x 10^3 $M_\odot$. Figure 57 shows a histogram of the logarithm of the masses.

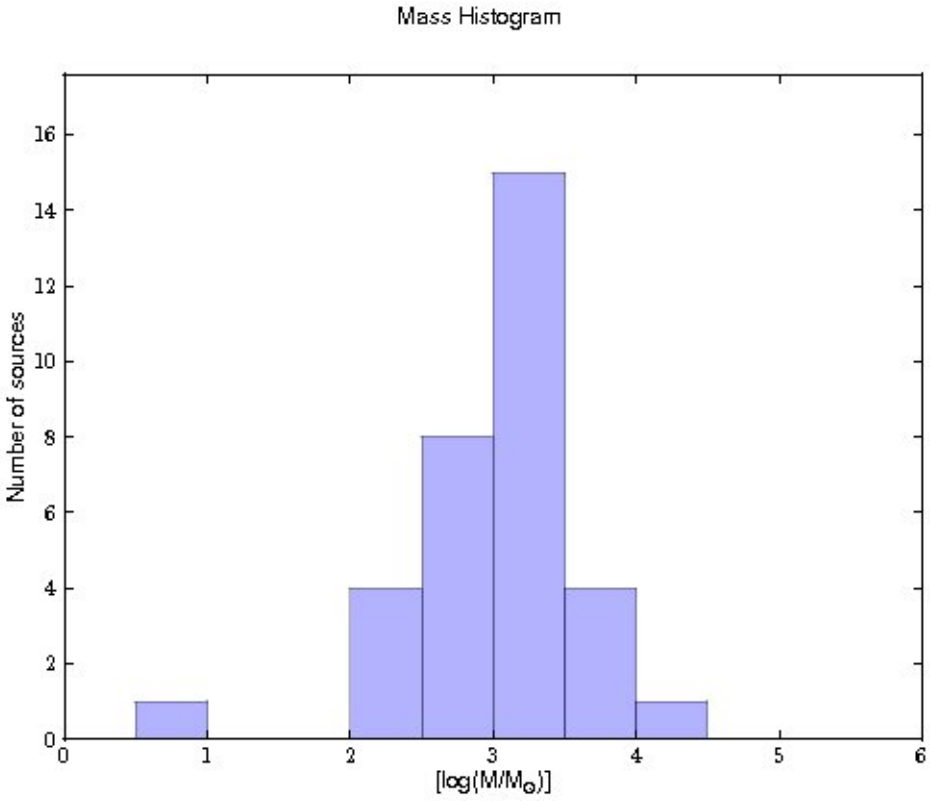

Figure 57: Histogram of mass

6.5 Density

With the assumption of spherical symmetric and constant density I derive the density of the cores (column 4 table 10). The mean density is 1.75 x 10^5 cm^{-3}.

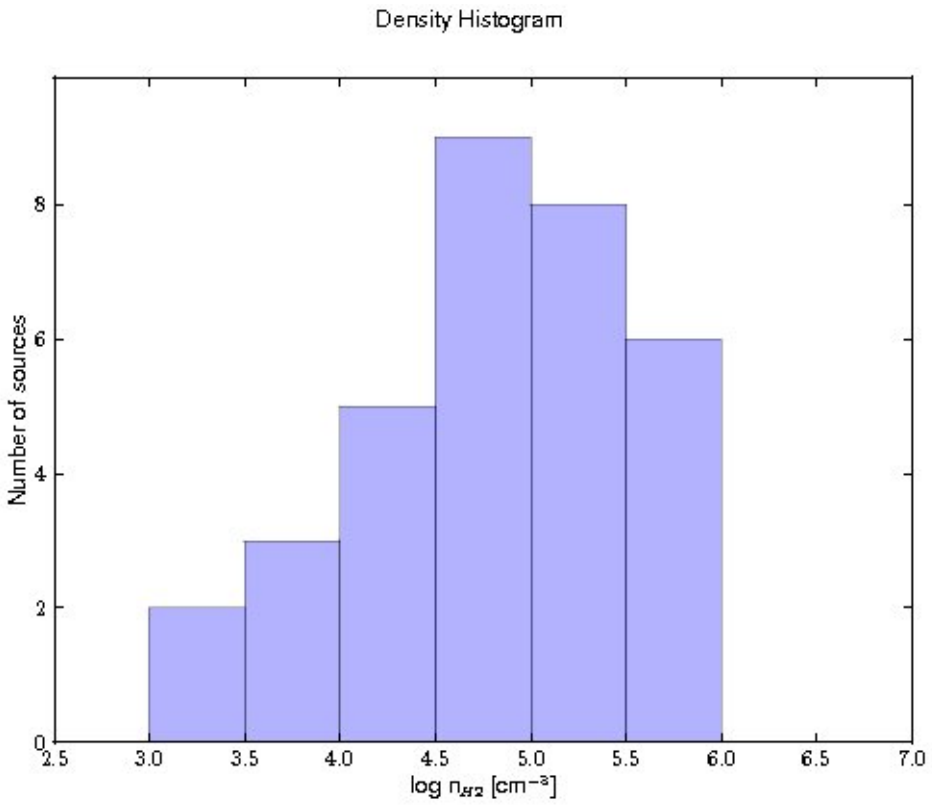

Figure 58: Histogram of density

6.6 Luminosity

The total luminosity of the regions can be computed using two approaches. In the first one, I use the IRAS fluxes and calculate an infrared flux and luminosity using the formulas of Casoli et al. (1986),

$$F_{IR}(10^{-13}\,W\,m^{-2}) = 1.75(F_{12}/0.79 + F_{25}/2 + F_{60}/3.9 + F_{100}/9.9) \quad (21)$$

$$L_{IR} = 4\pi\, d^2\, F_{IR} \quad (22)$$

Alternatively, since a fit to the SED is available for each object, I integrate it over the frequencies to get the total bolometric flux,

$$F_{bol} = \int_0^\infty F_\nu d\,\nu \quad (23)$$

A comparison of the fluxes computed using the two approaches is presented on Figure 59. While there is a good agreement between the two it can be seen that F_{IR} tends to be larger than F_{bol} by a factor of typically 1.3. So for this kind of objects, the Casoli's formula tends to overestimate the total luminosity.

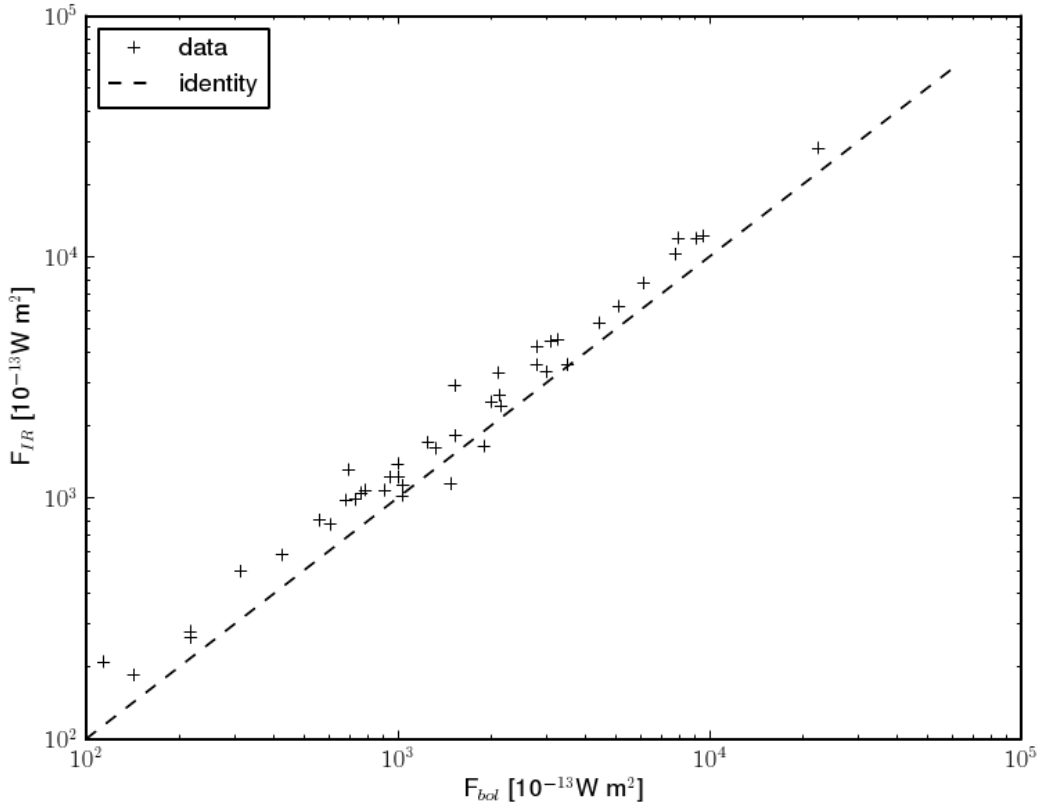

Figure 59: F_{bol} vs F_{IR}

The value of the luminosity in solar luminosities [$L_\odot$] ranges between 1.7 x 10^4 and 6.6 x 10^5, with a mean value of 1.4 x 10^5, which suggests that these objects are probably sites of O and B star formation. Figure 60 shows an histogram of the luminosities.

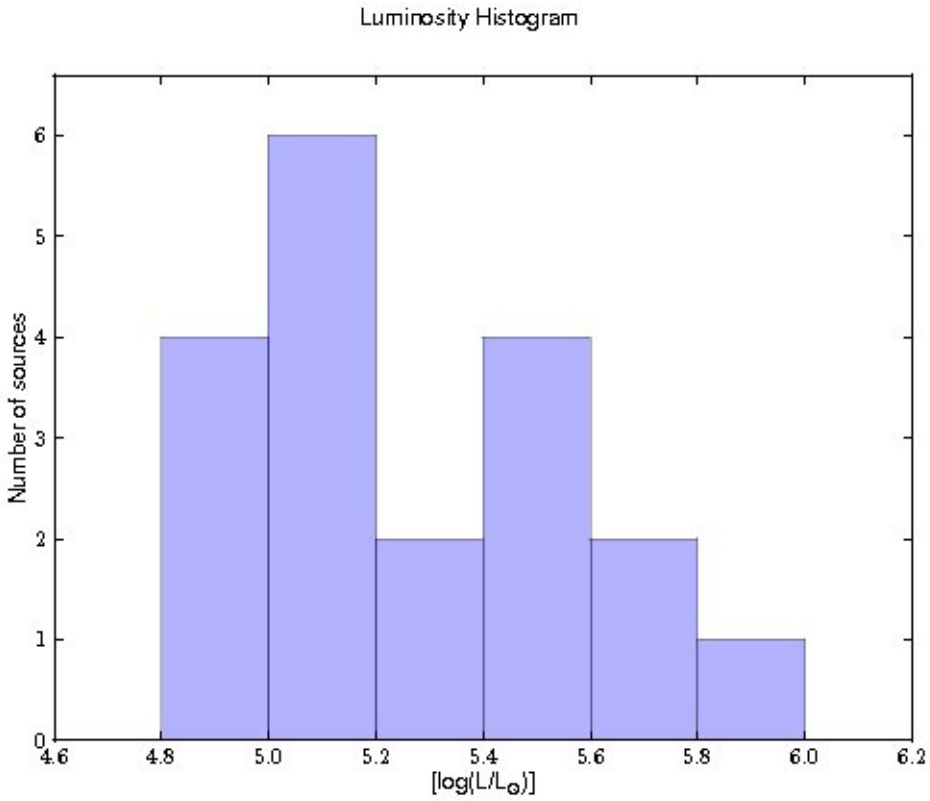

Figure 60: Histogram of luminosity

6.7 Summary

Table 10 shows the derived physical parameters for all the sources from the Guzman list and the HCHII regions list. Tables 11 and 12 present the minimum, maximum and mean values for each physical characteristic for each of the two samples, Guzman and HCHII, respectively.

Table 10: Derived Data

Source	Mass [$M_\odot$]	$N(H_2)$ [10^{-22} cm $^{-2}$]	$n(H_2)$ [cm $^{-3}$]	Radius [pc]	$\tau_{870\mu m}$
G300.9674+01.1499	1.36E+03	7.81	7.99E+04	0.39	0.011
G300.9674+01.1499	1.36E+03	7.81	7.99E+04	0.39	0.010
G301.1364-00.2249	2.01E+03	19.9	5.68E+05	0.23	0.045
G302.1515-00.9488	1.14E+03	1.33	8.70E+03	0.77	0.002
G308.9176+00.1231	8.52E+02	3.29	2.67E+04	0.48	0.004
G311.1359-00.2372	1.87E+03	0.73	1.81E+03	1.53	0.001
G317.4298-00.5612	3.70E+03	2.64	1.37E+04	0.98	0.004
G317.8908-00.0578	2.66E+03	1.69	5.73E+03	1.17	0.002
G326.5297-00.4186	8.66E+00	0.4	7.51E+04	0.07	0.002
G326.7249+00.6159	5.73E+02	9.61	1.93E+05	0.22	0.014
G329.4761+00.8414	3.87E+02	2.17	2.65E+04	0.37	0.003
G330.2935-00.3946	1.06E+03	7.14	1.23E+05	0.31	0.013
G332.8256-00.5498	2.80E+03	27.6	6.67E+05	0.24	0.056
G333.0162+00.7615	1.69E+03	10.8	8.69E+04	0.41	0.012
G333.1306-00.4275	3.74E+03	24.6	2.13E+05	0.39	0.028
G336.9842-00.1835	2.04E+02	1.6	3.69E+04	0.27	0.003
G337.4032-00.4037	1.35E+03	20.1	6.16E+05	0.2	0.041
G337.7051-00.0575	1.62E+04	19.6	1.91E+05	0.66	0.043
G337.7091+00.0932	1.73E+03	12.1	2.38E+05	0.29	0.024
G337.8442-00.3748	2.52E+02	3.77	1.10E+05	0.2	0.007
G338.9217+00.6233	1.66E+03	7.55	7.77E+04	0.42	0.011
G340.2480-00.3725	1.43E+03	6.83	4.70E+04	0.47	0.007
G345.4938+01.4677	7.27E+02	17.7	4.10E+05	0.18	0.025
13134-6242	5.32E+02	13.4	7.58E+05	0.13	0.035
13471-6120	1.47E+03	7.12	1.10E+05	0.36	0.013
15437-5343	6.84E+02	4.01	5.68E+04	0.35	0.007

Source	Mass [$M_\odot$]	$N(H_2)$ [10^{-22} cm^{-2}]	$n(H_2)$ [cm^{-3}]	Radius [pc]	$\tau_{870\mu m}$
16547-4247	1.34E+03	22.9	6.97E+05	0.19	0.045
17238-3516	6.67E+02	3.88	5.90E+04	0.34	0.007
17439-2845	5.41E+03	6.95	3.00E+04	0.85	0.009
17559-2420	1.29E+03	1.55	2.39E+03	1.23	0.001
18048-2019	1.58E+02	1.22	2.24E+04	0.29	0.002
18064-2020	2.83E+02	4.78	5.28E+04	0.26	0.005
18314-0720	4.07E+03	3.17	7.56E+03	1.23	0.003
18316-0602	8.66E+02	9.5	1.63E+05	0.26	0.014
G9.62	2.36E+04	13.3	6.93E+04	1.06	0.025
G10.47	1.66E+04	32.8	5.31E+05	0.48	0.088
M17	2.81E+03	24.7	2.03E+05	0.36	0.025
G20.08-0.14N	7.39E+03	8.59	9.81E+04	0.64	0.021
G24.78+0.08 A2	7.44E+03	23.1	2.71E+05	0.46	0.042
G28.20	6.11E+03	12.1	1.13E+05	0.57	0.022
G34.26+0.15B	4.00E+03	46.5	1.02E+06	0.24	0.085
G12.89	1.27E+03	4.22	4.55E+04	0.46	0.007
G43.80	3.96E+02	7.62	3.27E+05	0.16	0.018

Table 11: Physical Characteristics Summary, Guzman sample

Physical Characteristic	Minimum	Maximum	Mean
Size [pc]	0.07	1.53	0.48
Cold c. temperature [°K]	28	46	35.3
Warm c. temperature [°K]	60	200	118
Hot c. temperature [°K]	320	600	430
Column Density [10^{22} cm^{-2}]	0.4	27.6	8.7
Mass [$M_\odot$]	8.6	16200	1940
Density [cm^{-3}]	1.8×10^3	7.6×10^5	1.75×10^5
Luminosity [$L_\odot$]	1.7×10^4	6.6×10^5	1.4×10^5

Table 12: Physical Characteristics Summary, HCHII sample

Physical Characteristic	Minimum	Maximum	Mean
Size [pc]	0.24	1.06	0.48
Cold c. temperature [°K]	30	45.5	38
Warm c. temperature [°K]	77	200	132
Hot c. temperature [°K]	350	600	440
Column Density [10^{22} cm^{-2}]	4.2	46.5	18
Mass [$M_\odot$]	1300	23600	6000
Density [cm^{-3}]	4.6×10^4	10^6	3.1×10^5
Luminosity [$L_\odot$]	6.0×10^4	2.4×10^6	5.7×10^5

6.8 Radio Luminosity

With the luminosity derived in this thesis I can reassess if Guzman sample is selecting sources with less radio luminosity than optically thin HII regions. In the case of an optically thin HII regions the 8.6 GHz free-free continuum monochromatic luminosity expected from a source that emits N_i Lyman continuum photons per second, and every ionizing photon is absorbed, the expected relation is (Guzman et al. 2011),

$$\frac{4\pi D^2 F_\nu}{N_i h} = 1.707 \left(\frac{\nu}{8.6\,GHz}\right)^{-0.11} \left(\frac{T}{8000\,K}\right)^{0.38} \tag{24}$$

The ionizing photon rate for stars of spectral types between O and B class V stars are taken from the models (e.g. Panagia 1973, Vacca et al. 1996, and Sternberg et al. 2003).

Figure 61 shows the sources (crosses, red for Guzman sample and blue for the HCHII regions), the expected monochromatic luminosity for three star models (continuous lines, green Panagia model, cyan Vacca et al model, and yellow Sternberg et al. model), and the expected monochromatic luminosity for a star cluster (dashed line, Guzman et al. 2011). All sources are under-luminous, except a few, compared to an optically thin HII region with a single O or B star, and most of them are even under-luminous compared to an HII region excited by a cluster of stars.

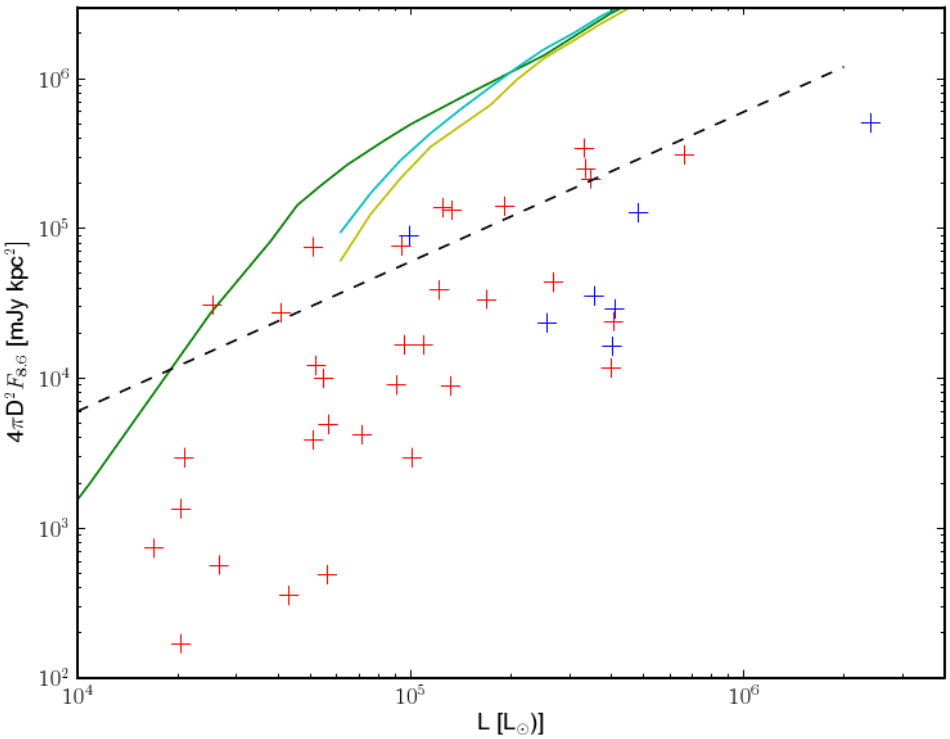

Figure 61: Total monochromatic 8.6 GHz luminosity versus total luminosity

Chapter 7

Comparison with other samples

7.1 Comparison with Faundez et al (2004)

To put in perspective the characteristics of the objects in the sample, I will compare our results with the Faundez et al (2004) sample which consists of 146 1.2 mm/IRAS sources corresponding to massive and dense cores harboring massive YSO's (sample F04). I will make use of histograms, and statistical tools to make a robust comparison.

I used mainly four types of statistical tests (using the python implementation of each):

- Kolmogorov-Smirnof (KS) test ; this is a two-sided test for the null hypothesis that 2 independent samples are drawn from the same continuous distribution. If the samples do not come from the same distribution, there are three possibilities; they have different mean, different variance or they are drawn from different types of distribution (eg Normal vs Cauchy).
- Student-t test; this is a two-sided test for the null hypothesis that 2 independent samples have identical average (expected) values.
- Bartlett test; test with the null hypothesis that all input samples have equal variances. This test is sensitive to departures from normality. The Levene test is an alternative that is less sensitive to departures from normality.
- Normality tests; test with the null hypothesis that the sample comes from a normal distribution. I used three different tests; Shapiro and Wilk test, Anderson and Darling test, and D'Agostino and Pearson's test. This is mainly used to test the sensitivity of the Bartlett test, because when the samples are normal it has better performance than the Levene test (NIST/SEMATECH 2011).

I will only compare the Guzman Sample with the F04 sample as the HCHII region sample is too small to have robust statistical significance.

7.1.1 Cold Temperatures

Figure 62 shows an histogram of the cold temperatures of the objects in the Guzman sample (filled), and Faundez et al. (2004) samples.

Although the temperatures in the two samples fall in the same range [20-50 °K], it appears that my sample has a higher mean. The KS test to the null hypothesis that the two samples are drawn from the same distribution gives us a p-value of 8.7e-4. Thus I reject the null hypothesis with a 99% of confidence concluding that indeed they are not the same distribution. From the Student t-test and Levene test (normality tests conclude that the temperature of F04 are not normally distributed, unlike our data), I conclude that statistically the means are not equal (99% confidence, α=0.01) but I cannot reject the null hypothesis of equal variances.

Another way to see the mean difference between our data and the F04 sample is perform a Montecarlo simulation. In this case the statistical significance of the Student-t test is big and to perform a

simulation may not be useful to draw new conclusions but is more illustrative, and sets a basis for other cases. For the Montecarlo simulation I create additional data sets (in this case I created 10000) for each sample, mine and F04. Then I calculate the estimator I want to analyze for each set and get conclusions, mainly confidence intervals, from the distribution of the estimator in all the data sets. For this I use the bootstrap method which uses the empirical distribution as the underlying distribution, so I draw with replacement from the empirical sample to create the new data samples.

Figure 63 (I) shows the distribution of estimator mean, from which I obtain a 1-sigma value of 0.66. So I can give a 68% confidence interval (CI) for the mean cold temperature of the sample (34.560 , 36.020)or a 90% CI (34.092 , 36.525). Thus at the 90% of confidence, our mean is above the 32 °K mean temperature of the F04 sample. Or I could use the mean difference estimator which after re-sampling takes the difference of the new sets of data. Figure 63 (ii) shows that the difference in the mean temperatures is always more than zero, indicating that indeed our sample has higher mean cold temperature than the F04 sample. And I even can say with 90% confidence that our sample is 1.85 °K hotter.

Additionally I show in Figures 63 (iii) and (iv) the same results for the variance of the temperature. The main conclusion is that in the 1-sigma range the difference in the variances of both samples has the zero difference [-10.420 , 0.420]. Hence, I cannot conclude that the variances are statistically different. This supports the result of the Levene test, in which the p-value is 0.96 so I cannot reject the null hypothesis of equal variances.

Appendix B shows all the bootstrap distributions obtained through Montecarlo simulations for all the parameters analyzed.

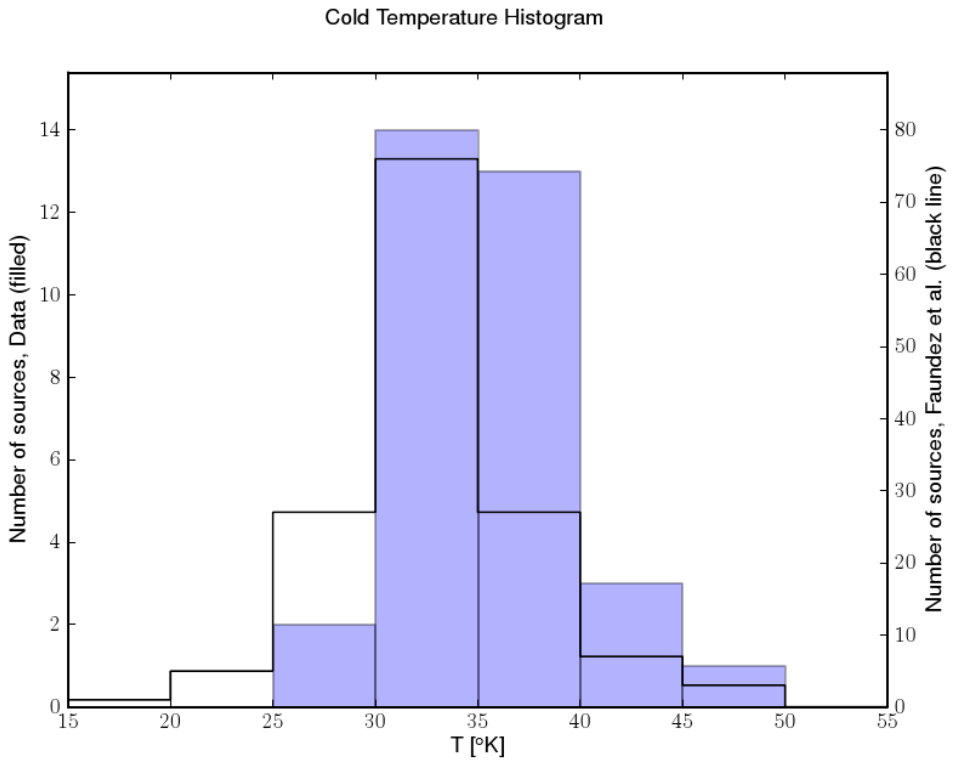

Figure 62: Cold Component Temperature Histogram, vs SF

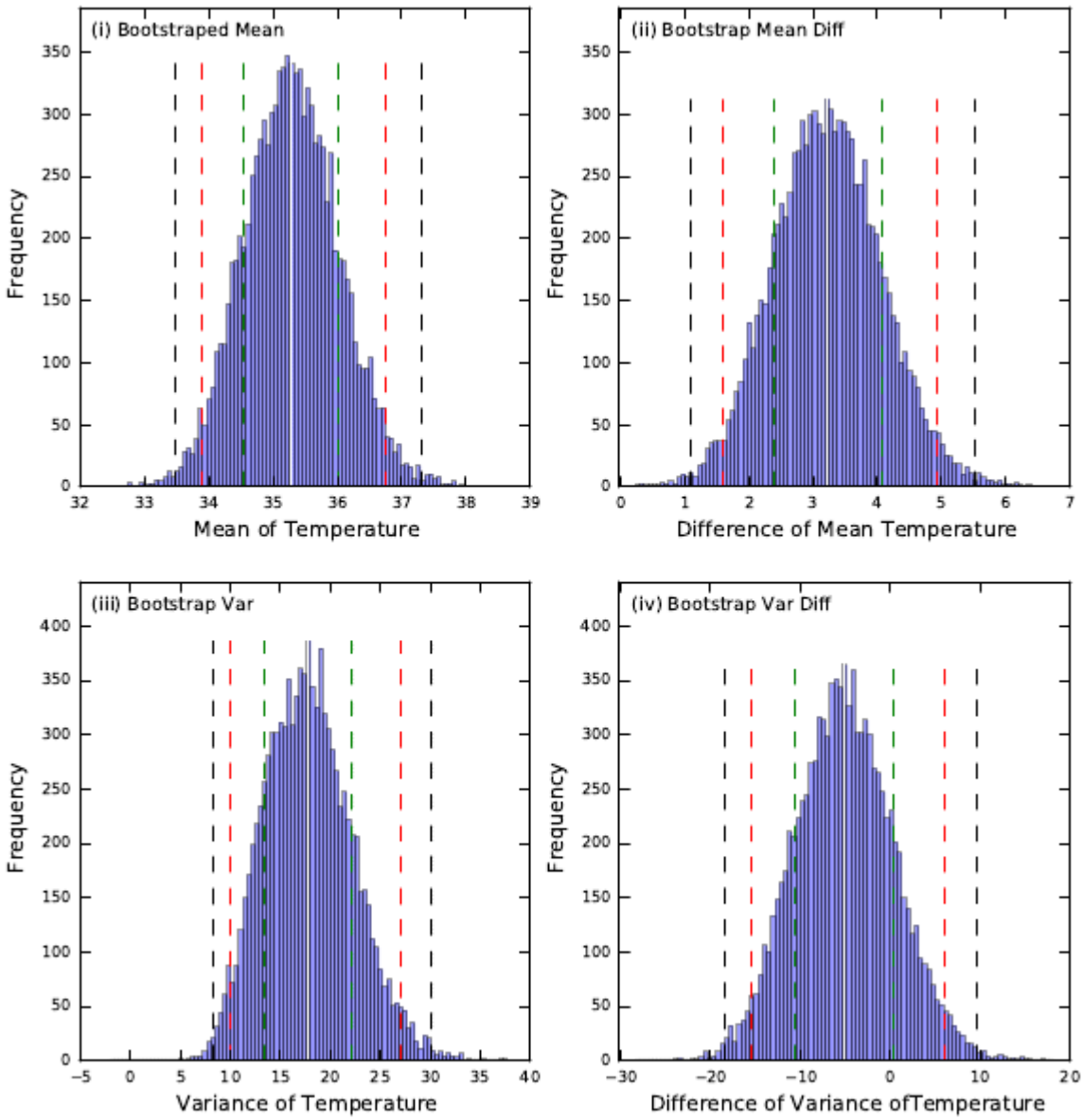

Figure 63: Bootstrap Distributions; (i) mean temperature, (ii) temperature's mean, difference vs Faundez et al (2004), (iii) temperature's variance , and (iv) temperature's variance, difference vs Faundez et al (2004)

7.1.2 Sizes

Figure 64 shows an histogram of the sizes for Guzman sample as well as for the F04 sample. The KS-test tells us that our sample comes from the same distribution than the other sample (p-values of 0.76). For mean and variance comparison, simulations (Appendix B) tells us that at the 90% confidence level I can't reject equal means and I reject equal variance with F04; result also backed by the statistical tests.

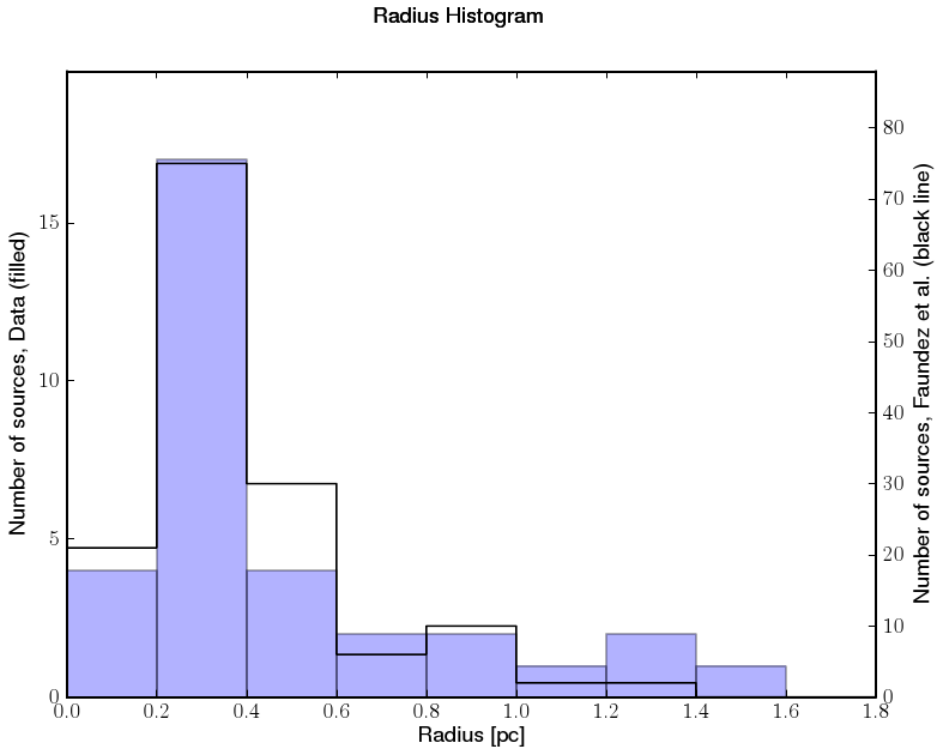

Figure 64: Radius Histogram, vs SF

7.1.3 Column Density

Figure 65 shows an histogram of the logarithm of the column density for Guzman and Faundez samples. Statistical tests and Montecarlo simulations conclude that the samples are different and that ours has a lower mean.

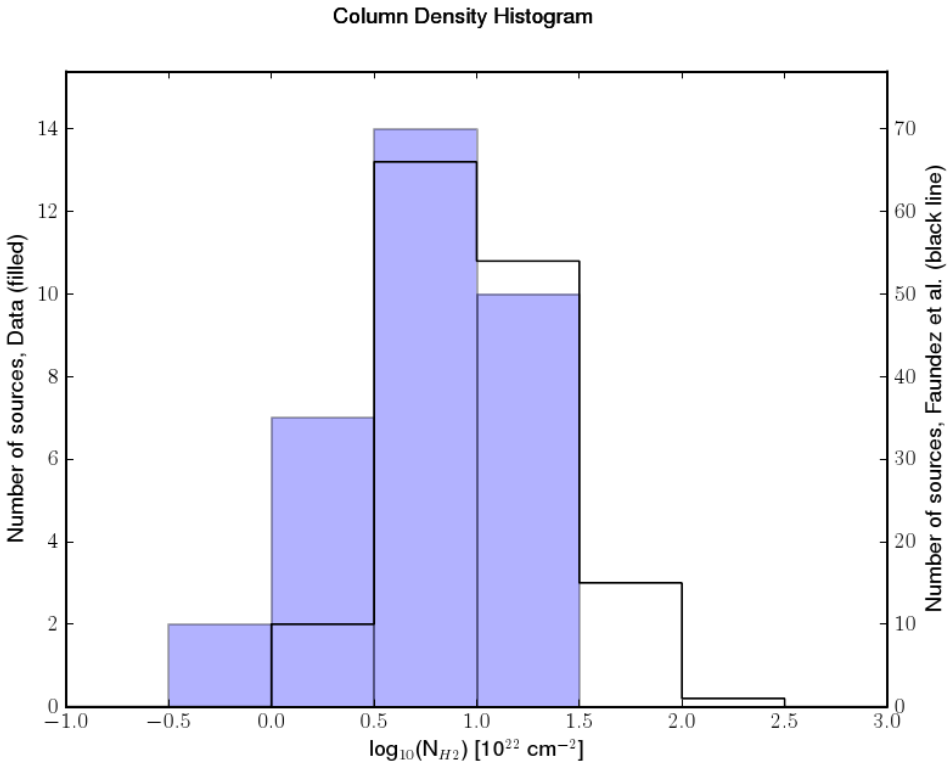

Figure 65: Column Density Histogram, vs SF

7.1.4 Mass

Figure 66 shows an histogram of the logarithm of the masses for Guzman and Faundez samples.

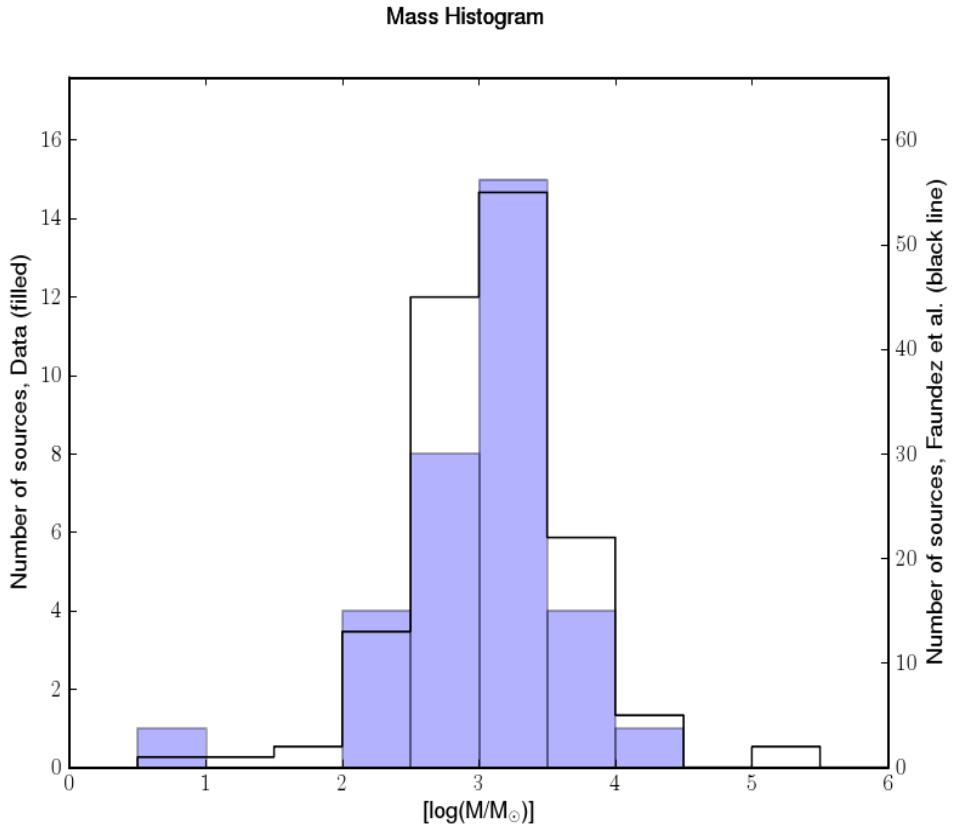

Figure 66: Mass Histogram, vs SF

Using statistical tests I find that both samples come from the same distribution, having the same mean and variance as I can't reject the null hypothesis (KS test p-value = 0.94), means (t-test p-value = 0.5) and variance (levene p-value = 0.61).

Using Montecarlo simulations the 90% confidence interval of the difference in mean mass is (-0.254 , 0.094) and in variance mass is (-0.272 , 0.214), meaning as both intervals have the 0.0 difference that statistically I can't say that both samples have different mean or variance.

7.1.5 Density

Comparing to the Faundez sample I have to be careful because the histogram showed in Figure 67 seems to show that our sample (filled) is a slightly less massive one and so they originate from different type of samples. The tests make us reject at 90% confidence the hypothesis of equal mean compared to both samples. For the Faundez sample at 68% confidence the simulations agree with this conclusion but not at 90%. Additionally I can't reject equal distributions given the KS-test results (p-value = 0.29), and at 95% confidence both types of analysis agree in not discarding equal means. So I best conclude that my sample doesn't deviate from the F04 sample.

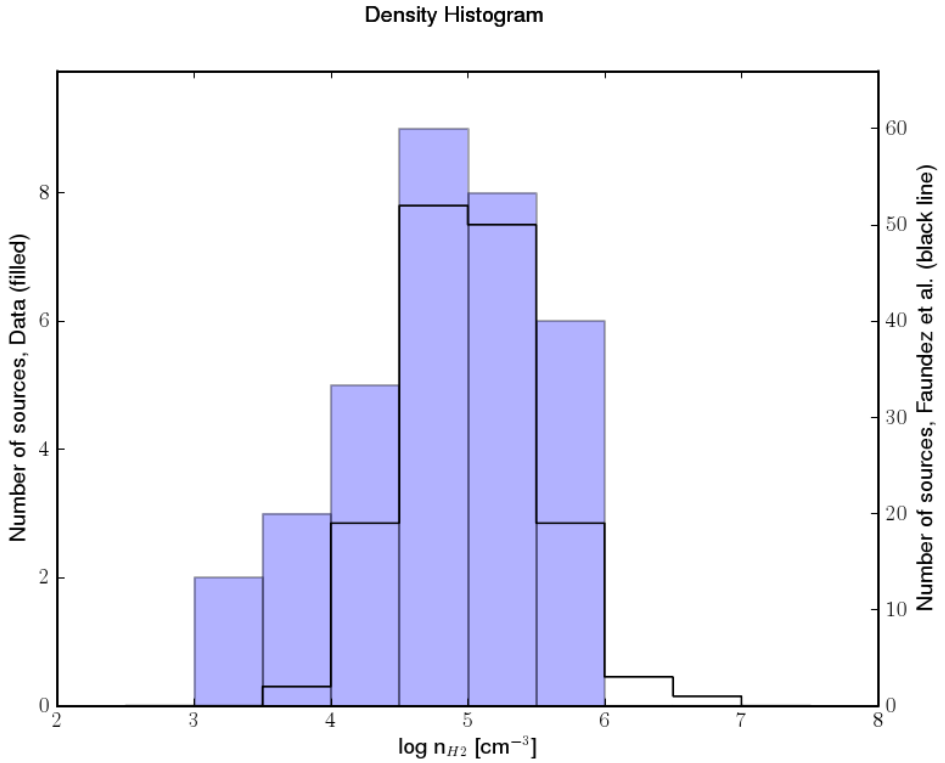

Figure 67: Density Histogram, vs SF

7.1.6 Luminosity

The histogram, Figure 68, shows that the two samples look the same in the mid part but towards the wings our sample tends to be more luminous. Proceeding as before (using statistical tests and Montecarlo simulations) the main conclusion is that statistically they have the same mean and variance.

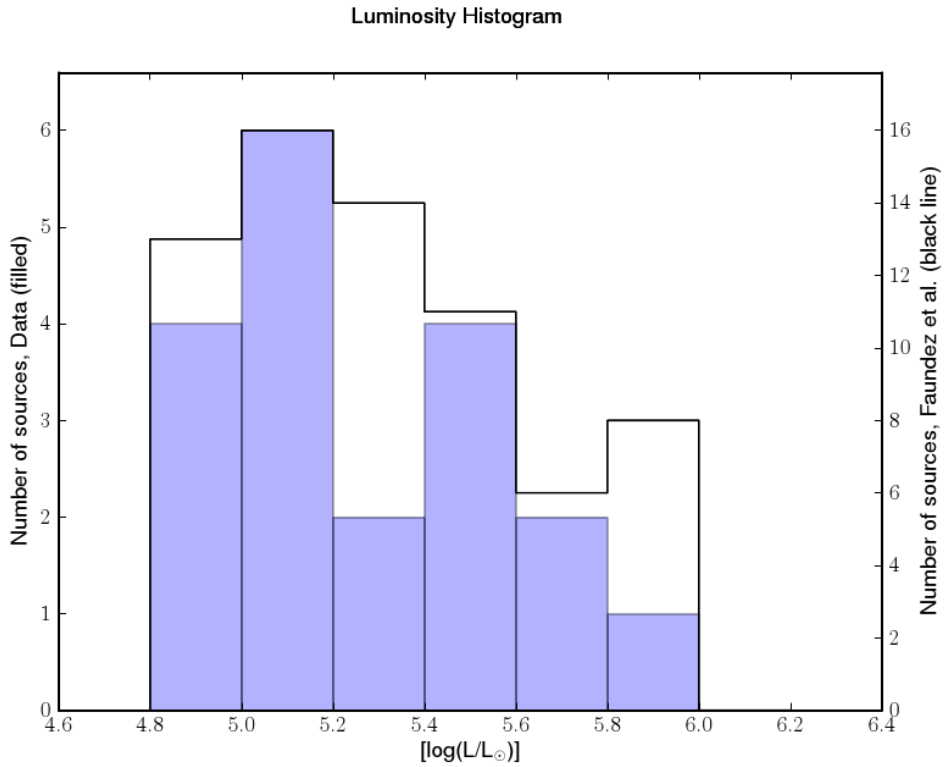

Figure 68: Luminosity Histogram, vs SF

7.1.7 Summary of Comparison

Table 13 shows a summary of the different physical characteristics for the F04 sample and the Guzman sample, table 14 summarizes the results of the comparison between the Guzman's objects and those in the Faundez et al (2004) sample, and table 15 shows the p-values obtained from five statistical tests. In table 14 I tabulate if the distributions are equal or if our sample has a bigger or smaller value with 90% confidence. If they are statistically different, the percentage shown in the table represents the percentage the 90% CI minimum difference is to the mean value of our sample, so it represents the minimum difference between the samples. These percentages are 5 or lower so although there are differences they are small compared to the mean values themselves.

Table 13: Summary of characteristics

Physical Characteristic	Mean (Guzman S)	σ (Guzman S)	Mean (F04 sample)	σ (f04 sample)
Size [pc]	0.48	0.36	0.39	0.23
Cold c. temperature [°K]	35.3	4.22	32.1	4.8
Column Density [$\log_{10}(10^{22}$ cm$^{-2})$]	0.73	0.47	1.03	0.37
Mass [$\log_{10}(M_\odot)$]	3.01	0.56	3.09	0.6
Density [$\log_{10}$(cm^{-3})]	4.83	0.69	5.01	0.48
Luminosity [$\log_{10}(L_\odot)$]	4.95	0.43	4.83	0.73

Table 14: comparison of parameter distributions

Parameter	Faundez et al
Size	Equal
Cold temperature	Greater (5%)
$\log_{10}$(Column Density)	Lower (20%)
$\log_{10}$(Mass)	Equal
$\log_{10}$(Density)	Equal
$\log_{10}$(Luminosity)	Equal

Table 15: Statistical tests p-values

Parameter	Kolmogorov-Smirnov test	Student-T test	Levene test	D'Agostino-Pearson test	Shapiro-Wilk test
Size [pc]	0.76	0.11	0.03	<0.01	<0.01
Cold c. temperature [°K]	<0.01	<0.01	0.96	0.28	0.23
Column Density [$\log_{10}(10^{22}$ cm$^{-2})$]	<0.01	<0.01	0.04	0.46	0.3
Mass [$\log_{10}(M_{\odot})$]	0.94	0.5	0.61	<0.01	0.01
Density [$\log_{10}$(cm^{-3})]	0.29	0.08	0.01	0.51	0.31
Luminosity [$\log_{10}(L_{\odot})$]	0.3	0.39	0.05	0.43	0.35

7.2 Dense Cores

The idea is to compare the 43 results to the dense cores in which high mass stars forms, referred as maternities of massive stars (Garay 2005). The characteristics of the dense cores are (Garay & Lizano 1999):

- Linear sizes of 0.3 – 1.0 pc
- Molecular densities in the range of $2 \times 10^4 - 3 \times 10^6$ cm^{-3}
- Kinetic temperatures of 30 − 50 K
- Masses between $10^3 - 3 \times 10^4$ $M\odot$

For the 43 objects analyzed all but one, G326.5297-00.4186, have parameters within these ranges or deviate less than one order of magnitude. For the HCHII list this was expected, but this conclusion for the Guzman list tells us that the selection criteria he used is highly effective. Counting the non counterpart object, this list obtains 31 of 33 dense cores where high mass stars forms, giving a 94% efficiency.

The mean parameters I obtained were linear size of 0.48 pc, molecular density of 1.75 x 10^5 cm^{-3}, luminosity of 1.43 x 10^5 solar luminosities, temperatures of 35.3 °K, and mass of 1.94 x 10^3 solar masses, which are all in the expected range.

I had one particular case in which the above conditions were not met. For G326.5297-00.4186 I obtained a mass of 8.66 solar masses and a size of 0.07 pc which are well below the accepted values. Its morphology is from a compact object without any extended or filamentary emission. Given the much low integrated flux of this object, the peak value me was just 2.5 times the 3-sigma calculated noise, this information shouldn't be relied upon, or I should use another model to calculate the mass that doesn't rely so much in the value of the 870 μm emission.

7.3 Comparison with Other Previous Works

I already compared rigorously each individual parameter of our list to two previous works. There were differences in some parameters, but as concluded before, they were small and always less than a factor of 3 away.

Other previous surveys of dust emission, is the work of Mueller et al (2002) who conducted a survey of dust emission at sub-millimeter wavelengths (0.35 mm) towards 51 mass star formation regions (MSFR) associated with water masers. They found an average luminosity of 2.5 x 10^5 $L_\odot$, an average radius of 0.16 ± 0.1 pc, an average dust temperature of 29 ± 9 °K, and an average mass of 2.1 x 10^3 $M_\odot$, which are in good agreement with our results except that our objects have consistently larger linear sizes.

I should also compare with the results of studies of cores containing young massive stellar objects derived from molecular line observations (Cesaroni et al. 1991; Juvela 1996; Plume et al. 1997).

- Cesaroni et al (1991), using $C^{34}S$ observations towards known UCHII regions, found that the molecular clumps they observed have typically molecular hydrogen number density of 10^6 cm^{-3}, mass of ~2000 $M_\odot$, and sizes between 0.3-0.5 pc; which are, despite the high density, almost the same values I found.
- Juvela (1996) did CS and $C^{34}S$ observations towards molecular cores associated with H_2O masers, and found that they have typical densities of 10^4 – 10^5 cm^{-3}.
- Plume et al (1997) observed 150 MSFR. Using CS transitions they found for 71 of their regions the following physical conditions: mean density of 8.5 x 10^5 cm^{-3}, mean virial mass of 3.8 x 10^3 $M_\odot$, and mean radius of 0.5 pc. This sample is a bit massive (and denser) than ours but they don't deviate more than one order of magnitude.

They show a good agreement, so the 0.87 mm dust continuum is tracing the same structures than these high density molecular lines. For these objects this should be expected as by construction they have molecular lines observation to be able to calculate radial velocities and kinematic distances. The main conclusion is that the regions where massive stars form have distinctive physical characteristics, and that the 0.87 mm emission can be used to analyze these maternities of massive stars.

7.4 Relations

In this section I will investigate relationships between different parameters, using the list of 31 dense cores obtained from the Guzman list.

7.4.1 Mass vs Luminosity

I tested the relation;

$$L \propto M^{\alpha} \tag{25}$$

The linear regression fitted to the data is seen in Figure 69, which shows a direct relation. I obtain a value for α equal to 0.76, and using Montecarlo bootstrap simulation I have a 90% confidence interval of (0.589 , 0.936). The Pearson-r value was 0.78 which is statistically significant. This results suggests that more massive clouds tend to harbor more luminous stars, i.e. more massive, so to find the most massive stars in their formation one has to look in the more massive clouds.

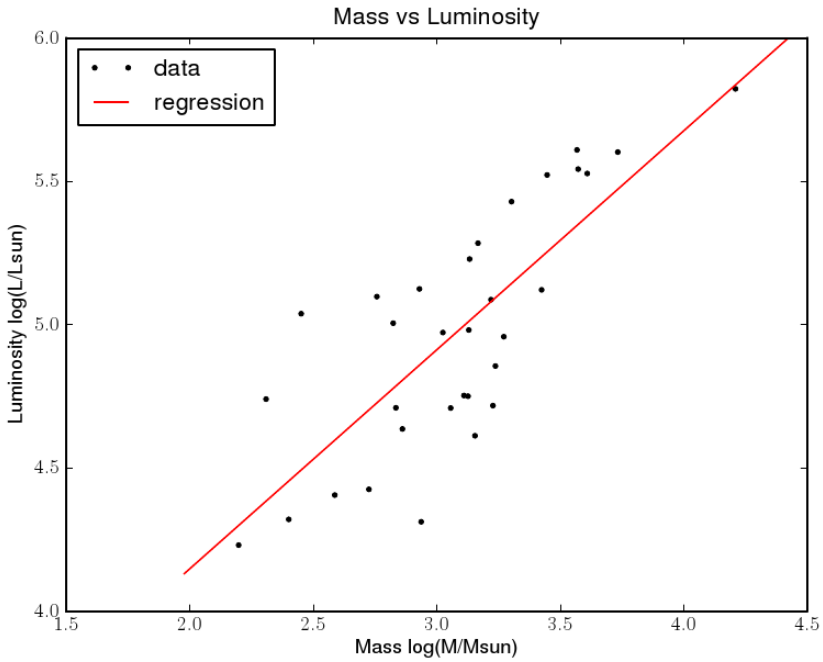

Figure 69: Mass versus Luminosity

7.4.2 Mass vs Radius

$$M \propto r^{\beta} \tag{26}$$

I obtained a value for β of 2.94, with a statistically significant r-value of 0.53. One can conclude of this that the more massive clouds are also the larger in size, despite the range of densities of the sample. In Figure 70 I show the plotted data and the fitted regression.

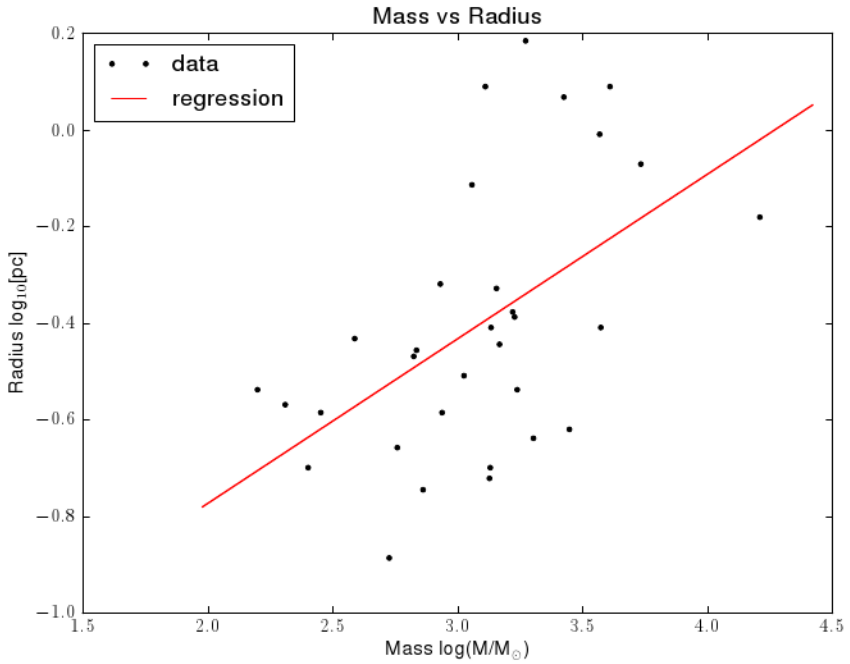

Figure 70: Mass versus Radius

7.4.3 Mass vs Density and Temperature

$$M \propto \rho^{\gamma} \quad M \propto T_c^{\delta} \tag{27}$$

In both of these cases the r-value is lower than 0.02, and so the t-test makes us reject at 90% the null hypothesis that r ≠ 0 (i.e. that a relationship exists). So the value of the cloud mass in this sample does not depend on the temperature or the density of the cloud, rather these parameters can have any value whether the cloud is of the most massive or not.

Chapter 8

Summary and Conclusions

In this chapter I present the main conclusions of this work.

I investigated the environments around jet candidates in young stellar objects (45 objects, also referred as Guzman list), and hyper compact HII regions (12 objects) which are thought to be in a similar evolutionary phase than jets. Of all these objects a total of 44 are located within the range covered by the ATLASGAL survey (34 in Guzman list and 10 in HCHII). In Chapter 4.1 I present contour maps of the sub-millimeter emission at 0.87 mm for each target, and I analyze their morphology. All targets, except one, had associated a 0.87 mm counterpart, so I ended with 43 sources to analyze. In the maps there was always a central compact object, within either a filamentary structure, a spherically symmetric extended weak envelope or an irregular structure. The most common morphology was a central compact core with an extended nearly symmetric envelope.

The ratio of the linear distance between the radio source and the sub-millimeter peak to the radius of the cold dust core shows a high correlation between the two emissions. In 37 cases (86%) the ratio is less than 1.0 and in 28 cases (65%) the ratio is less than 0.5. This result indicates that the jet candidates are located at the center of the massive cores and most likely they are being formed there.

I also retrieved mid-infrared and far-infrared data from publicly available catalogs IRAS, MSX and GLIMPSE; from which I constructed three-color (RGB) images (for MSX and GLIMPSE bands) and obtained photometric data at 12 other wavelengths. I used those data to construct a spectral energy distribution (SED) for each of the 43 objects with sub-millimeter data, with the goal of obtaining the temperature, luminosity, mass and column density. A three component model was necessary to fit the whole range of data available. I used four dust models but the Weingartner & Draine (2001) ones best fitted the data (88% of the cases). So these models best represent the characteristics of the dust in the regions considered.

The mean values I found from the SED fitting, of the physical characteristics of these objects are:

- Linear size: 0.48 pc
- Molecular density: 1.8×10^5 cm^{-3}
- Luminosity: 1.4×10^5 $L_\odot$
- Temperature: 35 °K
- Mass: 1.9×10^3 $M_\odot$

I found that the derived values of the size, mass, column density and temperature of the cold dust component, for the majority of the objects analyzed are within the range of values of massive and dense cores discussed by Garay & Lizano (1999). Only one object has different characteristics. For the hyper compact HII regions the observed parameters are within the range of massive and dense cores. Only two of the 33 objects in the Guzman list were not associated with a high mass star forming region emitting in the sub-millimeter range, which tells that the selection criteria used by Guzman has a 94% efficiency for finding massive and dense cores.

Comparing in detail the characteristics of the environments around our sample of jet candidates to

those of massive star forming regions surveyed by Faundez et al (2004), I found that our sample has statistically equal masses, densities and sizes, but ours is slightly hotter. The hotter sample may be the result of consistently selecting a more evolved core in which the pre-stellar object in the center has heated more the surrounding dust. A less detailed comparison with other works of surveys of dust emission, gives similar results.

Comparing to molecular line (CS and $C^{34}S$) emission surveys, the results are very similar. From which it can be concluded that the 0.87 mm emission is tracing the same structures as this high density molecular lines.

From the 34 objects of the Guzman list that were in the ATLASGAL coverage, Guzman et al (2011) only confirmed the presence of jets in two objects: G317.4298 and 16547-4247. This gives a 6% chance to find a jet within a massive and dense core with this criteria.

So I started with a list of probable MSFR based in infrared color criteria, and this list also presented evidence for a possible presence of jets. Using ATLASGAL data I was able to derive physical parameters for this sample. Comparing I concluded that the emission at this wavelength is tracing dense cores, so ATLASGAL will become a very useful source of information to help analyze and understand better this objects. I also concluded that indeed the objects I analyzed were regions of high mass star formation. With that important conclusion, and the detection of jets in them there would be more information to analyze of this stage in the formation of high mass stars and with it would bring a better understanding of the whole process.

Bibliography

Astrometry.net, 2010. PyLevmar – Astrometry.net. Available at: http://trac.astrometry.net/wiki/PyLevmar.

Avedisova, V.S., 2002. A Catalog of Star-Forming Regions in the Galaxy. *Astronomy Reports*, 46, pp.193-205.

Bate, M.R., 2000. Predicting the properties of binary stellar systems: the evolution of accreting protobinary systems. *MNRAS*, 314, pp.33-53.

Benjamin, R.A. et al., 2003. GLIMPSE. I. An SIRTF Legacy Project to Map the Inner Galaxy. *pasp*, 115, pp.953-964.

Beuther, H. et al., 2002. Massive molecular outflows. *A&A*, 383, pp.892-904.

Bonnell, I. A, M. R Bate, and H. Zinnecker. 1998. "On the formation of massive stars." *MNRAS,* 298, pp.93-102.

Bonnell, I.A., Vine, S.G. & Bate, M.R., 2004. Massive star formation: nurture, not nature. *MNRAS*, 349, pp.735-741.

Bronfman, L., Nyman, L.-A. & May, J., 1996. A CS(2-1) survey of IRAS point sources with color characteristics of ultra-compact HII regions. *A&As*, 115, p.81-+.

Casoli, F. et al., 1986. (C-13)O and (C-12)O observations of cold IRAS unidentified point sources in the Galaxy. *A&A*, 169, pp.281-297.

Cesaroni, R. et al., 1991. Molecular clumps associated with ultra compact H II regions. *A&A*, 252, p.278–290.

Churchwell, E., Walmsley, C.M. & Cesaroni, R., 1990. A survey of ammonia and water vapor emission from ultracompact HII regions. A&A*S*, 83, p.119–144.

Faúndez, S. et al., 2004. SIMBA survey of southern high-mass star forming regions. I. Physical parameters of the 1.2 mm/IRAS sources. *A&A*, 426, pp.97-103.

Fazio, G.G. et al., 2004. The Infrared Array Camera (IRAC) for the Spitzer Space Telescope. *APJs*, 154, pp.10-17.

Garay, G., 2005. Massive and dense cores: the maternities of massive stars. In M. F. R. Cesaroni, ed. *Massive Star Birth: A Crossroads of Astrophysics*. IAU Symposium. pp. 86-91.

Garay, G. & Lizano, S., 1999. Massive Stars: Their Environment and Formation. *pasp*, 111, pp.1049-1087.

Greisen, E.W., 2009. AIPS: Astronomical Image Processing System. Available at: http://www.aips.nrao.edu/.

Guzmán, A.E., Garay, G. & Brooks, K.J., 2010. A String of Radio Emission Associated with IRAS 16562-3959: A Collimated Jet Emanating from a Luminous Massive Young Stellar Object. *APJ*, 725,

pp.734-741.

Hildebrand, R.H., 1983. The Determination of Cloud Masses and Dust Characteristics from Submillimetre Thermal Emission. *QJRAS*, 24, p.267-+.

Juvela, M., 1996. Studies of dense molecular cores in regions of massive star formation. IV. Multitransition CS-study towards southern H_2_O masers in the longitude range l=308-360deg. *A&As*, 118, pp.191-226.

Kudritzki, R.P., 2002. Line-driven Winds, Ionizing Fluxes, and Ultraviolet Spectra of Hot Stars at Extremely Low Metallicity. I. Very Massive O Stars. *APJ*, 577, pp.389-408.

Larson, R.B., 1985. Cloud fragmentation and stellar masses. *MNRAS*, 214, pp.379-398.

Larson, R.B., 1969. Numerical calculations of the dynamics of collapsing proto-star. *MNRAS*, 145, p.271-+.

Linnik, Y.V., 1961. *Method of least squares and principles of the theory of observations*, Pergamon Press.

Lourakis, M.I.A., 2004. levmar: Levenberg-Marquardt nonlinear least squares algorithms in C/C++. Available at: http://www.ics.forth.gr/~lourakis/levmar.

Low, M.-M.M. & Klessen, R.S., 2004. Control of star formation by supersonic turbulence. *Reviews of Modern Physics*, 76, p.125–194.

Lumsden, S.L. et al., 2002. The population of the Galactic plane as seen by MSX. *MNRAS*, 336, pp.621-636.

McKee, C.F. & Tan, J.C., 2003. The Formation of Massive Stars from Turbulent Cores. *APJ*, 585, pp.850-871.

Mink, D.J., 2010. WCSTools: Image World Coordinate System Utilities. Available at: http://tdc-www.harvard.edu/wcstools/.

Mizuno, A. et al., 1995. Overall distribution of dense molecular gas and star formation in the the Taurus cloud complex. *APJ*, 445, p.L161-L165.

NIST/SEMATECH, 2011. e-Handbook of Statistical Methods. Available at: http://www.itl.nist.gov/div898/handbook/.

Ossenkopf, V. & Henning, T., 1994. Dust opacities for protostellar cores. *A&A*, 291, pp.943-959.

Padoan, P. et al., 2001. The Turbulent Shock Origin of Proto-Stellar Cores. *APJ*, 553, pp.227-234.

Padoan, P. & Nordlund, A., 2002. The Stellar Initial Mass Function from Turbulent Fragmentation. *APJ*, 576, p.870–879.

Panagia, N. 1973. “Some Physical parameters of early-type stars.” *AJ,* 78, pp. 929-934.

Pestalozzi, M.R., Minier, V. & Booth, R.S., 2005. A general catalogue of 6.7-GHz methanol masers. I. Data. *A&A*, 432, pp.737-742.

Plume, R., Jaffe, D.T. & Evans, I.I., 1992. A survey of CS J = 7 - 6 in regions of massive star formation. *ApJs*, 78, p.505–515.

Plume, R. et al., 1997. Dense Gas and Star Formation: Characteristics of Cloud Cores Associated with Water Masers. *APJ*, 476, p.730-+.

Schuller, F. et al., 2009. ATLASGAL - The APEX telescope large area survey of the galaxy at 870 um. *A&A*, 504, pp.415-427.

Shepherd, D.S. & Churchwell, E., 1996. Bipolar Molecular Outflows in Massive Star Formation Regions. *APJ*, 472, p.225-+.

Siringo, G. et al., 2009. The Large APEX BOlometer CAmera LABOCA. *A&A*, 497, pp.945-962.

Sternberg, A., T. L Hoffmann, and A. W. A Pauldrach. 2003. "Ionizing Photon Emission Rates from O- and Early B-Type Stars and Clusters." *APJ*, 599, pp. 1333-1343.

Tilley, D.A. & Pudritz, R.E., 2003. Gravitational Collapse of Filamentary Magnetized Molecular Clouds. *APJ*, 593, pp.426-434.

Urquhart, J.S. et al., 2007. The RMS survey. Radio observations of candidate massive YSOs in the southern hemisphere. *A&A*, 461, pp.11-23.

Vacca, W. D, C. D Garmany, and J. M Shull. 1996. "The Lyman-Continuum Fluxes and Stellar Parameters of O and Early B-Type Stars." *APJ,* 460, pp.914-+.

Walsh, A.J. et al., 1998. Studies of ultracompact HII regions - II. High-resolution radio continuum and methanol maser survey. *MNRAS*, 301, pp.640-698.

Walsh, A.J. et al., 1997. Studies of ultracompact HII regions - I. Methanol maser survey of IRAS-selected sources. *MNRAS*, 291, pp.261-278.

Weingartner, J.C. & Draine, B.T., 2001. Dust Grain-Size Distributions and Extinction in the Milky Way, Large Magellanic Cloud, and Small Magellanic Cloud. *APJ*, 548, pp.296-309.

Werner, M.W. et al., 2004. The Spitzer Space Telescope Mission. *APJs*, 154, pp.1-9.

Wood, D.O.S. & Churchwell, E., 1989. Massive stars embedded in molecular clouds - Their population and distribution in the galaxy. *APJ*, 340, pp.265-272.

Wu, Y. et al., 2004. A study of high velocity molecular outflows with an up-to-date sample. *A&A*, 426, pp.503-515.

Zhang, Q. et al., 2001. Search for CO Outflows toward a Sample of 69 High-Mass Protostellar Candidates: Frequency of Occurrence. *APJl*, 552, p.L167-L170.

Zinnecker, H. & Yorke, H.W., 2007. Toward Understanding Massive Star Formation. *ARA&A*, 45, p.481–563.

Appendix A

Method of Least Squares and Errors

Our function to fit is a sum gray blackbodies (Eq 6). I had 6 unknowns; T_h, T_w, N_w, N_h, β and ν_0, non of which are linear in the equation so I had to implement a method which fits non-linear least squares. I used the python implementation (Astrometry.net 2010) of *levmar (Lourakis 2004)* which is a C/ C++ implementation of the Levenberg-Marquardt nonlinear least squares minimization algorithm that is distributed under the GNU General Public License.

The general problem is to minimize;

$$F(x) = \sum_{i=1}^{m} (f_i(x))^2 \tag{28}$$

Where $x = (x_1, x_2, \ldots, x_n)^T$ are the parameters to fit, and $m \geq n$. So as to not be biased to fitting better the wavelengths with higher fluxes, I used f_i in our case as the difference between the base_{10} logarithm of our model (eq 6) evaluated at the point x and the base_{10} logarithm of the observed values (the flux densities at each wavelength). As I had 12 fluxes to fit, I had 12 $f_i(x)$ one for each observed value.

$$f_i(x) = \log_{10}(F_v(x)) - \log_{10}(y_i) \quad \text{where } y_i = \text{observed value in Jy} \tag{29}$$

The output of the program is the computed solution x_f (generally a local minimum) found given the starting point. I had to calculate the errors by means of determining the variance-covariance matrix (XX book 1):

$$C = \sigma^2 (J^T J)^{-1} \tag{30}$$

Where σ^2 is the estimated variance of the residual at the computed solution x_f, given by,

$$\sigma^2 = \frac{F(x_f)}{m-n} \quad if\ m > n, \ and\ 0 \ \ if\ m = n \tag{31}$$

And J is the Jacobian matrix of f(x):

$$J = \begin{matrix} \frac{\partial f_1}{\partial x_1} & \cdots & \frac{\partial f_1}{\partial x_n} \\ \vdots & \ddots & \vdots \\ \frac{\partial f_m}{\partial x_1} & \cdots & \frac{\partial f_m}{\partial x_n} \end{matrix} \tag{32}$$

There are cases in which $J^T J$ is singular then the pseudo-inverse is taken instead. The diagonal (off-diagonal) elements of C are estimates of the variances (covariances) of the estimated regression coefficients.

A.1 Chi-square

To assess the goodness of fit I constructed the weighted sum of square errors. Conservative flux uncertainties of 20% were taken for IRAS, MSX and IRAC data, and 15% for ATLASGAL. In my case,

$$\chi^2 = \sum \frac{(\log_{10}(Fitted\ value_i) - \log_{10}(Observed\ value_i))^2}{\sigma_i} \tag{33}$$

Where σ_i is the known variance of the 10-base logarithm of the observation, obtained from the assumed uncertainty. I used log10(flux/Jy) as not be biased to over-fit the frequencies with higher flux values. And the reduced chi-square is,

$$\chi^2_{red} = \frac{\chi^2}{dof} \tag{34}$$

Where dof = degrees of freedom = m – n. If $\chi^2_{red} > 1$ indicates that the fit does not fully captures the data (or the error variance is underestimated), a $\chi^2_{red} < 1$ indicates that the model is over-fitting the data (model is either fitting improperly the noise, or the error variance has been overestimated), and $\chi^2_{red} \approx 1$ indicates that the observations and fitted values are in accordance to the error variance.

The obtained values are in the range of 0.02 to 2.04 with a mean of 0.36. Only two values were over 1.2 which indicates that almost all the values were well fitted within the given uncertainties, and these two values (G10.47 and G34.26) were not too far from 1.0 as not to contradict the conclusion of a obtaining a good fit. The majority of the values were under 0.5 which is most probable due to the fact that I assumed a conservative (but still expected) uncertainty. Were I to use a more exact uncertainty the obtained reduced chi-square should not be so over-fitted.

A.2 Confidence intervals

If x* is the true solution, then the 100(1-β)% confidence interval on x_f is (Linnik 1961),

$$(x_f)_i - \sqrt{c_{ii}} \cdot t_{(1-\beta/2, m-n)} < x^* < (x_f)_i + \sqrt{c_{ii}} \cdot t_{(1-\beta/2, m-n)} \qquad i = 1,2,\ldots,n \tag{35}$$

Where $t_{(1-\beta/2,m-n)}$ is the $100(1-\beta)/2$ percentage point of the t-distribution with $m-n$ degrees of freedom.

I calculated three confidence intervals (CI) 68%, 90% and 95%. The fitting errors for T_h, T_w, N_w and N_h, for all the objects were reasonable, all these errors were lower than the value of the parameter fitted. But for β and ν_0, 7 objects had errors (even in the 68% CI) above the actual fitted value. The median values of the errors are shown in table 16 plus the mean value for comparison. For T_h, T_w, N_w, N_h and ν_0 the errors are less than the mean value, but for β I should only rely on the 68% CI.

Table 16: SED parameters fitting errors

Fitted Parameter	Median Error 68% CI	Median Error 90% CI	Median Error 95% CI	Mean value
T_w [K]	9.52	18.67	23.76	121.15
T_h [K]	13.83	27.05	34.5	432.88
N_w [10^{22} cm^{-2}]	0.14	0.27	0.34	1.18
N_h [10^{22} cm^{-2}]	0.006	0.01	0.02	0.19
β	1.27	2.43	3.06	1.85
ν_0	0.12	0.23	0.29	7.87

Appendix B

Montecarlo bootstrap distributions

Here I present all the Montecarlo bootstrap distributions arrived by comparing the Guzman list to the samples of Faundez et al (2004). The following parameters were analyzed: Cold, warm and hot components temperatures, cold components column density, mass, luminosity, radius, and density. In each Figure I present four distributions: (i) mean value of the parameter, (ii) parameter's mean difference vs Faundez et al (2004) (iii) parameter's variance, and (iv) parameter's variance difference vs Faundez et al (2004).

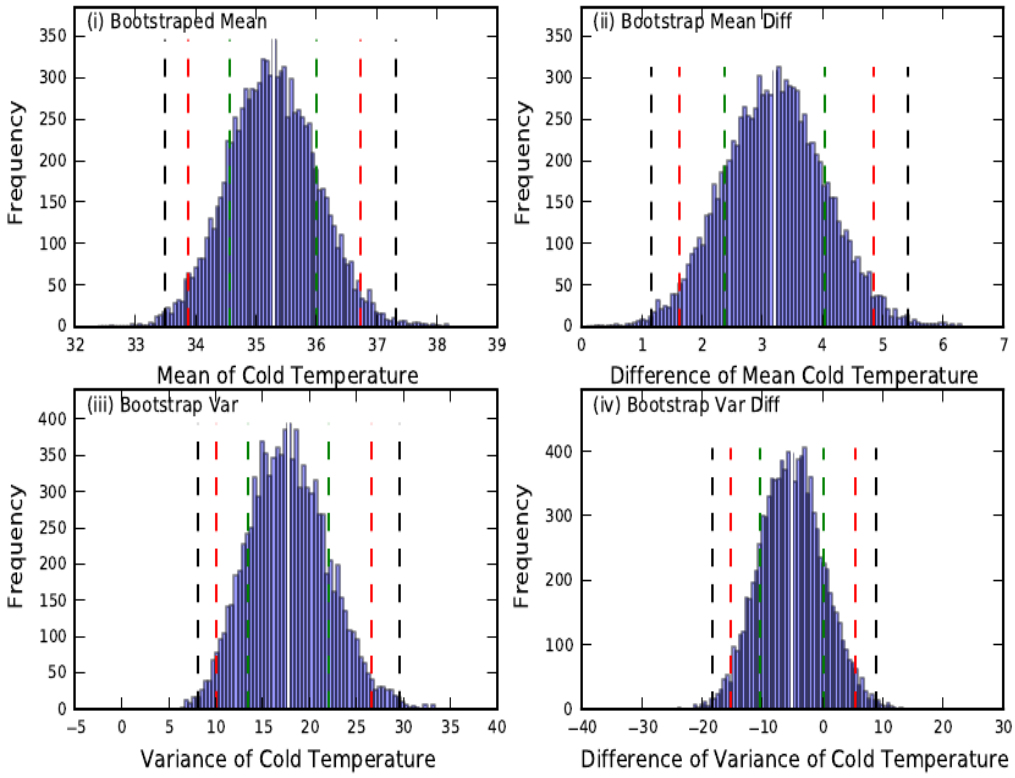

Figure 71: Cold Component Temperature (in °K), comparison vs Faundez et al (2004)

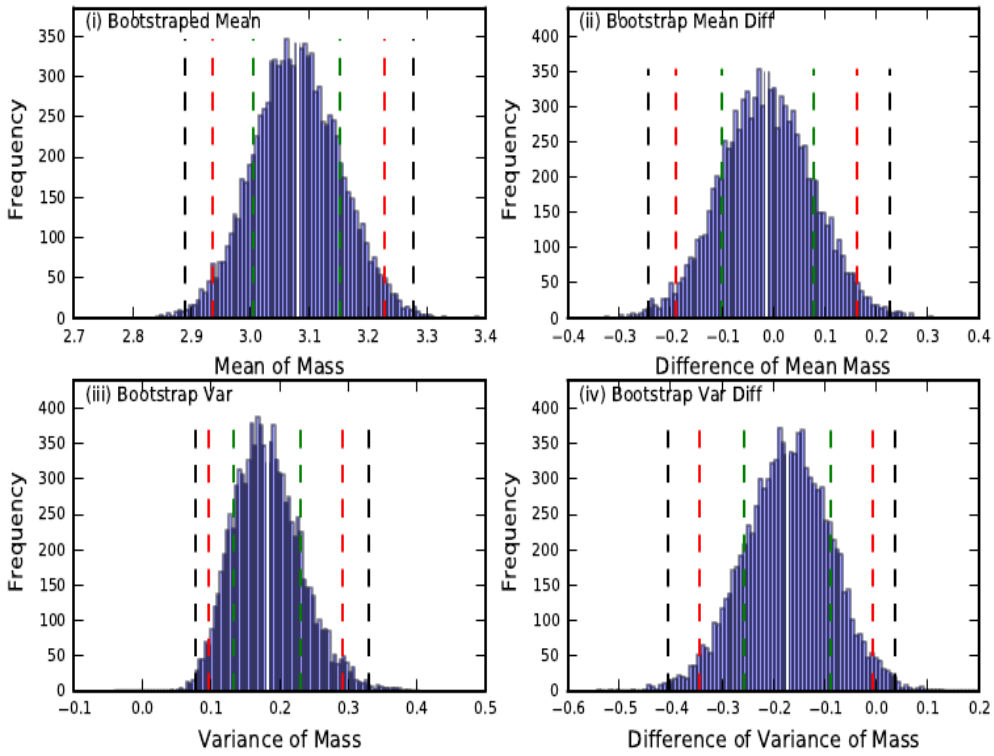

Figure 72: Mass (in $\log_{10}(M_{\odot})$), comparison vs Faundez et al (2004)

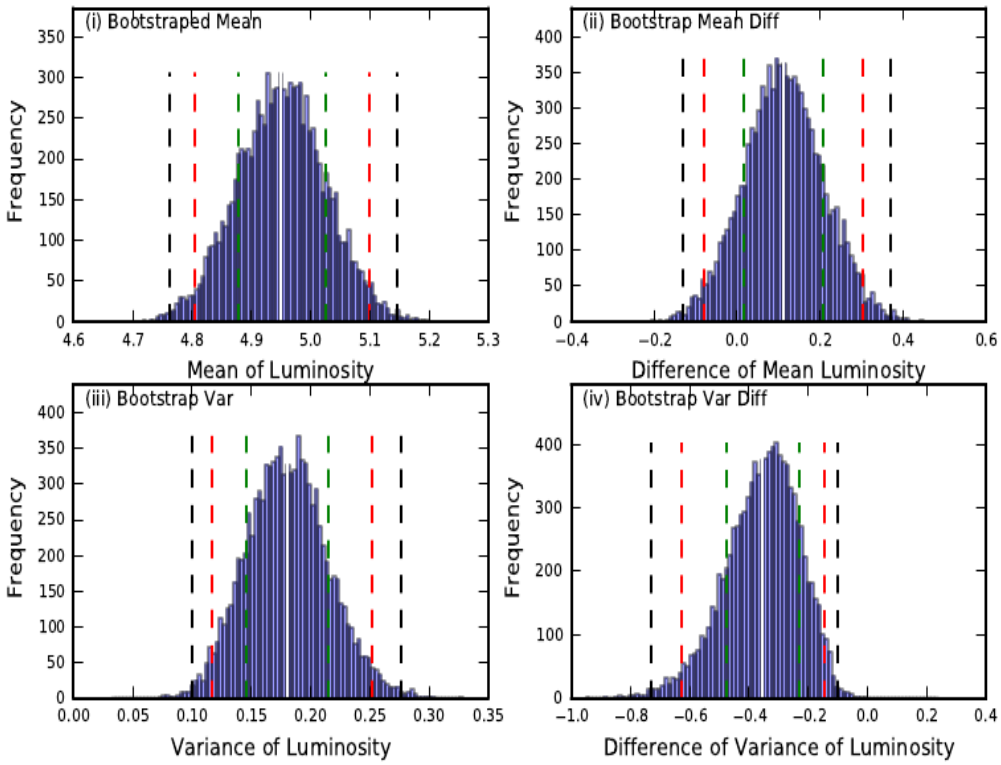

Figure 73: Luminosity (in $\log_{10}(L_{\odot})$), comparison vs Faundez et al (2004)

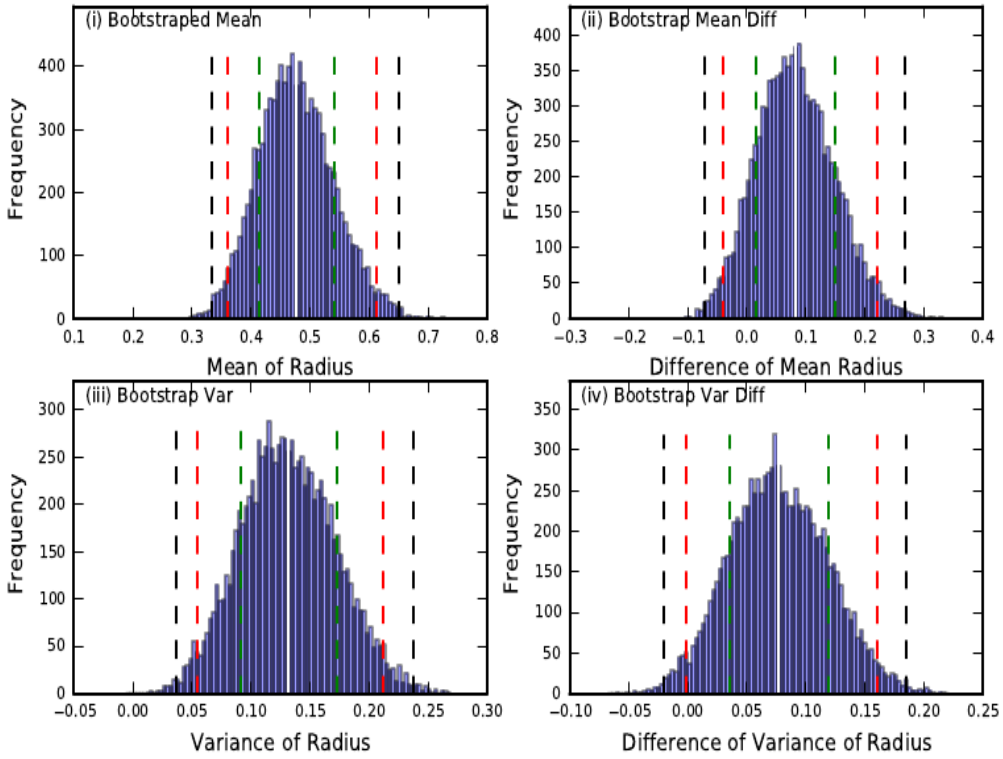

Figure 74: Radius (in parsec), comparison vs Faundez et al (2004)

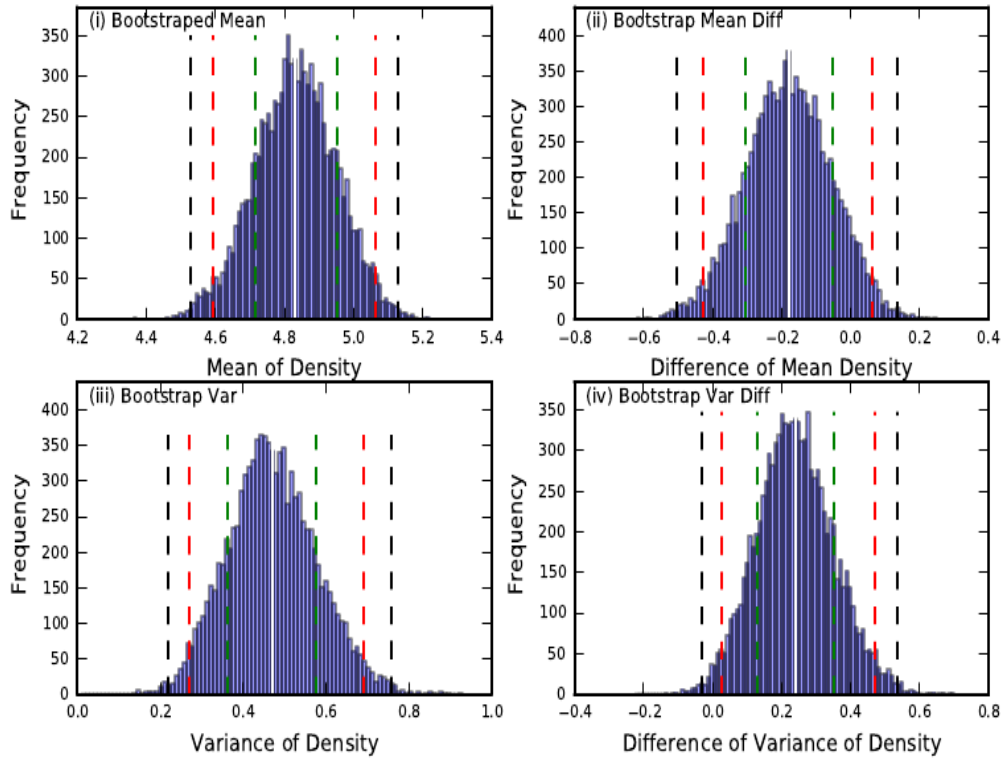

Figure 75: Density (in $\log_{10}(cm^{-3})$), comparison vs Faundez et al (2004)